Experimental Investigation of a Wind Turbine with Adaptive Camber Rotor Blades under Gusty Conditions

Schiffmann, Klaus

(2020)

Experimental Investigation of a Wind Turbine with Adaptive Camber Rotor Blades under Gusty Conditions

Vom Fachbereich Maschinenbau
an der Technischen Universität Darmstadt
zur
Erlangung des Grades eines Doktor-Ingenieurs (Dr.-Ing.)
genehmigte

Dissertation

vorgelegt von

Dipl.-Ing. Klaus Schiffmann

aus Mainz

Berichterstatter:	Prof. Dr.-Ing. Cameron Tropea
1. Mitberichterstatter:	Prof. Dr.-Ing. Ewald Krämer
Tag der Einreichung:	21. Januar 2020
Tag der mündlichen Prüfung:	26. März 2020

Darmstadt 2020

D 17

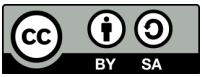

Danksagung

Die vorliegende Arbeit entstand während meiner Tätigkeit am Institut für Strömungslehre und Aerodynamik (SLA) der TU Darmstadt innerhalb eines von der Deutschen Forschungsgemeinschaft (DFG) geförderten Projektes.
Ich danke Herrn Prof. Cameron Tropea für den Freiraum, aber auch seine volle Unterstützung, wenn es nötig war.
Ich danke Herrn Dr. Klaus Hufnagel für die vielen lehrreichen fachlichen Diskussionen, seinen Glauben an mich und das Projekt und letztendlich für den Feinschliff als Ingenieur.
Ich danke den vielen motivierten Studenten, die ich betreuen durfte und die durch ihre Kreativität und ihren Einsatz maßgeblich zum Erfolg beigetragen haben. Herr Karol Hajek, der mich als Hiwi und zuletzt als Masterand über das gesamte Projekt begleitet hat, sowie Thorsten Ziegler und Martin Tvarochek bildeten das Kernteam, ohne das die Entwicklung und Fertigung von Modellen, aber auch die Durchführung der entscheidenden Messkampagnen undenkbar gewesen wäre.
Ich danke Ilona Kaufhold, Tim Geelhaar, sowie Florian Vogt und Joachim Heyl aus der mechanischen Werkstatt für die Unterstützung und die gute Zusammenarbeit, insbesondere auch in stressigen Zeiten. Gleiches gilt für Alexander Beck, Martin Weiss und Bernd Braun.
Ich danke allen Kollegen am SLA, die ich kennenlernen durfte und dazu beigetragen haben, dass ich an meine Zeit dort immer gerne zurückdenken werde.

Abstract

This study has the purpose of investigating the performance of the adaptive camber profile (ACP) concept on wind turbine blades. As such, it extends previous studies at the Institute of Fluid Mechanics and Aerodynamics at the Technische Universität Darmstadt in which the load-dependent ACP concept has been examined for two-dimensional flow and for synthetic gust generation. The experiments in this study have been performed on the Berlin Research Turbine (BeRT) at the Technische Universität Berlin.

Two main goals were formulated in designing the experiments. The first goal was to investigate the ACP performance under fully three-dimensional operating conditions and with realistic turbulence/gust conditions of the inflow. For this, the response of the ACP elements when the turbine operated with a yawed rotor plane was compared to the non-yawed case. The yawed rotor plane resulted in local variations of angle of attack, dependent on both rotation angle and span location, yielding highly unsteady conditions of the onflow. The aim was to examine the ability of the ACP concept to alleviate gust load fluctuations. The second goal was to investigate to what extent the ACP concept was suitable over a larger range of angle-of-attack variations. This was realised by outfitting one rotor blade with three ACP sections, distributed between the root and tip of the blade, since these three positions exhibit very different effective AoA variations.

The experiments show that it is favourable to control not only the outer blade area with an ACP mechanism but also the area near the blade root, resulting in a significantly higher overall gust load reduction. A peak load reduction of about 10% could be achieved. On the other hand, local load increase of about 20% could be achieved and this leads to a reduction of load fluctuation amplitude compared with rigid profiles. Based on the findings of this study it can be concluded that the ACP concept, if properly designed and imple-

mented for specific operating conditions, has great potential to increase the lifetime and the energy output of wind turbines.

Kurzfassung

Die vorliegende Arbeit beschäftigt sich mit der experimentellen Untersuchung des Adaptive Camber Profile (ACP) Konzeptes integriert in den Rotor einer Modellwindturbine. Die Arbeit ist eine Erweiterung früherer am Fachgebiet für Strömungslehre und Aerodynamik der Technischen Universität Darmstadt durchgeführter Arbeiten, die das Verhalten des passiven, lastabhängigen ACP Konzeptes in zweidimensionaler Strömung und unter dem Einfluss synthetischer Böen untersuchten. Die aktuellen Experimente wurden an der Berlin Research Turbine (BeRT) im großen Windkanal (GroWiKa) der Technischen Universität Berlin durchgeführt.
Die Experimente wurden ausgelegt um das Verhalten des Konzeptes im rotierenden System einer Windkraftanlage unter dreidimensionaler Anströmung und einer realistischen Böen Situation zu untersuchen. Die Basis der Versuchsreihe bildet der Vergleich der ACP Funktion bei gegierter und nicht gegierter Rotorebene. Wird die Rotorebene unter einem Gierwinkel angeströmt führt das zu lokalen Schwankungen des Anströmwinkels und der Anströmgeschwindigkeit am Rotorblatt. Diese hoch instationären periodischen Schwankungen in der Blattanströmung sind abhängig von der Spannweitenposition und dem Umlaufwinkel des Blattes. Das konkrete Ziel war es das Potential des ACP Konzeptes als eine Möglichkeit zur Böenlastminderung an Windturbinen zu untersuchen. In diesem Sinne war ein weiteres Anliegen herauszufinden in welchem Bereich der erzeugten Fluktuation von Anströmwinkel und Geschwindigkeit das Konzept den gewünschten Einfluss auf das Lastverhalten des Rotors zeigt. Zu diesem Zweck wurde ein Rotorblatt mit drei ACP Sektionen verteilt über die Spannweite zwischen Blattwurzel und Blattspitze entwickelt. Die experimentellen Ergebnisse zeigen, dass es sinnvoll ist nicht nur die äußeren Bereiche eines Rotorblattes mit dem ACP Konzept zu kontrollieren, sondern insbesondere auch die mittleren und die Bereiche nahe der Blattwurzel. Ver-

glichen mit der starren Conflagration des Rotorblattes konnte eine Spitzenlastreduktion des kritischen Wurzelbiegemomentes um 10%, bei gleichzeitiger Erhöhung lokaler Lasten um 20% nachgewiesen werden. Das führt zu einer Reduzierung der Böenamplitude verglichen mit einem konventionellen Rotorblatt. Aufgrund der Ergebnisse kann davon ausgegangen werden, dass das ACP Konzept, wenn richtig implementiert und eingestellt, großes Potential besitzt, sowohl die Lebensdauer, als auch die Energieausbeute von Windturbinen signifikant zu erhöhen.

Contents

Nomenclature

Abbreviations

Symbol	Description
ACP	Adaptive Camber Profile
AoA	Angle of Attack
BeRT	Berlin Research Turbine
COE	Cost of Energy Ratio
DFG	Deutsche Forschungsgemeinschaft
LEV	Leading Edge Vortex
PIV	Particle Image Velocimetry
TEF	Trailing Edge Vortex
TSR	Tip Speed Ratio
SLA	Institute "Strömungslehre und Aerodynamik" of TU Darmstadt

Roman Symbols

Symbol	Description	Unit
A	Wing area	$[m^2]$
C	Theodorsen function	[-]
c	Chord length	[mm]
D	Rotor diameter	$[m]$
f	Frequency of perturbation	$[1/s]$
h_a	Heaving amplitude	[m]
h	Transfer function	[-]

L	Lift	[N]
l_{ref}	Reference length	$[m]$
M	moment	$[Nmm]$
N	Number of samples	[-]
n	Coupling ratio	[-]
P	Power	$[W]$
p	Rotor revolution frequency	$[1/s]$
R	Rotor radius	$[m]$
r	Local blade radius	$[m]$
s	Estimated standard deviation	[°,m/s,-]
t	Time	$[s]$
U	Steady horizontal velocity	$[m/s]$
u	Uncertainty	[°,-]
v	Velocity	$[m/s]$
y	Strain gauge value	$[V]$

Greek Symbols

Symbol	**Description**	**Unit**
α	AoA	[°]
β	Side-slip angle	[°]
γ	Trailing edge flap angle	[°]
θ	Azimuthal angle	[°]
λ	Tip speed ratio	[-]
ν	Kinematic viscosity of air	[m^2/s]
ρ	Density of air	[kg/m^3]
σ	Standard deviation	[°,m/s,-]
τ	Local blade twist angle	[°]
ϕ	Yaw angle	[°]
Ω	Angular frequency of rotor	$[1/s]$
ω	Angular frequency of perturbation	[1/s]

Dimensionless Numbers

Symbol	Description	Definition
c_L	Lift coefficient	$\frac{L}{\frac{\rho}{2}U_\infty^2 A}$
c_p	Pressure coefficient	$\frac{p_s - p_\infty}{\frac{\rho}{2}U_\infty^2}$
k	Reduced frequency	$\frac{\omega c}{2U_\infty} = \frac{\pi f c}{U_\infty}$
OPRB	Out-of-Plane Root Bending Factor	$\overline{y}(\theta)\frac{1}{\overline{y}_{rigid-max}}$
Re	Reynolds number	$\frac{U_\infty c}{\nu}$
St	Strouhal number	$\frac{2fh_a}{U_\infty}$

Subscript

Symbol	Description
$Aero$	Aerodynamic
dyn	Dynamic
$flexibel, flex$	Flexibel
max	Maximal
min	Minimal
qs	Quasi-steady
ref	Reference

$rigid, rig$	Rigid blade
$Spring$	Spring
s	Static
T	Total
x, y, r	Coordinates as defined in figures 2.5 and 4.7
$2d$	Two-dimensional
∞	Undisturbed

Superscript

Symbol	**Description**
$\hat{}$	Maximum amplitude
-	Mean
$'$	Stochastic fluctuation
$\tilde{}$	Time dependent periodic fluctuation

1 Introduction

1.1 Motivation

Classic aerodynamics is based on rigid profiles in steady flows, which has been widely investigated, experimentally, numerically and analytically. A next step in complexity is to include unsteadiness of the inflow and still further, fluid structure interaction, in which flexible structures are influenced by the flow field. Wind gusts acting on wind turbines is an example of such a complex aerodynamic problem and the flow unsteadiness influences the set point operation conditions and limits the lifetime of rotor blades. Moreover, without a basic understanding of the response of wind turbine blades to wind gusts or other sources of unsteadiness, an up-scaling is difficult; hence, also the ability to realise the highest potential of physically possible energy harvesting. Familiar design theories, like the theory of Betz (1924), Schmitz (1955) or Hütter (1942), do not capture these effects.

Within the framework of wind gust response on wind turbine rotor blades a passive approach for gust load alleviation on wind turbines has been developed and patented (Hufnagel & Lambie (2013)) at the Institute of Strömungslehre und Aerodynamik (SLA, Fluid Mechanics and Aerodynamics) of the Technische Universität Darmstadt. The concept is based on a variable camber line of an aerodynamic profile, which adapts passively according to local in-flow conditions. The performance of this adaptive profile was investigated experimentally for two-dimensional flows under steady conditions by Lambie (2011) and for two-dimensional flows under unsteady conditions by Cordes (2016). Furthermore, Spiegelberg (2014) investigated a structural model of the adaptive camber aerofoil analytically by coupling a three-degrees-of-freedom model to unsteady thin aerofoil theory and a quasi-steady panel code.

These previous studies indicated high potential of the concept for alleviation of gust load fluctuations under steady and unsteady conditions. Nevertheless, several basic questions remain to be clarified. For one, previous work was restricted to two-dimensional flows with strictly harmonic flow excitation. However, real-world gusts acting on wind turbine rotor blades exhibit a high degree of three-dimensionality and local inflow fluctuations may deviate significantly from harmonic excitation. Furthermore, previous work was restricted to local angle-of-attack (AoA) values lying in the regime of linear lift coefficient. On a wind turbine this assumption is not always valid, especially near the root of rotor blades.

An investigation of these questions solely on the basis of numerical simulations is difficult for a multitude of reasons, most of which culminate in extremely high demands on computing capacity. However, a very elementary difficulty lies in specifying appropriate boundary conditions, since it is not trivial to know the exact inflow conditions on a rotor blade in real-world operating conditions and furthermore, these can be influenced by component interactions, for instance between the tower and the blades. Hence, a complete simulation of the entire wind turbine is necessary to insure that such effects are captured. Experimental investigations are therefore still indispensable and build the focus of the present study.

1.2 Gust Load Alleviation on Wind Turbines: State of the Art

This section offers an overview of current concepts for gust load alleviation of which the Adaptive Camber Profile (ACP) is one and which will be elaborated in more detail in the subsequent section. Gust load alleviation concepts can be generally categorised into global or local systems. Global approaches affect the rotor blade in its entirety, for example pitch control or individual

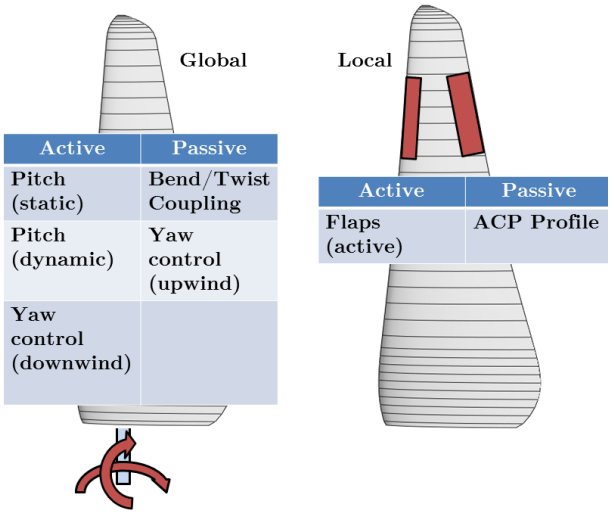

Figure 1.1: Classification of gust load alleviation approaches in rotor aerodynamics.

pitch control, whereas local approaches influence only a limited rotor blade segment. In addition, methods can be classified as active or passive systems. An active system comprises a sensor, an actuator and control algorithm; a passive system features structural deformations according to its design properties. In passive systems the energy required for deformation is supplied by the gust itself.

From a more general viewpoint, systems designed to influence the circulation (or lift) around an aerofoil is a broad topic in both steady and unsteady aerodynamics and active means include such devices as trailing edge flaps, synthetic jet actuators or dielectric barrier discharge (DBD) plasma actuators. Passive elements include vortex generators, micro-tabs or bend/twist coupling designs. Graphically these categories and some examples of each are shown in figure 1.1. The various approaches for gust load alleviation are described and summarised by e.g. Barlas (2011).

The most widespread load control system employed on wind turbines is pitch control. Common turbines are equipped with a static pitch control mechanism; however, these devices are not suitable for sudden gusts because they react too slowly. Through pitch control the blade loading can be influenced by changing the mean angle of attack (AoA) simultaneously for all radial blade sections. Dynamic pitch control systems are able to react faster and are in common use on helicopters and to a limited extent on wind turbines. On wind turbines individual pitch control (IPC) has been widely tested on research turbines and first realisations on production units are appearing. With this concept the pitch of each blade is controlled independent of one another. Plumley et al. (2014) compare the IPC approach with smart rotor control strategies for load reduction. Smart rotor concepts are characterised by Plumley et al. (2014) as devices distributed along the blades, allowing a real time adjustment of aerodynamic characteristics.

Passive methods of circulation control come from the field of helicopter aerodynamics. The bend of a rotor blade due to aerodynamic loading is used to achieve a controlled twist, which generates a pitching movement and adapts the blade segment to the instantaneous inflow angle of attack. In recent years the bend/twist coupling has been successfully introduced into wind turbine design. The bend twist coupling approach for wind turbine blades is discussed in Lobitz & Veers (1998) and Fedorov & Bergreen (2014)

Still another approach to gust alleviation is to rotate the rotor plane about a yaw angle. Yawing the rotor plane with respect to the mean inflow direction reduces the effective area of the rotor plane. According to Betz (1924) the maximal physically possible energy output of a wind turbine is approx. 59% of the wind energy contained in the airflow through the rotor plane. Decreasing the area of the rotor plane by increasing the yaw angle effectively lowers the inflow velocity on the radial blade sections over the rotation. On the other hand, yawing the rotor plane introduces a further unsteadiness, a topic which will be discussed in detail in the scope of this study.

The most familiar sectional approach to control the lift distribution of an aerofoil under changing inflow conditions are flaps, especially trailing edge flaps. Trailing edge flaps are well known from aircraft aerodynamics, commonly designed for steady or quasi-steady conditions and widely used as a high lift device during start and landing of aircraft. A flap deflection is essentially equivalent to a change of the profile cambering. A small flap deflection yields a relatively high change in lift force (circulation), which makes this technique attractive for gust load alleviation.

When discussing circulation control directed towards specific blade segments another aspect must be considered for wind turbines. The highest moments on the blade are generated at outer radial blade sections because of the long moment arm. Relatively small load alleviation at the blade tip can be very effective in decreasing overall bending moments; hence, lifetime duration. On the other hand, the blade root has the highest overall loading, therefore the blade profile in the root section is designed comprising aerodynamic performance with structural integrity, resulting in relatively thick profiles. Improvement of the aerodynamics in the root section is therefore also a consideration when introducing lift control schemes into wind turbine blade design.

Although trailing edge flap devices superficially appear attractive for use on wind turbines, there are contradicting demands to be met. The most evident is the fact that energy must be supplied to actuate the trailing edge device. In addition, sensors, actuators and a control circuit are required if the trailing edge is implemented as an active device. These demands are amplified in complexity simply by the fact that wind turbines are not available for regular maintenance and must withstand very harsh environmental conditions over long periods. A summary of trailing edge devices as applied to wind turbines is given by Barlas & van Kuik (2009) and Johnson et al. (2010).

Passively actuated flaps are less widespread, although an admirable attempt in recent years is documented by Bottasso et al. (2016) in which a reduction

of fatigue loads on wind turbines has been analytically examined. The passive trailing edge flap is actuated by aeroelastic blade movement. An additional mass is used, whose inertial from blade bending actuates the flap deflection to offset the increased lift. However, the disadvantage is similar to the bend/twist coupling, that a global blade deformation is obtained to realise a local gust mitigation. There are attempts with flexible trailing edge flaps actuated by the aerodynamic forces acting on the flap and resulting from changes in lift, but the aerodynamic lift forces acting on a profile are small at the trailing edge, exhibiting their maximum values closer to the leading edge. Indeed, it is exactly these considerations which led to the concept of the Adaptive Camber Profile.

1.3 Adaptive Camber Profile

The adaptive camber profile as pictured schematically in Figure 1.2 comprises three sections: a movable leading edge flap, a movable trailing edge flap and a rigid middle part, onto which the flaps are mounted. The pivot of the leading edge flap is located at 20% of the profiles chord line and the pivot of the trailing edge flap is located at 70% of the chord line. These flap ratios where deemed optimal in the study by Spiegelberg (2014), in which the ACP was modelled as a three degree of freedom mechanical system and the flow was considered ideal (potential flow).

A Clark-Y profile was chosen, because it does not exhibit abrupt stall behaviour at low Reynolds numbers and furthermore, its lift distribution is sensitive to trailing edge flap movement. Moreover, it has a relatively small thickness, but is still large enough to implement mechanical and measurement equipment inside the profile. The Clark-Y profile was used by Charles Lindbergh during his flight over the Atlantic Ocean with the Spirit of St. Louis and is one of the most famous aerodynamic profiles, being very well investigated over the years.

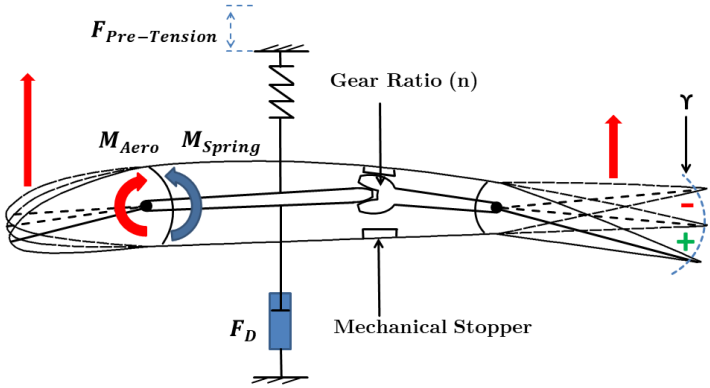

Figure 1.2: Schematic of the Adaptive Camber Profile (ACP) concept.

The leading edge and trailing edge flaps are coupled mechanically with a specified coupling ratio (n). The entire system has an inherent spring stiffness characterised by a spring constant and an adjustable pre-tension. To adjust the pre-tension, mechanical stoppers are integrated into the system. The mechanical system has an internal damping, the magnitude of which is determined by the specific design. If ball bearings are used for flap mounting and a wheel gear for the coupling, the inherent damping can be estimated as the sum of roll friction in bearings and gear wheels. The degree of damping influences how quickly the ACP is able to react to unsteady loads.

The force for actuating the trailing edge arises from the aerodynamic moment created at the leading edge flap. A flap deflection of 0° corresponds to the rigid Clark-Y profile contour, denoted as the base contour. Negative flap angles indicate a de-cambering from the base contour and positive flap angles a stronger camber, whereby a pre-cambering of the ACP can be realised using corresponding spring pre-tension. It is typically desired that the profile works around a certain operation point. The operation point is a point at a specific inflow velocity and rotor frequency where the profile should have the

geometric form of the rigid Clark-Y profile. The decisive parameter to adjust an ACP profile to this condition is the pre-tension. If the driving moment on the mechanism is known, the maximum and minimum flap deflection during operation can be adjusted by choice of the spring stiffness.

If the ACP works in unsteady conditions the damping parameter plays an important role. When the gust is too rapid, the damping prevents a reaction of the profile camber. The choice of spring stiffness and pre-tension is directly connected with the coupling ratio of the system, because this parameter dictates the mechanical spring movement. In this context it makes a difference if the spring is connected to the trailing edge flap or the leading edge flap, which must be taken into consideration when the ACP is designed for a specific purpose. The design guidelines for the ACP, depending on the expected aerodynamic operating range, have been described in detail in Spiegelberg (2014).

1.4 Outline of the Thesis

The common conception of a gust is a sudden increase of wind speed or a change of wind direction, as one might encounter while driving a car on the highway. Chapter 2 examines more closely what can be understood by a 'gust' from a more engineering point of view. Furthermore, gusts typically encountered by a wind turbine are characterised and quantified. Necessarily, this chapter begins with some general comments directed towards the fundamentals of unsteady aerodynamics, including the governing dimensionless numbers. In Chapter 2 the concept of the Adaptive Camber Profile (ACP) is introduced and ACP design guidelines for wind turbines are summarised. Chapter 2 closes with a classification of gust scenarios encountered by wind turbines and their impact on the lifetime and energy output. These aspects are also discussed with respect to economic considerations.

Chapter 3 provides details of the experimental facilities and methods. It starts by describing the facility where the experiments have been conducted,

including the Berlin Research Turbine (BeRT). Then the ACP blade design and instrumentation is discussed in detail, since proper design is the key factor to successful operation. This topic is given extra attention, since this design is exemplary for scale-up designs on full-scale turbines. Moreover, the design used in this study is not comparable to those used in previous studies. The measurement equipment, measurement procedure and measurement uncertainties are described in this chapter, including a unique five-hole probe used to monitor local inflow conditions on individual rotor blades. The chapter concludes with an overview of the test cases which were conducted and how the collected data was processed and presented.

In Chapter 4 the results of the measurement campaign are presented, discussed and validated. These are then compared with numerical simulations, where possible.

The thesis concludes with a summary and outlook in Chapter 5. The achievements and findings concerning the present state-of-the-art of ACP rotor research are summarised and the next research and development steps necessary for implementation of the concept are discussed.

2 Unsteady Aerodynamic Considerations

The following chapter is not intended as an extensive introduction into the fundamentals of aerodynamics and wind turbines; for that purpose there are numerous excellent textbooks and references available, starting from the seminal works of Betz (1924), Hütter (1942) and Schmitz (1955) or comprehensive textbooks such as Gasch & Twele (2010), Burton et al. (2011) and Leishman (2006). The latter book, entitled "Principles of Helicopter Aerodynamics", although being a standard reference for helicopter research, includes a highly recommendable chapter about wind turbine aerodynamics, especially regarding unsteady phenomena acting on turbine blades.

In the following sections aspects of aerodynamic theory which are crucial for the understanding of the design and evaluation of the present experiments are discussed.

2.1 Wind Turbine under Gusty Conditions

Wind turbines do not operate under steady flow conditions. Even when operating at the design tip speed ratio at constant wind speed without a yaw or tilt misalignment of the rotor plane, dynamic loads arise due to the velocity profile of the atmospheric boundary layer or the tower passing of the blades (tower shadow). In addition, Barlas & van Kuik (2009) describe aerodynamic and gravitational loads which appear as internal structural loads due to aeroelastic coupling. These various loads are transferred from the blade root to the drive train and to the tower. In this way they influence lifetime,

power output and maintenance costs of the turbine. External load sources can be summarised as:

- Atmospheric boundary layer
- Turbulence and gusts (rotational sampling of eddies)
- Yaw and tilt misalignment of rotor plane
- Tower shadow
- Gravitational loads

The loads occurring during "normal" rotor operation can be characterised as periodic. Bernhammer et al. (2016) cite these periodic loads as the main source of structural fatigue. According to Barlas & van Kuik (2009) these loads are crucial for structural turbine design considerations. It is evident that periodic loads are related to the rotor frequency and the number of blades. For common turbines the load frequencies from these periodic sources varies from 1p to 5p, where p is the rotor revolution frequency.

It is obvious that critical frequencies for the tower, the drive train and the nacelle are about 3p, because typical commercial turbines are equipped with three blades and load fluctuations are experienced from each blade once per rotation. The critical load frequency for the blade root is accordingly about 1p, which is confirmed by Bergami & Gauna (2014), who have investigated the NREL 5MW WEA. Bergami & Gauna (2014) have also found the critical frequencies for fatigue loads to be between 1p and 2p.

Beside periodic loads, there are also transient isolated events, which according to Gasch & Twele (2010) occur because of manoeuvre disturbances or aerodynamically extreme conditions. Such events produce friction and braking forces, which provoke aerodynamic and gravitational loads, for example during an abrupt turbine stop. Furthermore, stochastic loads arise caused for example by sea disturbances, earthquakes or wind turbulence. Viewed in the framework of the present change of climate, these can be expected to become

more extreme in the future.

The economics of wind turbines is often summarised in the quantity "Cost of Energy Ratio" (COE) as defined by Johnson et al. (2010) and later refined by Fingersh et al. (2006) in the form:

$$\text{COE} = \frac{\text{Capital cost} + \text{Operation and maintenance cost}}{\text{Lifetime energy capture}} \tag{2.1}$$

An effective way to decrease the COE ratio is to increase the power captured by the turbine over its lifetime. This is most easily achieved by increasing the rotor diameter, as seen from the expression for output power as adapted from Gasch & Twele (2010):

$$P = c_p \frac{\rho}{2} U_\infty^3 \pi (\frac{D}{2})^2 \tag{2.2}$$

where, c_p is the power coefficient, U_∞ is the undisturbed mean inflow velocity, ρ is the density of air and D is the rotor diameter. Despite increased capital costs associated with increasing the rotor diameter, rotor diameters have increased rapidly in the past years. The world's largest turbine currently in operation is the Haliade-X 12 MW offshore turbine with a rotor diameter of 220 m and a total height of 260 m. One blade measures 107 m in span. However, there is a limit to turbine diameter, arising from structural loading.

Concurrent with the increase of rotor diameter and associated large blade deformations during operation, the extreme loads come more into focus of the design considerations according to Bernhammer et al. (2016). The deformation of the blades normal to the rotor plane influences the necessary tower clearance and the nacelle overhang. This deformation of the blades is directly related to the out-of-plane root bending moment, one of the quantities to be examined in the present study. It is therefore of great interest to reduce the root bending moment and deformations caused by periodic and extreme loads. For this, a gust load alleviation concept offers one solution, ultimately aimed at decreasing the COE. In brief, a gust load alleviation concept should exhibit the following characteristics:

- Ability to damp external periodic loads
- Ability to damp external extreme loads
- Ability to minimise blade deformations
- Low initial capital costs
- Low maintenance costs
- Good compatibility with other turbine control mechanisms
- Ability to increase energy capture

The adaptive camber profile examined in the present study, fulfils most of these demands.

2.2 Fundamentals

A steady aerodynamic condition for a profile is characterised by a constant inflow velocity and a constant AoA generating a constant lift force. With regard to the Adaptive Camber Profile (ACP) this means that the resulting aerodynamic moment at the leading edge flap and the spring moment acting in the opposite direction are equal and thus, the profile is in an equilibrium state of camber. Wind turbines operating at their set point can be considered to be operating under steady conditions. For such conditions the pre-camber and pre-tension of the ACP can be adjusted, such that the profile takes the optimal shape of a rigid profile suited to this reference steady-state condition. The Clark-Y profile has been selected as a reference profile for the ACP. The aerodynamic characteristics of this profile have been obtained using potential flow theory, as implemented in XFoil (Drela (2014)). In previous work of Lambie (2011) and Spiegelberg (2014), quasi-steady behaviour of the ACP was assumed and the lift curve was computed for both the rigid profile and for the ACP, computing the degree of camber as dictated by the acting aerodynamic forces. These studies revealed that the slope of the lift curve decreases with decreasing spring stiffness, whereas a higher pre-tension shifts the lift

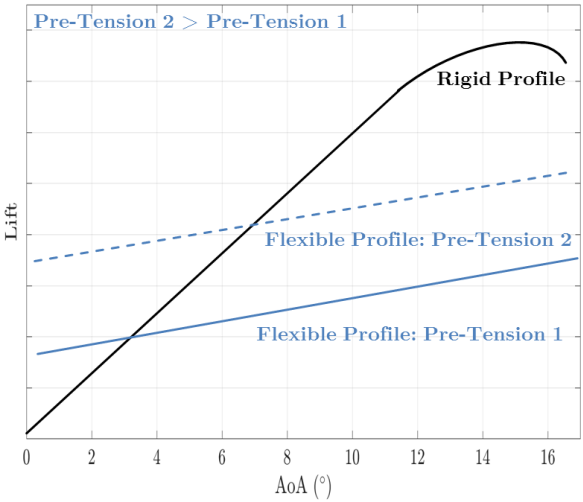

Figure 2.1: Lift of a rigid Clark-Y airfoil over the AoA at quasi-steady inflow conditions (black line). The lift curve is compared to the behaviour of an ACP profile with a fixed spring stiffness and two different pre-tensions.

curve vertically upwards. Figure 2.1 shows this behaviour, comparing the rigid airfoil to the operational ACP. The spring stiffness is held constant, but two different pre-tensions are exemplary shown.

Unsteady aerodynamic conditions occur when changes of the inflow velocity occur rapidly compared with the time fluid elements need to traverse the chord of the airfoil. The ratio of one to the other is known as the reduced frequency, given by

$$k = \frac{\pi f c}{U_\infty} = \frac{\omega c}{2U_\infty} \tag{2.3}$$

where f is a frequency characterising the inflow velocity changes and c is the airfoil chord. The value of reduced frequency at which quasi-steady conditions can no longer be applied is dependent on many different factors, but for two-dimensional pitching/plunging airfoils exhibiting no flow separation,

unsteady aerodynamic considerations are thought to be necessary for $k > 0.05$ (Leishman (2006)). For flows in which separation occurs, e.g. dynamic stall, this value is presumably less, but again, many other factors are of influence, including three-dimensional effects in practical applications. Typical reduced frequencies for wind turbines as well as flapping flight of birds are around 0.1. Further details of the theory for unsteady aerodynamics can be found in Gülçat (2016).

The Strouhal number is also relevant in unsteady aerodynamics, being defined as

$$St = \frac{f l_{ref}}{U_\infty} = \frac{2 f h_a}{U_\infty} \tag{2.4}$$

In contrast to its relevance in steady flows, where f is the frequency of shed vortices from a bluff body of characteristic length scale l_{ref} (for instance the diameter of a cylinder in a cross-flow), for unsteady situations f is defined as described above in connection with Eq. 2.3 or the frequency of airfoil movement for pitching/plunging/flapping applications. h_a is the amplitude of the excitation. For pitching/plunging scenarios of an airfoil h_a is typically taken as the heaving or pitching amplitude of the leading or trailing edge movement. In flapping flight, Strouhal numbers between 0.2 and 0.4 lead to high propulsive efficiency.

This discussion already indicates that unsteadiness can arise on the one hand from unsteady inflow conditions such as a gust, on the other hand unsteadiness can result when the lifting surface undertakes movement, such as pitching/plunging or flapping. These two scenarios for unsteadiness are not equivalent and this is reflected in analytic approaches to describe their aerodynamic responses, as will be discussed below. However, first some general characterisation of unsteady aerodynamic phenomena will be presented.

2.2.1 Dynamic Stall

Under steady inflow conditions in which no flow separation over the airfoil occurs, the lift is linearly proportional to the angle of attack (see Fig. 2.1). For the Clark-Y airfoil used as an Adaptive Camber Profile, this linear range is -4°<AoA<10°, the angle -4° being the angle for which the profile exhibits zero lift. Beyond 10° the lift increase is non-linear, followed by a condition of flow separation. The critical AoA at which the maximum lift occurs under steady conditions followed by a break down of lift caused by separation is termed the static stall limit. The static stall limit of the Clark-Y profile is about 15°.

For unsteady conditions in which the effective angle of attack exceeds the static stall limit, dynamic stall can occur. Dynamic stall can be caused either by fluctuations of the inflow angle or by movement of the airfoil relative to the inflow. The dynamic stall phenomenon can be explained with the help of Fig. 2.2, depicting the flow structure above an oscillating pitching airfoil. At stage (a) flow separation begins on the upper airfoil surface. The lift continues to increase, although the steady lift curve (blue line) decreases at the same AoA. At point (b) a pronounced leading edge vortex (LEV) begins to appear. At stage (c) this vortex grows and moves towards the trailing edge (TE). During this period the lift continues to increase, exhibiting values higher than the 2π slope curve and above the maximum values attained in steady flow. The lift reaches a maximum when the vortex has developed to its maximum size at stage (d). Beyond that point, when the vortex detaches from the airfoil, a rapid breakdown in lift can be observed. At stage (e) the profile is in a fully stalled condition. If the AoA then decreases, the flow reattaches at point (f), which brings the dynamic curve back to values typical of steady flow.

Dynamic lift was first observed by Kramer (1932). The connection between the dynamic lift increase and vortex structures, as pictured in figure 2.2, was first investigated by Carr et al. (1977) and Carr et al. (1978). More recently the development of the LEV due to dynamic stall was investigated by Baik

et al. (2012) and Akkala & Buchholz (2016).

The practical importance of dynamic stall was discovered early in helicopter applications, because a helicopter blade typically works under rapidly changing AoA, exceeding the static stall limit. Another area in which dynamic stall becomes important is that of micro-air vehicles utilising flapping wings. During the upstroke and downstroke the leading edge vortex is a recurring phenomenon influencing strongly both lift and thrust. Whereas dynamic stall on a helicopter or wind turbine blade can be detrimental, some insects profit from the high lift caused by leading edge vortexes, especially for perching manoeuvres.

On wind turbine blades dynamic stall occurs first in the root section, because here the rotational velocity is much smaller than at the tip and any fluctuations of free-stream velocity lead to high AoA fluctuations. The difference between wind turbine blades and helicopter blades is that wind turbine blades work at much lower Reynolds numbers and the flow can be assumed to be incompressible. According to Gasch & Twele (2010), dynamic stall effects on wind turbines are assumed to be dominated by flow separation initiated near the trailing edge of the blade, because of the relative thickness of common wind turbine blades in contrast to helicopter blades. Pereira et al. (2013) suggests that a typical wind turbine blade profile has a relative thickness of over 15%. The Clark-Y, with a maximal thickness of 11.7%, is therefore not typical for a wind turbine and dynamic stall may exhibit a different behaviour compared to wind turbine blades. Nevertheless, if dynamic stall occurs, then the rotor blades can be subjected to much higher lift forces; hence, larger bending moments and danger to the structural integrity of blades.

In the framework of this thesis the separated flow regime is examined in an AoA range of about 12° to 20°. These limits have been empirically determined in an experimental campaign conducted in the active grid wind tunnel of the University of Oldenburg (Wester et al. (2018b)). The schematic in figure 2.2 is derived from measurements presented in Wester et al. (2018b) and Cordes

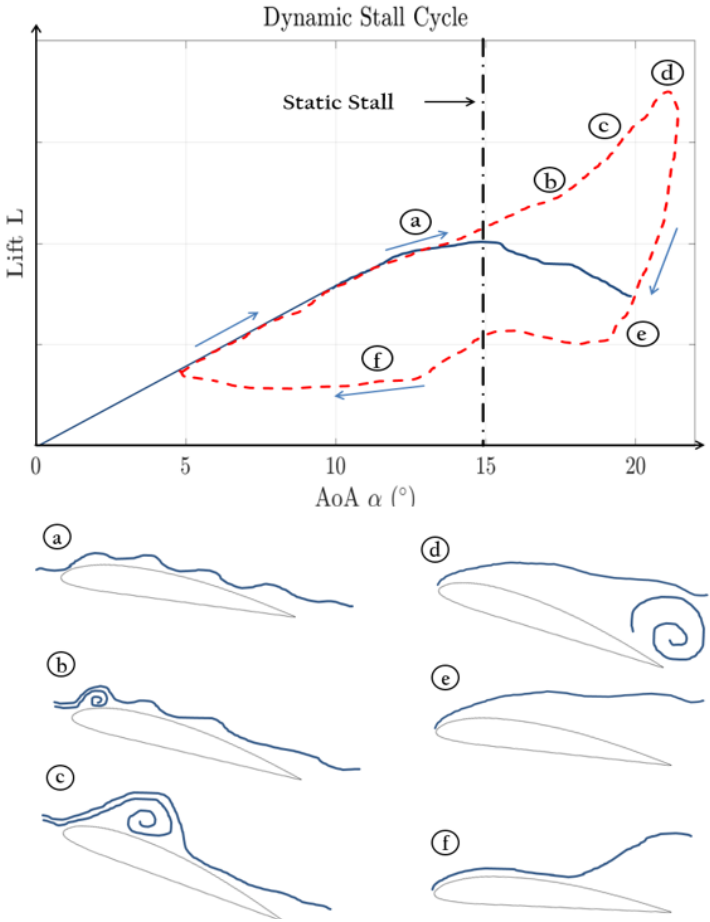

Figure 2.2: Qualitative dynamic stall cycle of a Clark-Y profile. The dotted line represents the dynamic stall behaviour of the profile over AoA. The solid line shows the steady behaviour. The static stall AoA is approximately at 15°. Typical points of the cycle are depicted underneath the plot. The schematic is derived from measurements of Kramer (1932) and Cordes (2016)

.

(2016). In contrast to Wester et al. (2018b), where the AoA fluctuation is generated by an oscillating grid, Cordes (2016) performed pitch and plunge experiments with similar results regarding the flow structure during the dynamic stall cycle.

Whereas the lift at AoA values in the linear regime can be well predicted, the prediction of loads incurred during dynamic stall on wind turbine rotor blades remains a challenging task and common models are still of semi-empirical nature. The most popular model for helicopter blades is the Beddoes-Leishman model introduced in Leishman & Beddoes (1989). The popularity of the Beddoes-Leishman dynamic stall model is based on the fact that the empirical parameters which are needed can be taken from quasi-steady profile measurements. It considers unsteady forces induced by a developing leading edge vortex and therefore includes a dynamic point of separation. The separation point is derived from measurements obtained under static or quasi-static conditions. Furthermore, empirical time constants are taken into account to specify the time delay in aerodynamic loading due to unsteady effects with respect to the steady case.

There are attempts to adapt the Beddoes-Leishman stall model for wind turbines. Assuming small Mach numbers and a dominant trailing edge vortex caused by thick profiles, the empirical parameters must be adapted. Furthermore, Pereira et al. (2013) take rotational forces into account, which are assumed to play a non-negligible role in dynamic stall onset, especially in the blade root region of a wind turbine. These assumptions are confirmed by Herráez et al. (2014), Sicot et al. (2008) and Bangga et al. (2015), who investigated the rotational effects on wind turbine blades experimentally and numerically. They all came to the conclusion that rotational effects, caused by centrifugal and Coriolis forces, have a major impact at the blade root and cause a shift of the separation point compared to the non-rotational case. It has been observed that rotational forces can lead to a stall delay and a smaller wake size, which leads to lift augmentation. Moreover, different airfoil types react differently to rotational forces.

The separated flow regime was identified as the most important flow regime regarding unsteady aerodynamic loads which affect harmonic run, energy efficiency and structural integrity. This flow regime is dominated by the dynamic stall phenomena, which causes high load peaks compared to steady or quasi-steady conditions. The peak loads are a direct result of the development of vortex structures at the leading edge. Dynamic stall is not a design condition for common wind turbines, but it does occur regularly. It is difficult to access numerically as well as analytically. To control dynamic stall the ability to control the developing leading edge vortex is needed.

Various different stall control mechanisms have been the focus of research. Chandrasekhara et al. (1998) investigated a dynamically deforming leading edge profile shape for dynamic stall control. Feszty et al. (2003) and Gerontakos & Lee (2006) demonstrated the ability of active trailing edge flaps for dynamic stall control. Nguyen (1998) investigated the concept of blade pitch control numerically. In the field of wind turbine research various concepts have also been investigated. Xu et al. (2016) performed experiments with a controlled flow jet at the suction side of an airfoil to suppress the development of vortices. Choudhry et al. (2016) compare three approaches in respect to their effectiveness; a vortex generator to produce vortices with reverse circulation compared to the dynamic stall vortex, an elevated wire at the leading edge to produce reverse spanwise vortices, and a cavity configuration with a cavity at the suction side near the leading edge in order to suppress leading edge vortex formation.

The ACP concept has been investigated by Wester et al. (2018a) and Cordes (2016) with respect to its usability for dynamic stall control. Cordes (2016) investigated an ACP model during pitch and plunge motion at high mean AoA's in the transition zone, while Wester et al. (2018a) investigated the ACP in the active grid tunnel of the University of Oldenburg under dynamic stall conditions. Both came to similar conclusions regarding ACP behaviour and impact. Wester et al. (2018a) documents a load reduction of 20% compared

to the rigid profile achieved with relatively small trailing edge amplitudes of about 3.5°. The impressive load alleviation is illustrated by high speed PIV measurements, which show how ACP operation leads to a better flow attachment within the dynamic stall cycle compared to the rigid profile, which damps the development of vortexes.

The ACP airfoil de-cambers due to the leading edge vortex formation, which damps the dynamic stall evolution compared to the airfoil in rigid condition. It can be assumed that the concept implemented in a rotor blade is favourable regarding the dynamic stall behaviour of rotor blades. However, this behaviour of the ACP under dynamic stall conditions has to date not been comprehensively or quantitatively investigated.

2.2.2 Analytical Approaches for Unsteady Aerodynamics

In the following subsection a short overview and summary of analytical approaches used to describe the lift response of an airfoil in unsteady flow are given. These approaches are based on the principles of thin airfoil theory. They are valid for two-dimensional periodic gusts with small amplitude. Furthermore, they describe the behaviour for attached flow only and can be divided into first order and second order transfer functions.

First order approaches assume a complete decoupling of steady and fluctuating flow, which leads to relatively simple closed form solutions. These approaches are derived for a thin plate without camber in a uniform flow and in general they are not applicable for thicker, cambered profiles which lead to flow separation. Three such analytic solutions and their applicability to wind turbine aerodynamics will be briefly presented, two first order solutions, Sears (1938) and Theodorsen (1935), and one second order solution, Goldstein & Atassi (1976) and Atassi (1984).

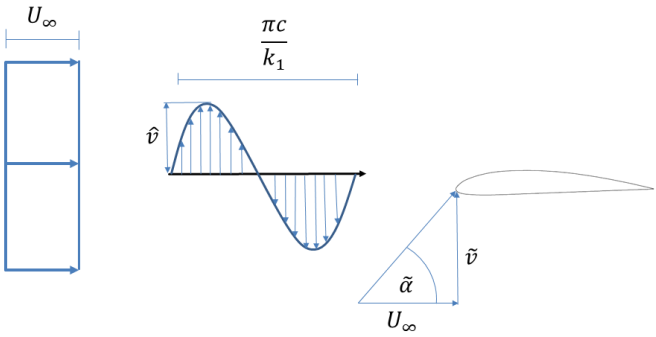

Figure 2.3: Inflow conditions according to Sears. Fluctuations in the normal velocity component $\tilde{v}$ with a reduced frequency k_1 impinge on the airfoil. The resulting angle of attack variations are represented by $\tilde{\alpha}$. The depiction is adapted from Wei et al. (2018).

Sears Theory

The Sears theory is an analytical solution for the problem of a flat plate in uniform flow responding to a gust scenario represented by a two-dimensional sinusoidal and periodic perturbation of the velocity component normal to the mean flow. The approach was developed in context with the practical problem of swinging bridges under specific unsteady wind conditions, which was evidently not explained by phenomena like the Kármán vortex street.

Figure 2.3 depicts the inflow conditions at a profile according to Sears. In the Sears scenario, the analytical description of the problem depends only on one reduced frequency k_1 pictured in Fig. 2.3 as a spatial perturbation of the v velocity component. The hats above the symbols indicate the amplitude of sinusoidal fluctuations of specific components of the inflow velocity.

Within the framework of the present study experiments were performed under such unsteady flow conditions in the active grid wind tunnel at the University of Oldenburg using the Clark-Y profile. These experiments and

their analysis is fully described in Wei et al. (2018). The results confirmed the Sears response, although the Clark-Y profile used in the experiments is thicker than the flat plate assumption of the Sears theory. This leads to the conclusion that the Sears function has practical importance not only for thin plates, but also for profiles commonly used for wind turbine blades. This assumption has yet to be systematically and comprehensively quantified and is a subject of future research.

One main goal of the experimental campaign was to determine whether the Sears theory could also be applied to the ACP profile. Recalling that the Sears theory assumes a periodic perturbation, such conditions arise on wind turbines due to the tower shadow, periodic passage through the atmospheric boundary layer and/or perturbations caused by yaw misalignment, i.e. a misalignment of the rotor plane normal to the mean wind velocity. Under these conditions, and assuming sinusoidal, two-dimensional, small amplitude perturbations, the Sears theory should be applicable. This is more likely the case near the rotor blade tips, since here all wind gust perturbations become relatively small due to the dominating rotational speed of the blade in the velocity triangle. On the other hand, none of the above-mentioned perturbation sources are strictly sinusoidal and moreover, the wind velocity is not always constant. In summary, the Sears theory may not be directly applicable for many gust scenarios.

2nd Order Transfer Function of Atassi

The Atassi solution and the main differences to the Sears theory have been discussed in detail in Wei et al. (2018). The practical importance in the framework of the present study is that the theory of Atassi allows for a fluctuation both of the inflow speed and the AoA. This is mathematically captured by introducing a sinusoidal spatial fluctuation of the inflow velocity in the direction normal to the mean inflow direction, characterised by the reduced frequency k_2. Still, the flow is prescribed as being two-dimensional and the perturbation is periodic and sinusoidal, but a changing inflow velocity in combination with

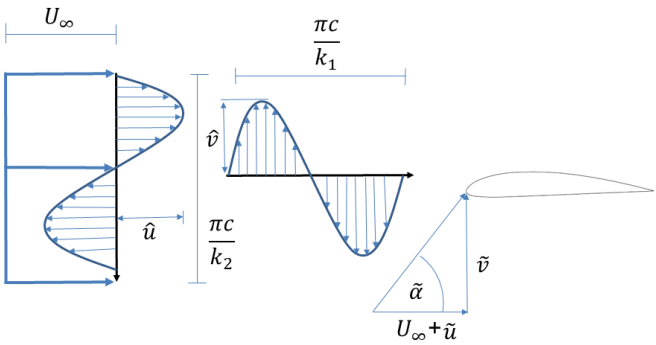

Figure 2.4: Inflow conditions according to Atassi. In addition to the normal velocity fluctuations from the Sears problem, streamwise velocity fluctuations with amplitude $\hat{u}$ and a reduced frequency k_2 are also present. The depiction is adapted from Wei et al. (2018).

an AoA fluctuation is a more realistic gust scenario to which a wind turbine blade is exposed. Especially considering radial profiles at the middle section of a rotor blade, where the flow can be assumed two-dimensional and attached, the Atassi solution may be applicable.

Figure 2.4 shows a schematic of the inflow conditions according to Atassi. In the Atassi solution the additional perturbation expressed by k_2 is coupled with the reduced frequency k_1 appearing in the Sears problem, a condition which allowed Atassi to obtain an analytic solution. In other words, the Sears problem is a special case of the Atassi formulation, for which $k_2 = 0$. To what extent this solution is directly applicable to wind turbine operation is not yet clear. The more general problem of arbitrary k_2 values is formulated in Goldstein & Atassi (1976), but not solved.

Theodorsen Functions

Theodorsen (1935) analytically described the lift response of a pitching and/or plunging airfoil in a uniform flow on the basis of potential flow theory. The lift response of such an airfoil can be determined by the Theodorsen function:

$$C(k) = F(k) + iG(k) \tag{2.5}$$

where $C(k)$ is a complex function with a real part $F(k)$ and an imaginary part $G(k)$, both of which are expressed in terms of Bessel functions. The reduced frequency k refers to the frequency of the profile motion and $\mathbf{v}(\mathbf{x}, t)$ expresses the induced velocity field. The Theodorsen function is directly applicable to flapping flight insofar as the flow remains attached and can be considered to be two-dimensional. The fundamental difference between the theory of Theodorsen and those of Sears and Atassi is that under the conditions addressed with the Theodorsen solution, all particles passing over the profile experience the unsteady change in boundary conditions simultaneously and to the same degree.

The transfer function h expresses the lift of a pitching or plunging airfoil in comparison to the quasi-steady lift encountered at the same geometric AoA, i.e.

$$h = \frac{L_{dyn}}{L_{qs}} = \frac{C_{L,dyn}}{C_{L,qs}} = h(C(k), \mathbf{v}(\mathbf{x}, t)) \tag{2.6}$$

and this function depends on both the Theodorsen function and the kinematics of the airfoil motion.

The Theodorsen function is undoubtedly relevant to wind turbine operation, since rotor blades experience plunging and possibly pitching motion through the blade bending and/or twisting or when the inflow is not exactly normal to the rotor plane, i.e. in yawed operation.

2.3 Wind Turbines with a Yawed Rotor Plane

The main practical challenge considering unsteady aerodynamic experiments is the generation of an adequate gust scenario. *Adequate* means in this context that it has to be reproducible and that it can be controlled with respect to a wide range of the characteristic parameters like inflow velocity, gust amplitude and frequency for example. Furthermore, the scenario should have practical relevance.

A gust generation approach which has been used in previous ACP research is the active grid technology. Such an apparatus has been developed at the University of Oldenburg and the experiments of Cordes (2016) as well as Wei et al. (2018) have been performed in cooperation with University of Oldenburg. A active grid is basically a set of airfoils mounted upstream of the test section, which can be controlled by drive units. The airfoils are moved according to a specified protocol, which leads to a given gust scenario. The nature of the incoming gusts is then characterised by direct velocity measurements in the test section, for instance using hot-wire anemometry. Further information about the functionality of the active grid technology can be found in Knebel et al. (2011), Weitemeyer et al. (2013) and Reinke (2017). A further promising and highly interesting approach to generate controlled gusts in a wind tunnel is to generate gusts using an upstream pitching/plunging airfoil, as described in Wei et al. (2019). The approach greatly reduces wake effects and the wind tunnel blockage encountered using active grid generators.

In general the complexity of such gust generators and the difficulties in implementation increase with the size of the test section and model. For experiments with the goal to validate analytic approaches to response of profiles to flow perturbations, relatively small and simple two-dimensional models are sufficient. However, for the investigation of turbines under realistic unsteady inflow conditions, a much larger experiment is required to realise a realistic turbine diameter.

Acknowledging these difficulties in generating appropriate gust scenarios at large scale, a choice has been made in the present study to restrict investigations to unsteadiness arising from a rotor plane yaw. This decision has the advantage that no gust generator is needed in the wind tunnel. The yaw case scenario is a practical, highly relevant scenario, because it is commonly encountered in real wind turbine operation. Micallef & Sant (2016) as well as Leishman (2006) describe the practical relevance of the yaw case scenario regarding the gust load problem. Butterfield et al. (1991) performed experiments with a wind turbine under a yaw angle of 30° and observed dynamic stall at the blades. Schreck et al. (2000) and Schreck et al. (2001) experimentally investigated the occurrence and the impact of dynamic stall phenomena on rotor blades caused by yawed rotor plane conditions. Galloway et al. (2013) investigated the combination of yaw and wave effects for a tidal stream turbine model.

The fundamental difference between experiments on a rotating model wind turbine and the previous experiments performed with the ACP is the three-dimensional character. Given this fundamental difference, it is instructive to consider what boundary conditions actually apply in the rotating frame arising from a yawed rotation plane. This discussion begins assuming a constant yaw angle and a constant inflow wind speed. Assuming first, that at all radial profile sections the flow remains attached to the profile, then the solutions of Sears, Atassi and/or Theodorsen may apply. Consider first the periodic bending of the rotor blade during rotation due to the fluctuating aerodynamic loading. This corresponds to pure plunge of the profile, suggesting a Theodorsen solution, whereby the plunge amplitude (and thus the Strouhal number) changes with blade radius. As the profile rotates from lee and luv side of the yawed rotor plane, a cross-stream velocity component is superimposed, which in one case acts towards the hub, in the other towards the tip. This corresponds in classical aerodynamics to a sweep condition and thus, the imposed sweep angle regularly changes sign. The additional velocity component relative to the blade arising from this effect will be termed the side-slip velocity, acting tangential to the leading edge of the rotor blade, i.e.

radially. Moreover, due to the bending movement of the rotor either 'into' or 'away' from the mean flow, both the speed and the AoA change periodically, which corresponds to the Atassi solution. So in summary, it appears that for the assumption of attached flow, a combination of Theodorsen and Atassi conditions, with a superimposed side-slip velocity is a realistic operational condition of wind turbine blades rotating in a yawed rotor plane.

Figure 2.5 shows an overview of a blade profile section in four positions of rotation within a yawed rotor plane. The yaw angle of the rotor plane is designated by ϕ, the angular rotor frequency with Ω and the chord length of a profile at a specific span position with c. In this representation we assume that the chord is aligned with the rotor plane, which effectively assumes that no local twist or pitch of the blade (τ) exists. Blade twist will be introduced in chapter 4.
A profile within the scenario of a yawed rotor plane undergoes an effective plunging and pitching motion relative to the inflow of the rotor plane, which results in a overlaid sliding angle fluctuation induced in the profile inflow. The plunging direction parallel to the inflow velocity at the rotor plane is designated by x_{plunge}.
Figure 2.6 builds on figure 2.5 and shows the definition of angles and velocities acting on a profile section of a rotor blade under yawed conditions in the four characteristic positions of a stroke motion. The velocity v_2 is the total velocity in the plane of rotation, using the nomenclature of Betz (1924).The velocity component into the rotor plane, i.e. the slide-slip velocity in the blade span direction, is denoted v_{Tr}, with a fluctuation amplitude between the maximum and minimum values of Δv_{Tr}.
v_2 is divided into the component v_{Tr} and the component v_2' in the profile plane due to the yaw angle ϕ. v_{Tr} has a fluctuating amplitude over the rotation, which induces the fluctuating side-slip angle β at the profile. The total velocity in the profile plane v_{T2D} results from the magnitude of v_2' and the angular velocity in the profile plane Ωr. At the top and bottom dead centre of the profiles flapping movement the component v_{Tr} takes a maximum value, but acts once from the blade root towards the blade tip and once from the blade

tip towards the blade root. In the mid-upstroke and mid-downstroke position the component v_{Tr} becomes zero.
In the mid-upstroke and mid-downstroke positions the velocity v_{plunge} induced by the stroke movement and acting parallel to v_2 takes a maximum value. During the downstroke v_{plunge} acts in the direction of v_2 and during the upstroke it acts against v_2.
At the mid-downstroke position v_{T2D} takes a maximum value while the angle of attack α reaches its minimum. At the mid-upstroke position α reaches its maximum and v_{T2D} becomes minimum. This behaviour arises due to the yawed rotor plane and results from the pitch movement of the profile relative to v_2 during the rotation. The influence of v_{plunge} on α and v_{T2D} strongly depends on the yaw angle ϕ, the local blade radius r and the angular frequency Ω.

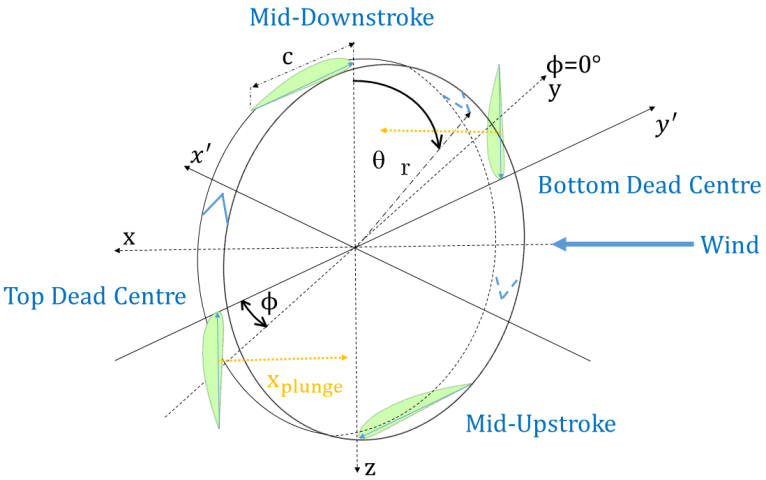

Figure 2.5: Overview of a profile section in 4 positions of rotation within a yawed rotor plane. The local blade twist angle τ is assumed to be zero, thus the chord is aligned with the angular rotation vector $\Omega(r)$. The yaw angle is denoted by ϕ. The azimuthal angle is denoted by θ. The plunging direction parallel to the inflow velocity of the rotor plane is designated by x_{plunge}

Regarding separated flow conditions, the yaw case scenario often defines the

boundary and initial conditions leading to dynamic stall. Leishman (2006) describes this problem in detail. One reason for dynamic stall onset is that the yawed rotor plane provokes high AoA fluctuations especially at the root. Another reason, which maybe is not as obvious, is the impact of the radial side-slip velocity component. Leishman (2006) points out that these velocity components under separated flow conditions cannot be neglected, like it is often assumed for attached flow conditions.

Consider an outer profile section, where the flow can be approximated as two-dimensional and attached and conditions prevail representing the Theodorsen problem of a plunging airfoil. In that case a formulation to determine the reduced frequency at the specific profile sections of a blade is needed. An adequate formulation is given by Leishman (2006) as follows

$$k(r) = \frac{\Omega c}{2(\Omega R r + U_\infty sin\phi)} = \left[\frac{1}{r + \frac{sin\phi}{\lambda}}\right]\frac{c}{2r} \tag{2.7}$$

where R is the radius of the rotor blade and λ is the Tip Speed Ratio (TSR). With equation (2.7) it is possible to compute the reduced frequency $k(r)$ as a function of span position r, which depends on the local chord length c, the Tip Speed Ratio λ, and the the rotor plane yaw angle ϕ. Knowing these quantities enables equations (2.5) and (2.6) to be solved.

This means that for a yawed rotor plane, unsteady conditions can be characterised and determined by adjusting the yaw angle ϕ, the wind speed U_∞ or the rotational speed of the turbine; hence, the tip speed ratio λ. One rotor rotation defines an upstroke and downstroke of the Theodorsen plunging problem seen from the perspective of a radial profile section. The plunge amplitude (without bending) depends on the radial blade position r and the yaw angle ϕ and is given by

$$x_{plunge} = 2(rsin\phi) \tag{2.8}$$

The local position within a plunge cycle $h(\theta)$ depends on the azimuthal angle θ. The velocity induced by plunge motion, v_{plunge}, depends on the

azimuthal angle θ and the rotor frequency f. The values are given by equations (2.9) and (2.10). (2.9) refers to the scenario experimentally investigated in this thesis and describes the conditions shown in figure 4.7

$$x_{plunge}(\theta) = r sin\phi(1 + cos(\theta + \pi/2)) = r sin\phi(1 + cos(2\pi\Omega t + \pi/2)) \quad (2.9)$$

$$\frac{dx_{plunge}}{dt} = v_{plunge} = h(\theta)f \quad (2.10)$$

Cordes (2016) has investigated a plunging ACP model regarding its gust load alleviation capability and presented promising results. During the downstroke the profile de-cambers and counteracts the load increase caused by an increase of AoA. During an upstroke the profile cambers and counteracts the load decrease caused by a decrease of AoA.

Cordes (2016) emphasises that especially for the plunge motion, the inertial mass forces of the flap augments the ACP actuation in the desired manner. The ACP under Theodorsen conditions is activated by inertial forces caused by airfoil motion and aerodynamic forces. The influence of inertial forces depends on the ACP design. If the flaps are balanced with respect to their axis of rotation and the mass of the flaps can be kept relatively small, mass forces influencing the ACP behaviour can also be kept accordingly small. Furthermore, an increasing load damping effect compared to the rigid profile could be observed with increasing reduced frequency.

The results of Cordes (2016) motivate experiments with a plunging airfoil by the fact that there is a plunging and pitching motion of profile sections due to deformations of the blade caused by bending and torsional loads. Similarly, the Theodorsen problem of a plunging airfoil is an analytical approach to describe the aerodynamically load response of the profile sections of a rotor blade under yawed conditions in an attached flow regime. Accordingly, the ACP should operate in an advantageous way with respect to gust load alleviation.

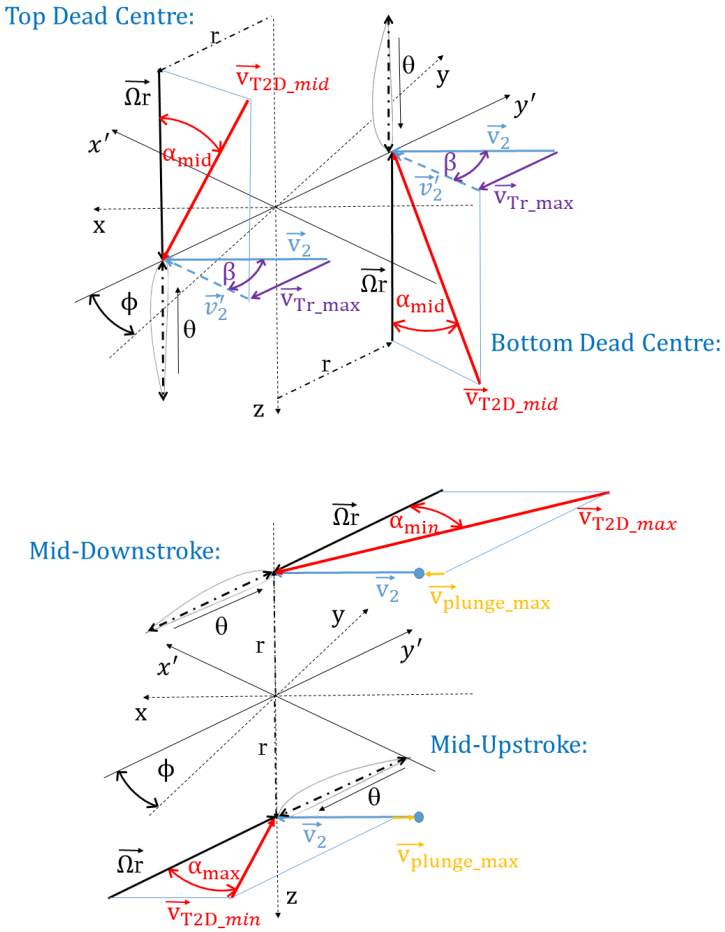

Figure 2.6: Definition of angles and velocities acting on a profile section of a rotor blade under yawed conditions. The local blade twist angle τ is zero, thus the chord is aligned with the angular rotation vector $\Omega(r)$. The yaw angle is denoted ϕ. The azimuthal angle is denoted θ. The representation refers to figure 2.5

3 Experimental Apparatus and Methods

The following chapter comprises five sections. The first describes the experimental setup, including the wind tunnel, the wind turbine and the construction of the rotor blades with embedded adaptive camber mechanisms. The second section addresses the instrumentation used in this study, including their calibration. A section is then included which summarizes the numerical tool used to complement the measurement data for situations and positions for which measurement equipment malfunctioned. The next section gives an overview of the test cases performed and the final section describes how the data was evaluated, including uncertainty estimations of the measured quantities.

3.1 Experimental Setup

The experimental setup consists of a model research turbine with ACP equipped rotor blades, extensive measurement equipment and sensor technology. In the settling chamber of the large wind tunnel of the Technische Universität Berlin, there is a turntable where a turbine can be mounted and the rotor plane yaw angle ϕ can be manually adjusted in the range $\pm 30°$ in steps of $5°$. The Berlin Research Turbine (BeRT) is mounted in this settling chamber, as pictured in figure 3.1.

3.1.1 Windtunnel

The wind tunnel at the TU Berlin is driven by a 450 kW fan. The settling chamber, which acts as a test section for the BeRT, has a cross section of 4.4 m x 4.4 m and a total length of 5 m. The turbulence intensity in the con-

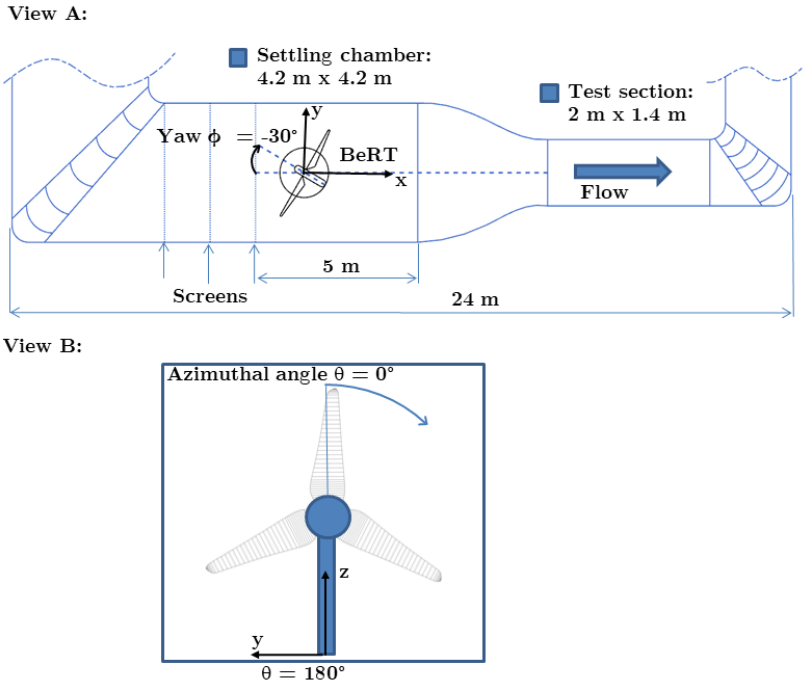

Figure 3.1: View A shows of the wind tunnel and Berlin Research Turbine (BeRT) from a top view. The BeRT is shown in the settling chamber with a rotor plane yaw angle ϕ of -30°. View B shows the BeRT from the flow direction onto the rotor plane. The centre line of the tower is located at an azimuthal angle θ of 180°.

ventional test section is lower than 1.5%, therefore the turbulence intensity in the test section must be assumed to be higher, but is not known. The flow in the settling chamber is not completely uniform over the cross-section - a consequence of being situated immediately downstream of corner four of the wind tunnel. Furthermore, the wake of the model turbine will be influenced by the downstream nozzle into the conventional W/T test section. These effects will be discussed further below.

Conducting these experiments in a closed wind tunnel undoubtedly introduces blockage effects on the absolute values of power coefficient and presumably also on the overall velocity field before and after the turbine. Considerable work has been reported on the influence of blockage on model wind turbines (Chen & Liou (2011); Hirai et al. (2008); Sarlak et al. (2016); Schreck et al. (2007); Schümann et al. (2013)) and a conservative estimate is that blockage above 5% can have significant impact on turbine performance. While this limitation is acknowledged in the present study, the major focus is on comparative measurements, i.e. comparing performance with and without actuation of the adaptive camber profiles. Thus, the blockage issue has not been pursued any further. Nevertheless, this does present an obstacle when comparing to numerical simulations, if the simulations do not also include the wind tunnel contours experienced by the turbine, as in the comparisons drawn with results obtained using the code QBlade (see section 3.3) in the present study.

For all of the tests reported in this study the wind tunnel was operated at a fan speed of 720 *rpm*. Unfortunately the velocity field across the settling chamber at this fan speed was not well documented by the wind tunnel operator and therefore only a nominal inflow velocity can be estimated. This is not considered a serious drawback, since the local blade incident velocity (magnitude and AoA) was measured directly with five-hole pressure probes. (see section 3.2.1). Nevertheless, to give some impression of the flow quality in the settling chamber, results are reported here from a concurrent investigation (Klein et al. (2017)).

Figure 3.2 depicts the velocity field at a plane 1.29 m upstream of the rotor plane for the case of an un-yawed turbine and for a fan speed of 520 rpm, measured using hot-wire anemometry. It can be observed that the velocity field is neither axisymmetric nor uniform across the cross-section. From the middle of the settling chamber to the tunnel walls there is a velocity difference of about 0.8 m/s. Two pitot tubes are permanently installed in the settling chamber, as shown in figure 3.2. At a fan speed of 720 rpm these pitot probes yielded a velocity of approximately 9.0 m/s. Thus, the inflow velocity in the middle of the tunnel can be estimated to be about 8.5 m/s.

This estimate was then substantiated by comparing AoA predictions using the simulation code QBlade (see section 3.3) with the measured AoA values throughout one turbine rotation. The comparison was made at 50% blade radius, assuming at this position the influence of the hub and tip flows would be minimal and the flow around the blade would best approximate the two-dimensional assumption made by QBlade. These results are illustrated in figure 3.3. As can be seen in this figure, the overall agreement is not good, for reasons which will be discussed later; however, the estimate of $U_\infty = 8.5\ m/s$ is a reasonable value for reference.

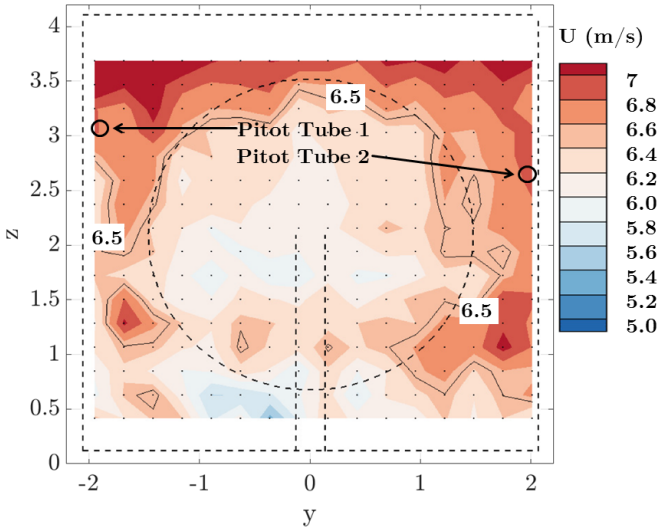

Figure 3.2: Hot wire measurements of a plane 1290 mm upstream of the rotor plane. Turbine was adjusted at a rotor plane yaw angle of 0°. The tunnel fan operated at 520 rpm. Hot wire data in the picture is taken from Klein et al. (2017). Position of the Pitot tubes used in the actual measurements is marked. Heads of the Pitot tubes are located in a plane 1100 mm upstream of the rotor plane.

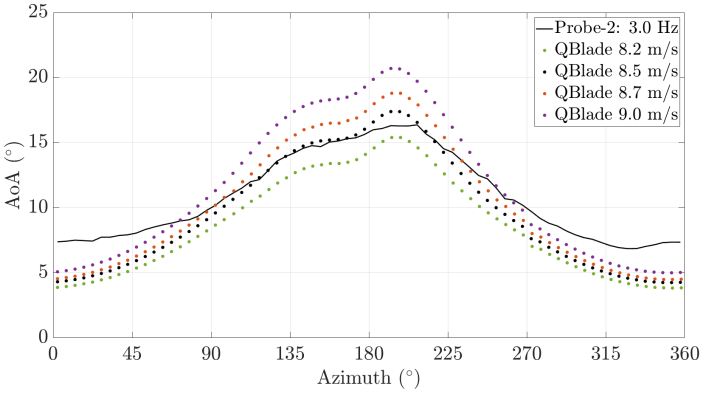

Figure 3.3: Measured AoA with five-hole probe 2 compared with predicted AoA using QBlade and assuming different wind tunnel velocities. The rotor frequency is 3.0 Hz

3.1.2 Berlin Research Turbine

The BeRT is a three bladed Horizontal Axis Wind Turbine (HAWT) with a design tip speed ratio of 4.6. The rated rotational speed is 180 rpm. The turbine has a rotor diameter of 3 m and an effective blade length of 1285 mm, which corresponds to a hub diameter of 430 mm. The blades are designed using only one profile over the entire span. The Clark-Y profile has been chosen because of its favourable aerodynamic behaviour and its qualities as a flap profile in the planned Reynolds number range.

The maximum Inflow wind speed of 8.5 m/s is relatively low for a turbine with a diameter of 3 m and an operational range of 100 rpm to 250 rpm with respect to the Reynolds number over the blade radius. The Clark-Y meets the demands to have a relatively large thickness of 11% and to be functional in a Reynolds range between 150,000 and 300,000. In other words, the profile is aerodynamically functional and yields a large cross section with sufficient space for ACP mechanics and sensors. Furthermore, the flat pressure distribution simplifies manufacturing as well as a proper arrangement of the leading

and trailing edge flaps relative to each other. The blades are mounted on the hub by threaded steel pins and the pitch angle can be adjusted manually, using a nonius scale.

The BeRT turbine is a small wind turbine which can only be operated at relatively low wind speeds. To achieve an adequate Reynolds number, the chord length of the blade profile is therefore relatively large. Moreover, also the hub is large, providing enough space for the data acquisition equipment. Thus, although the proportions of the model turbine are not comparable to real wind turbines, the performed measurements of the ACP mechanism as a gust load alleviation approach are of comparative nature, with reference to a rigid profile shape. The crucial point is to provide a realistic gust load scenario, leading to controllable AoA and velocity fluctuations on the blade profile sections.

There are approximately 18.75 cm^3 space for measurement equipment available, where a cRIO-9068 and a DAQ-9188 platform with 9220 modules are mounted. These are data acquisition modules from National Instruments®. The cRIO-9068 and its modules rotate and acquire data from the blades. The data is transmitted wireless to a remote, stationary system. The DAQ-9188, which is mounted in the non-rotating system, collects additional data. The tower height is 2.1 m with a diameter of 0.273 m.The rotor overhang is 0.5 m.

3.1.3 Rotor Blades with Adaptive Camber Profile Segments

Three unique rotor blades have been designed and manufactured for the experimental program with the BeRT. The blade design is based on a spar structure consisting of two aluminium beams which are connected by polyamide fins printed by laser powder bed fusion.

The carbon fibre composite (CFC) shells for the blade are manufactured by

vacuum infusion process (VIP). The challenge was to include a large number of pressure tubes in the blade shell. There are up to 60 tubes distributed over three radial positions integrated into one blade. The combination of the spar structure with the CFC shell guarantees a high stiffness and a relatively high eigenfrequency of 42 Hz. Furthermore, the construction provides an adequate mount for extensive mechanics and sensor equipment. To manufacture such a complex unique design, where different materials are combined with a fibre compound structure, numerous preliminary material tests were necessary. In this regard, the theoretical background for these tests is well summarised in Schürmann (2007).

Blade-1 is conceived as a baseline blade without ACP sections. Like all other blades, it is equipped with three service holes at three radial measurement profile sections at 30%, 50% and 70% of the blade radius. On Blade-1, there are five-hole pressure probes mounted to capture the three-dimensional Inflow at the respective profile sections.

Blade-2 is equipped with one ACP section from 60% to 80% of the blade radius. The assumption is that load alleviation at this blade section will be most effective, since at the tip the gust will be less pronounced in the total velocity vector, thus reducing the invoked bending moment, and at the root the moment arm of fluctuating loads will be less. The blade provided also the measurement data used in Klein (2019) for comparison to numerical simulations of the experiment. Figure 3.4 shows Blade-2 in the test section of the wind tunnel at TU-Darmstadt during preliminary tests for the rotor campaign.

Blade-3 is equipped with three ACP sections equally distributed from 20% to 80% of the blade radius. The design is the result of the consideration that unsteady aerodynamic phenomena initialised at inner radial blade sections can influence the aerodynamic behaviour at the outer sections. That means that there can be situations, when critical gust loads at the root section can be prevented by controlling the overall lift distribution.

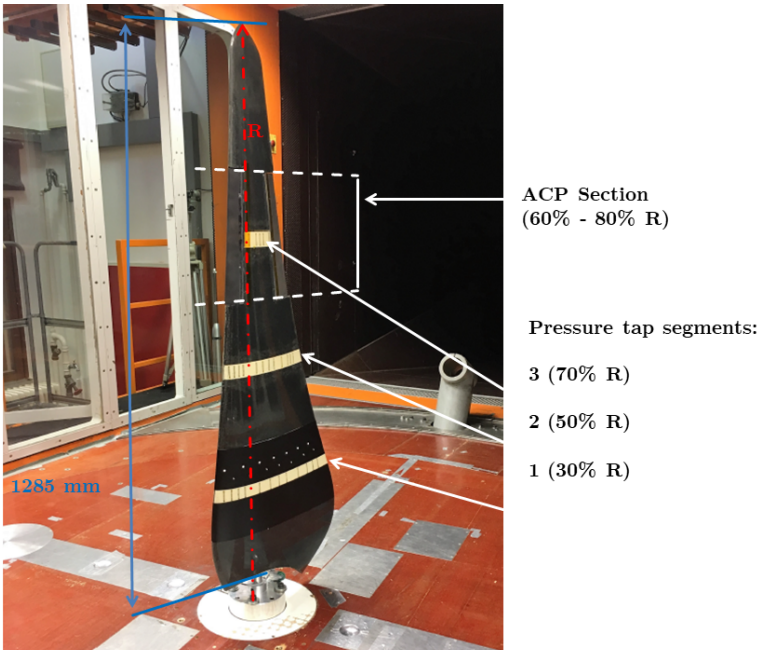

Figure 3.4: Blade-2 with an ACP section from 60% to 80% of the blade radius in the wind tunnel at TU Darmstadt during preliminary tests. The shell integrated pressure tap segments are clearly visible at three radial sections.

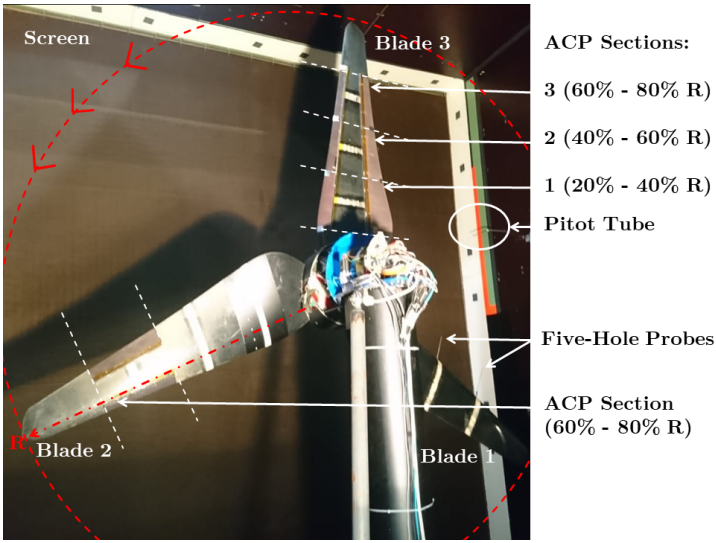

Figure 3.5: ACP rotor blades installed on the BeRT turbine. The picture is taken downstream of the rotor plane looking upstream.

The blade design is based on blade element theory with the inherent assumption that the single elements do not have any mutual influence. This assumption is not applicable in reality, especially not in an unsteady gust scenario. While Blade-2 is also the subject of numerical studies, at least in the linear region, the behaviour of Blade-3 is numerically not presently accessible and the results uncertain, because of the interaction of a multitude of unsteady phenomena. Figure 3.5 shows The BeRT turbine equipped with the rotors for the experimental campaigns.

In integrating the ACP concept into the rotor blades it was important to insure that the mechanisms did not affect the deformation behaviour of the blade, especially compared to the rigid blade. The optimum is a blade that can be assumed to be equivalent to a rigid profile during operation. To achieve that, the decision for a centre pin design was made. A hole through the neu-

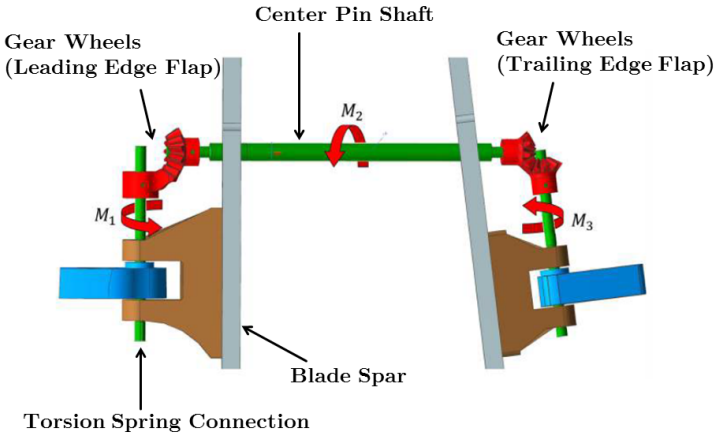

Figure 3.6: Principle of the coupling mechanism used to implement the ACP concept in the rotor blades

tral fibre of a spar structure allowed a centre pin shaft to be mounted, which least influenced the structural integrity of the blade.

One of the main challenges in realising the ACP is to design a proper coupling between the leading and trailing edge flaps. The present mechanism was realised using beveled gears and linkages. Bevel gears are common in the automotive sector, because of their inherent compactness and the homogeneous power transmission. Both compactness and a homogeneous transmission of the aerodynamic moment acting at the leading edge to the trailing edge flap are basic design requirements for the ACP mechanism, which makes the centre pin design the logical solution. Figure 3.6 shows the principle of the centre pin coupling mechanism used in the blade models.

For a twisted rotor blade it is not possible to use standard bevel gears, where the shaft axes are arranged 90° to one another. One pair of gears must be adapted to the radial blade position of the coupling mechanism. These gears are manufactured by laser powder bed fusion. The wheels are made of

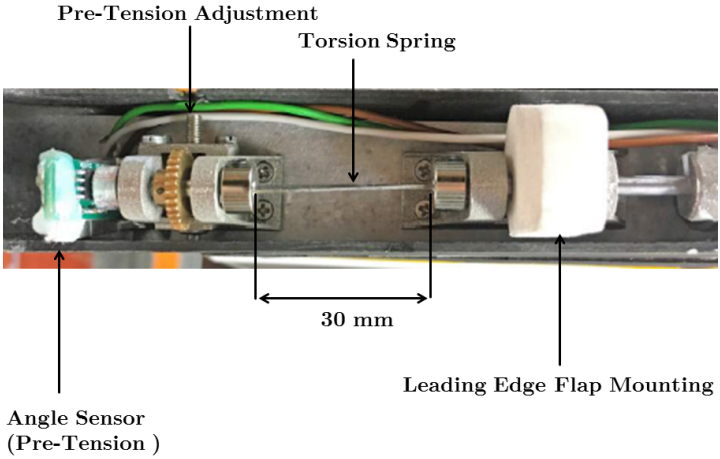

Figure 3.7: Spring mechanism of Blade-2 including pre-tension mechanism and torsion spring connected to the leading edge flap shaft. At the left side of the picture the angle sensor for pre-tension measurement can be seen.

metal instead of polyamide to reduce play in the coupling mechanism. The theoretical basics for the design of the special gears in a twisted rotor blade are taken from Roth (1998). The ACP sections had an coupling ratio $n = 2$ in all the experiments performed.

A further challenge relates to the spring mechanism, since an adequate spring behaviour must be achieved with very little spring deformation. Like all components, the spring mechanism has to be extremely compact and practically free of clearance. A torsion spring fulfils the requirements best and fits in the overall concept. It is connected to the leading edge flap, since the available space at the trailing edge is too small. The pre-tensioning is realised by a self-locking worm gear mechanism, similar to guitar string tensioners. Figure 3.7 shows the spring mechanism used in the blades.

3.2 Instrumentation

The instrumentation used in the present study can be divided into the following functional groups:

- Measurement of three-dimensional blade incident flow at various profile sections of the blade
- Measurement of the trailing edge flap angle
- Measurement of the root bending moments
- Measurement of the pressure distribution at profile sections of the blade

The measurement of the local incident flow at selected positions on rotor Blade-1 is based on five-hole pressure probes and a wireless transmission system to send data from the rotational to the stationary system. The electronics and pressure sensors are placed directly at the service caps on the blade to insure short tubes between the pressure taps and the sensors. This prevents damping effects and rotational effects of the air mass in the tubing.

The movement of the ACP flaps is based on Hall effect angle sensors, capturing the flap angle and the pre-tension of an ACP section.

The root bending moment is the main measurand to show the practical effectiveness of the ACP mechanism as a gust load alleviation approach. It is measured by two strain gauge bridges arranged 90° to each other.

The pressure distribution over the suction and pressure sides of the profile, captured at specific radial sections, and the resulting aerodynamic lift is the only measured quantity which is independent of mass forces. The pressure distribution provides direct information about the local aerodynamic forces acting on the profile and also indicates the state of the flow (e.g. attached or separated).

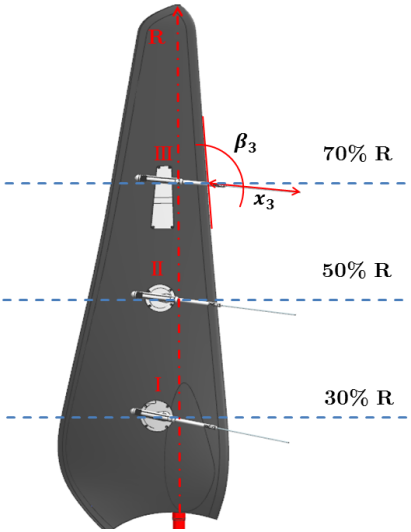

Figure 3.8: View of the pressure side of the baseline Blade-1 with five-hole probes installed at the service caps. The probes are installed with an initial inclination angle β_0 to compensate the sweep angle caused by the probe head protrusion ahead of the leading edge.

3.2.1 Measurement of the Incident Flow on Blades

Figure 3.8 shows the pressure side of Blade-1 with three five-hole pressure probes installed at 30%, 50% and 70% span. The position of the cone shaped probe head is defined by an inclination angle β_0 and a distance x_0, both with respect to the leading edge. The angle β_0 depends on the radial position of the probe and compensates the initial sweep angle induced by the rotation and the distance between the leading edge and the probe head. Table 3.1 provides the geometric positions of the probe heads.

For all pressure measurements differential pressure sensors of type HCLA2x5DB have been used. The sensors are pre-amplified and bidirectional in a range of $\pm 2.5\ mbar$. The HCLA2x5DB provides a full scale analogue output signal of $5\ V$. For the five-hole probes the high pressure port is normally connected to

Probe	Radius [%]	β_0 [°]	$x_0[mm]$
1	30	100.2	150
2	50	97.8	183
3	70	96.2	186

Table 3.1: Geometric specifications five-hole pressure probes

a probe tube and the low pressure port is connected to the static pressure of the flow captured by a Pitot-tube in the test section.

The tubing nomenclature used for the pressure probes is pictured in Fig. 3.9. To obtain angle information only, sensor 2 is not necessary. To obtain velocity information it is necessary to know the static pressure with respect to the probe pressure. Sensor 2 is located in the hub to make sure that no air column exists, because a longer tube in that case is unavoidable. The high pressure port of sensor 2 is connected to probe tube 2, while the low pressure port is connected to the static pressure of the flow.

The static reference pressure is captured by two Pitot probes which are connected to each other and in that way provides practically a mean static pressure of the inflow. The Pitot probes are mounted on the tunnel walls on both sides of the turbine. Figure 3.10 shows the exact position of the Pitot tubes used during the campaign with respect to the turbine. Blade-1 equipped with the five-hole probes is also pictured in this figure. The Pitot tubes on the tunnel walls have been used for turbine inflow measurements and as a reference pressure.

The blade incident flow measurement includes a wireless data acquisition system, which can be operated independently from the BeRT data acquisition system. The acquisition system integrated into the blades is based on an Arduino Nano® micro-controller in combination with an Xbee® WLAN module. The maximal sample rate is 700 Hz. The micro-controller has a resolution of 10 $bits$ and maximum data rate of 72.2 $Mbps$. The 12 V power supply

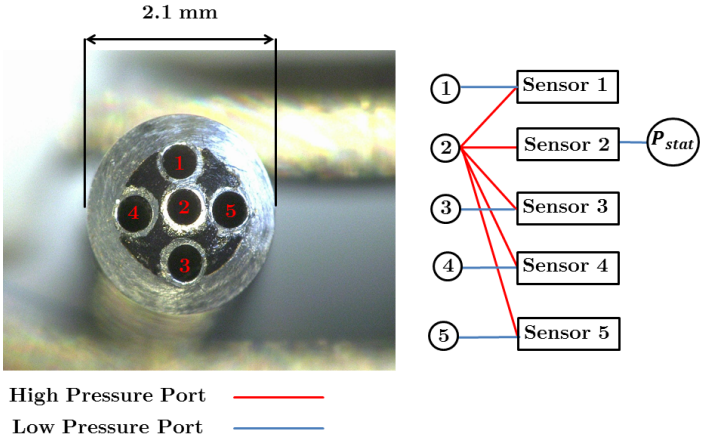

Figure 3.9: Tubing of the five-hole pressure probes. The image shows the probe head. Capillary stainless steel tubes are positioned manually. The space between the tubes is filled with resin. The cone-shaped head of the probe is turned on a lathe.

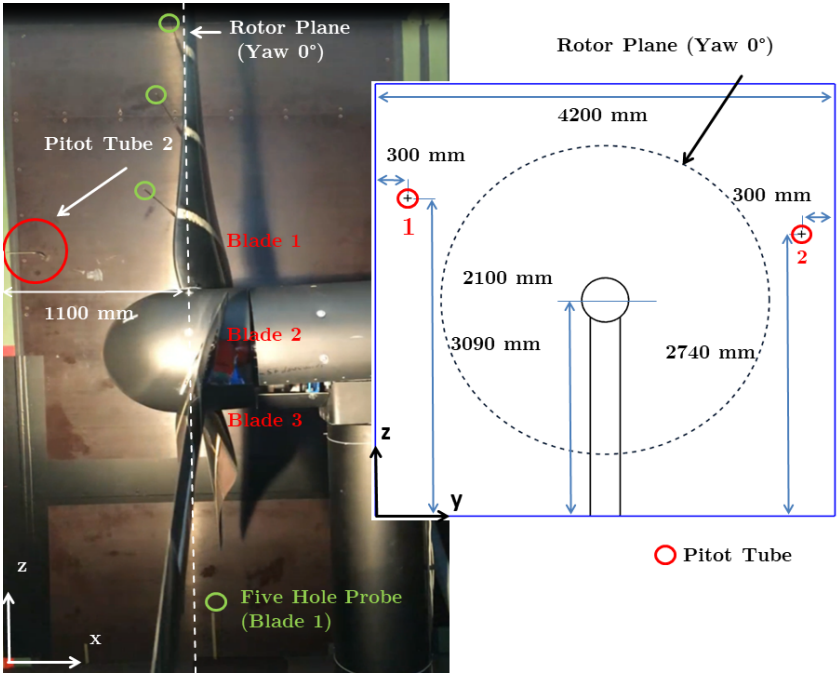

Figure 3.10: Position of the Pitot tubes used for inflow measurements and as a reference pressure source for the five-hole probes on Blade-1. The photograph shows the BeRT turbine equipped with three blades.

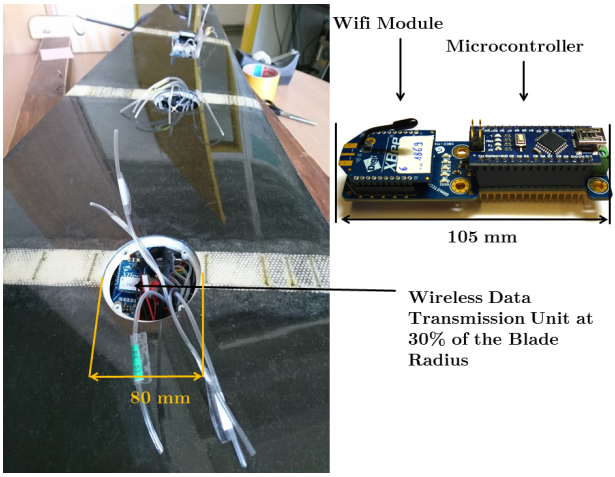

Figure 3.11: Wireless data transmission unit for blade incident flow measurements with five-hole pressure probes.

is taken from the hub. Detailed information about the wireless modules and micro-controller can be found in Bell (2013). For more general information about such acquisition equipment Horowitz & Hill (2015) and Scherz & Monk (2016) are recommended. Figure 3.11 shows the wireless data transmission unit and how it is integrated into Blade-1.

The calibration procedure has been conducted in the large low-speed wind tunnel of the TU Darmstadt. The probes are calibrated for AoA (α) as well as for the side-slip flow angle β. An angle range of $\pm 18°$ was used, which captures all flow regimes expected on the blades, from linear to fully detached. The measured incident velocity data is always related to the leading edge position of a specific blade and span position. Figure 3.12 shows the deviation between the measured incident angles, $\delta\alpha$ and $\delta\beta$ and the geometrically set incident angles. From these data no obvious systematic error was observed. The uncertainty due to stochastic errors, estimated at 95% confidence (1.96σ) is $0.2°$.

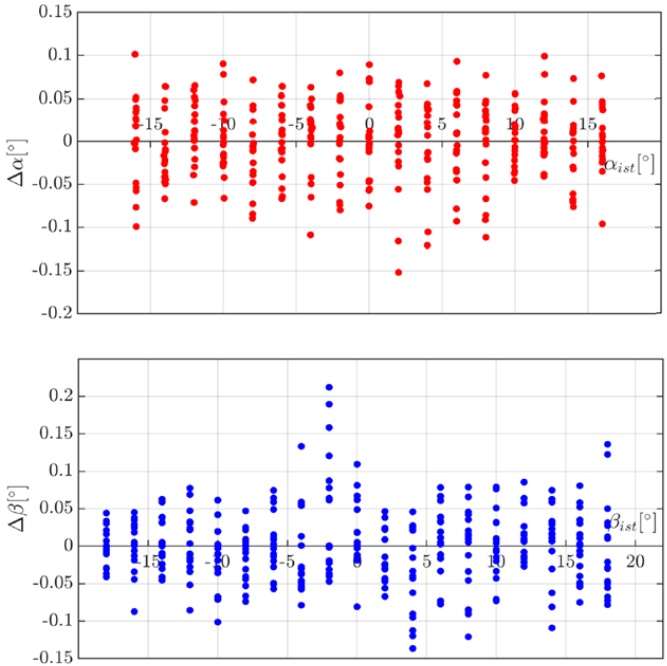

Figure 3.12: Steady calibration of five-hole pressure probes. The geometrically set angles during calibration apply on the X axis. The deviation between the measured angles and geometrically set angles applies on the Y axis.

3.2.2 Measurement of Flap Angle and Pre-tension

The measurement of flap angle and pre-tension is made with Hall-effect angle sensors. The torsion bar spring system, which is directly connected to the shaft of the leading edge flap, allows direct measurement with two angle sensors, one connected to the flap shaft and one connected to the shaft of the pre-tension unit. Until the mechanical stopper for the adjustment of the initial pre-camber is reached, both shafts turn and both sensors register angle changes. When the mechanical stopper is reached the sensor at the flap shaft stops at the initial pre-camber angle and the pre-tension sensor registers the pre-tension angle while the torsion bar continues to twist. The trailing edge flap angle, γ is obtained by multiplying the measured leading edge flap angle by the coupling ratio ($n = 2$) and assuming no play in the coupling mechanism.

The AMS5162 rotary Hall sensor, with a full scale analogue output of 5 V, is used for flap angle measurements. According to manufacturer specifications, this sensor has an uncertainty of 0.09° (95% confidence). The angle sensors on Blade-1 are programmed for a range of 20°, which leads to a resolution of 0.25 $V/°$, for which leading edge deflections can be detected. The angle sensors of Blade-3 are programmed for a range of 30°, which leads to a resolution of 0.18 $V/°$. Offsets in measurements caused by manufacturing tolerances and manual adjusting inaccuracies are estimated as being at most ±1°.

3.2.3 Measurement of Blade Root Loads

The root loads are measured by two bridges of strain gauges, which are applied at four milled planes of the blade root shaft close to the blade mount at the hub. The shaft is located at 30% of the profile chord and the strain gauges at 13.3% of the blade radius. At a blade pitch angle of 0° the plane of one bridge is normal to the rotor plane and the two bridges are arranged at 90° angle to each other. All experiments are performed with a blade pitch angle of 0° and in that case the strain gauges yield the in-plane and out-of-plane

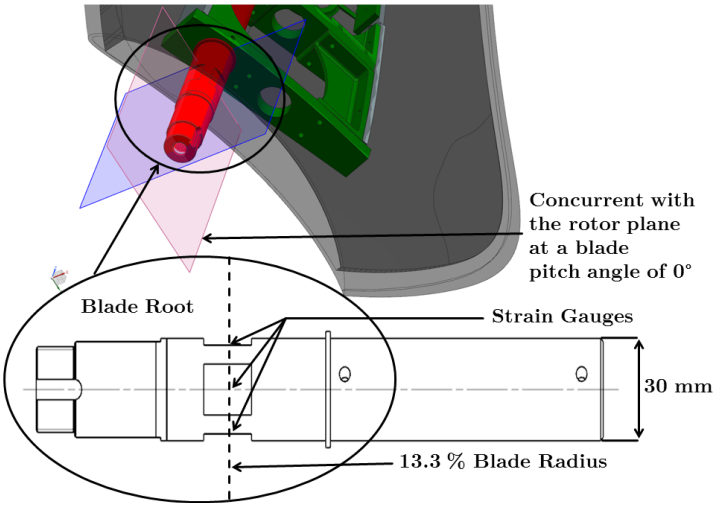

Figure 3.13: Position of the strain gauges on the blade root shaft. If a blade pitch angle of 0° is adjusted, the signals of the strain gauges correspond to the in-plane and out-of-plane root bending moments respectively.

root bending loads. The data is of qualitative character and the strain gauges are not calibrated. Figure 3.13 shows the location of the bridges. The root bending loads can be measured on all three blades in the same way.

The out-of-plane root bending factor (OPRB) is defined by

$$OPRB = \overline{y}(\theta)\frac{1}{\overline{y}_{rigid-max}} \tag{3.1}$$

where $\overline{y}(\theta)$ is a mean of the bridge voltage gathered during a run within an azimuthal angle interval centered at θ (see also section 3.5). $\overline{y}_{rigid-max}$ is the maximum mean measured bridge voltage on a blade using a rigid profile.

3.2.4 Measurement of Profile Pressure Distributions

The rotor blades are equipped with shell integrated stainless steel pressure tubes. The first layers of the laminate consist of a hand laminated glass fibre

layer. The transparency of glass fibre allows the subsequent manual drilling of the pressure taps from the outside into the embedded tubes. The tubes are fixed at the glass fibre layer with epoxy glue. The accurate positioning of the tubes at a specific chord position is realised by a special laser cut fleece mat. The cut is taken from a CAD file and contains slots for the tubes at the designated positions. After the tubes and the cuts are arranged and fixed in the mould, the carbon CFC layers are carefully prepared for the vacuum infusion process.

If a pressure tap is positioned on a flap or service cap, the tap is integrated into the SLM part and the steel tube for the connection to the silicon tube is glued at the printed component. The steel tubes have an outer diameter of 1.2 mm and an inner diameter of 1 mm. The pressure taps in the shell have a diameter of 0.5 mm. The steel tubes are limited in length and are connected to silicon tubes leading to the hub, where a pressure box with 32 differential pressure sensors are mounted within the rotating system. The static pressure of the flow, which acts as a reference pressure, is guided through a slip ring to the rotational system.

The data acquisition for the profile pressure distribution is influenced by rotational forces. Methods to compensate the data for this influence are still in progress; hence, the data is of qualitative character only and can be used for comparative considerations, but not for quantitative lift determination. Considering the uncertainties regarding the profile pressure data, the decision has been made to not present and discuss the data within the framework of this thesis. Figure 3.14 shows the general distribution of pressure measurement positions. Pressure distributions can be measured at 30%, 50% and 70% of the blade radius on all three blades. Table 3.2 contains the pressure tap positions in percent of chord.

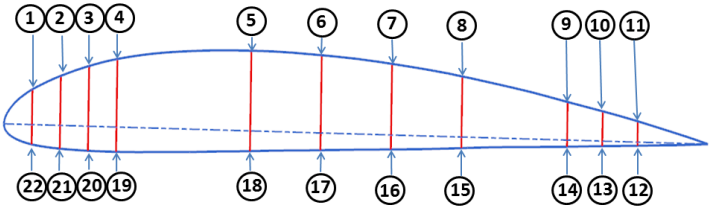

Figure 3.14: Distribution of pressure taps at specific radial blade positions.

Number	Position [% chord]	Number	Position [% chord]
1	4	11	90
2	8	12	85
3	12	13	80
4	16	14	65
5	35	15	55
6	45	16	45
7	65	17	35
8	80	18	16
9	85	19	12
10	90	20	8
		21	4

Table 3.2: Position of pressure taps.

3.3 Complementary Numerical Simulations

Although the focus of the present study was on experimental investigations, numerical simulations were conducted to check the plausibility of selected measurement results. Furthermore, because not all instrumentation was available throughout the entire test campaign, simulation results have been used to estimate local on-blade velocities at positions where no measurement data was available. For these simulations the tool QBlade was used.

QBlade is a code for the design of wind turbines developed at the TU-Berlin (Marten et al. (2010), Marten et al. (2015) and Marten et al. (2016)). The code is based on the nonlinear lifting-line free vortex wake model (LLFVW) as described by van Garrel (2003). Forces acting on the blade are extracted from tabulated lift and drag polar data. The lift and drag polar data for the Clark-Y profiles is obtained using XFOIL (Drela (2014)), whereby $N_{crit} = 9$. Viscous diffusion in the wake is accounted for through vortex core growth terms. The tower shadow is taken into account using a model from Bak et al. (2001). Unsteady aerodynamics and dynamic stall are introduced through the ATEFlap model, as described in Wendler et al. (2016). However, in the computations in the framework of this study, convergence with the dynamic stall model activated could not be achieved; thus, this model was not activated. An azimuthal angle discretization of 5° was chosen as a compromise between computational efficiency and accuracy. The same discretization was used in phase averaging the measurement data. Further information about the settings used in QBlade for the simulations conducted in this study can be found in Klein et al. (2017).

3.4 Test Conditions

3.4.1 ACP Spring Settings

The ACP mechanism was controlled in its actuation properties by a torsional spring. The spring steel used (EN 1.1248) had a modulus of elasticity $E = 81500\,N/mm^2$. During the experiments, the spring stiffness had a value $k = 5.3\,Nmm/°$, calculated according to (Grothe & Feldhusen, 2007, G52) with a torsion beam of 3 mm height, 0.5 mm width and 30 mm length. However, at the ACP section-2 of Blade-3 the spring stiffness was $k = 6.38\,Nmm/°$ because of its shorter length of 25 mm.

In single-section operation, two different pre-tensions have been investigated, 32 Nmm and 43.8 Nmm. The spring pre-tension is always selected so that the mean profile camber resulting from the dynamic ACP movement corresponds to the camber of the profile in its original rigid configuration. A higher or lower pre-tension increases or decreases the mean camber of the ACP in the dynamic case, starting from this reference value and it influences the amplitude of the ACP movement at a given operating point of the turbine. The initial angle of the trailing edge flap γ_i has been set to 5° and was adjusted by the mechanical stopper of the ACP mechanism. A trailing edge flap angle γ of 0° represents the Clark-Y profile in its rigid condition. If there is a negative trailing edge flap angle the ACP is de-cambered relative to the rigid Clark-Y condition. Data have been collected for rotor plane yaw angles of 0°and -30°. The results comprise data for the trailing edge flap angle and the strain gauge readings from the blade root, which document any alleviation of load fluctuations.

In multi-section operation two different pre-tension settings were investigated, but the magnitude of the pre-tensions for each flap section was different. In table 3.3 the two sets of investigated pre-tensions and the initial trailing flap angles γ are listed. The spring stiffness at ACP section-1 and 3 is 5.3 $Nmm/°$. The spring stiffness at ACP section-2 is 6.4 $Nmm/°$. The

length of spring 2 is limited to 25 mm , because of limited available cross section for the mechanics at Blade-3 in that area.

Blade-3	Setting-1 (Nmm)	Setting-2 (Nmm)	γ_i (°)
Flap-1	44.5	87.6	2
Flap-2	53.8	90.34	5.8
Flap-3	44.5	62.5	12.7

Table 3.3: Investigated pre-tension settings and initial trailing edge angles γ_i of Blade-3 during multi-section operation.

Blade-2 (one ACP section) was preliminary tested in the large low speed wind tunnel of the TU Darmstadt. It was possible to adjust the initial trailing flap angle γ_i and the pre-tension relatively precisely in the desired manner for single-section investigations. The characteristics of Blade-3 were approximately adjusted by examining the incoming data during the experiments, which was the only possible option under the extenuating circumstances of the experimental campaign in Berlin. The difference between single-section and multi-section investigations regarding the pre-tension setting is that the jump between the two adjustments is rather large, which has to be kept in mind when discussing the impact of pre-tension in the specific cases.

Another difference between single-section and multi-section investigations are the operation points. The operation point at a rotor speed of 2.0 Hz is not investigated in multi-section operation. Single-section operation had the goal to simply observe a reaction of the ACP mechanism within a rotational system of a wind turbine for the first time. However, the tunnel speed could only be varied from 6.5 m/s to 8.5 m/s, and even at 8.5 m/s the ACP just became active. The other parameter that could be varied for adjusting the gust amplitude was the rotor frequency, which also has an effect on the blade incident velocity. With these operation parameters it becomes evident that even at ACP section-3 the blade incident velocity decreases to about 12 m/s, which is a critical lower limit for the ACP operation.

The single-section operation investigation starts at 2.0 Hz, because for section-3 it is the lower bound for blade incident velocity and achieves the maximum gust amplitude. For further investigations with multi-section operation a rotor frequency of 2.0 Hz is not viable, because most of the blade is in a stalled condition. Therefore, an additional operation point at 3.5 Hz rotor frequency has been included for multi-section investigations, where section-1 and section-2 operate at more interesting blade incident velocity conditions.

3.4.2 Test Matrix

Table 3.4 summarises the test cases performed in the measurement campaign. At the listed operation points single-section as well as multi-section operation were selectively investigated and compared to the rigid reference case.

Rotor Plane Yaw [°]	Wind [m/s]	Rotational Frequency [Hz]	Tip Speed Ratio
0	8.5	2.5	2.8
0	8.5	3.0	3.3
0	8.5	3.5	3.9
-30	8.5	2.0	2.2
-30	8.5	2.5	2.8
-30	8.5	3.0	3.3
-30	8.5	3.5	3.9

Table 3.4: Test matrix.

3.5 Data Evaluation and Interpretation

Data evaluation is based on azimuthal phase averaging of all measured quantities. The duration of one measurement run is approximately 20 s, corresponding to approximately 40 to 60 rotations of the rotor. The trigger signal for the phase averaging is extracted from the rotor azimuthal angle signal. The data are binned into intervals of 5° azimuthal angle θ. The data of all

specific intervals sampled during a run are averaged and are considered representative of values at a rotation angle at the centre of every interval. This results in a maximum angular resolution of 5° for any quantity.

The choice of bin width, here 5°, represents a compromise between angular resolution and measurement accuracy. If the bin width is chosen too small, then the number of measurements contributing to the phase averaged value is low and the variability of the mean estimator increases. If the bin width is chosen too large, angular resolution decreases, but also systematic errors increase. This is briefly elaborated using a representative measured quantity x. The quantity x can be expressed using a triple decomposition as

$$x(t) = \overline{x} + \tilde{x}(\theta(t)) + x'(t) \tag{3.2}$$

where $\overline{x}$ represents the time mean average, $\tilde{x}$ is the phase dependent part (with θ denoting the phase angle) and $x'(t)$ corresponds to the stochastic part of x. The phase averaging performed in the present study for different measurement quantities represents an estimation of the $\tilde{x}(\theta(t))$ part. However, the stochastic part $x'(t)$ is estimated in the present study as the standard deviation of all values occurring in a given phase interval, using $\tilde{x}(\theta(t))$ as the mean value in the respective angular bin. However, if the phase dependent part varies significantly with angle, then the standard deviation computed over the angular interval will include this variation, which can be viewed as a systematic error of the standard deviation estimator. Nevertheless, no attempt has been made to refine this estimator, since the standard deviation, i.e. the $x'(t)$ part of the triple decomposition, will not be used for further analysis or interpretation. This concept will now be illustrated using several example measurement quantities.

Figure 3.15 shows the phase dependent AoA taken from probe 2 with a yawed rotor plane of $\phi = -30°$ and at an angular rotor frequency of $3\,Hz$. The vertical bars for each angular bin represent ± 2 bin standard deviations. This data indicates that the scatter within one bin is within about $\pm 1°$(95% confidence), which is significantly more than the calibrated uncertainty of the

probe ($\pm 0.2°$). This scatter is considered to be satisfactory, since the main variations of AoA with azimuthal angle can still be easily identified.

In the following presentations of the measured incident blade velocity for a rotor frequency of 2.5 Hz, data within an azimuthal angle range of 162.5° to 217.5° is unhinged, because the five-hole probe reached their limits for velocities lower than 10 m/s. (Regard figures, 4.6, 4.8, 4.9, 4.30)

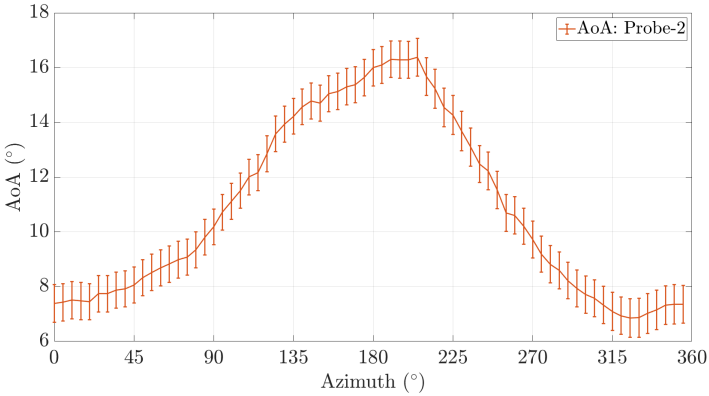

Figure 3.15: Phase averaged data of the measured AOA at a rotor frequency of 3.0 Hz and a rotor plane yaw angle $\phi = -30°$. The vertical bars represent twice the angular bin standard deviation.

Figure 3.16 depicts the phase averaged data of the trailing edge flap angle, γ, measured at a rotor frequency of 2.5 Hz. The black curve shows a run which is exemplary for a reference measurement of a rigid blade. The blue curve represents a typical result obtained when the adaptive camber mechanism is in operation.

The results obtained for the rigid blade confirm for one, that the flap is not moving significantly and second, that the estimated $\pm$ 0.09° uncertainty is a good estimate of the stochastic error (67% confidence). The results for the activated ACP indicate a higher angular bin standard deviation, which

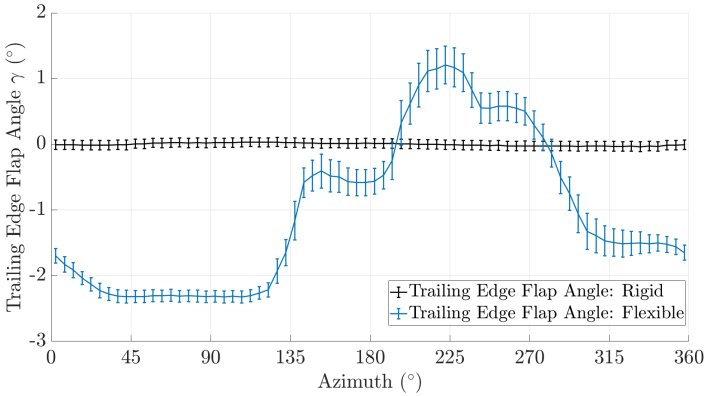

Figure 3.16: Phase averaged data of the measured trailing edge flap angle γ at a rotor frequency of 2.5 Hz and rotor plane yaw angle $\phi = -30°$. The vertical bars represent the angular bin standard deviation. The black curve is for a blade with a rigid profile, the blue curve for a blade with activated adaptive camber mechanism.

arises from the phase dependent part of the trailing edge flap angle variations.

Finally, figure 3.17 shows the OPRB factor at a rotor frequency of 3.0 Hz and a rotor plane yaw angle of $\phi = -30°$. The black curve depicts a reference run with a rigid profile, while the red curve represents the behaviour of the rotor blade with the ACP mechanism in operation. In this figure the vertical bars represent twice the angular bin standard deviation. These results illustrate two interesting observations. For one, the bending moment is strongly influenced by the adaptive camber profile, which will be discussed in detail in Chapter 4. Second, the angular bin standard deviation is very similar for both conditions, which is to be expected, since for both the rigid and ACP profiles, significant bending moment fluctuations as a function of azimuthal angle are to be expected for a yawed rotor plane.

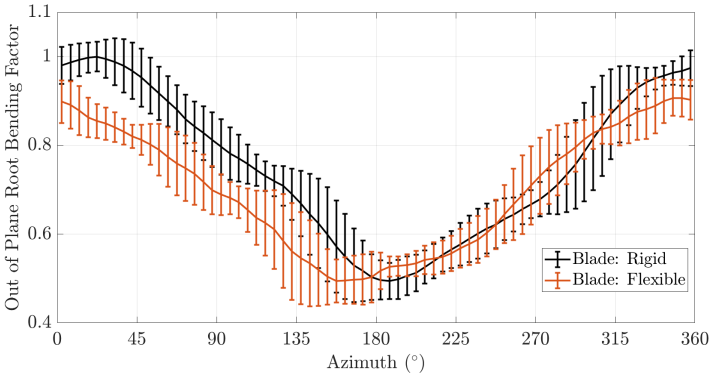

Figure 3.17: Phase averaged data of the measured out-of-plane root bending moment at a rotor frequency of 3.0 Hz and a rotor plane yaw angle $\phi = -30°$. The vertical bars represent twice the angular bin standard deviation. The black curve is for a rigid profile, the red curve for a blade with activated adaptive camber mechanism.

4 Results and Discussion

4.1 Incident Flow on Blades

In this first subsection the blade incident flow is documented, as measured using the five-hole pressure probes. Although three such probes were mounted at different blade spans, only one probe functioned properly during the test campaign and this probe was positioned at 50% of the blade radius. The general plausibility and reliability of the data is discussed in sections 3.2.1 and 3.5.

Figure 4.1 shows the measured phase averaged data of the AoA(α) over the azimuthal angle θ for a rotor plane yaw angle $\phi = 0°$. Data sampled at rotor frequencies of 2.5 Hz, 3.0 Hz and 3.5 Hz are shown. As expected, the mean AoA increases with a decreasing rotor frequency. For a rotor plane yaw angle $\phi = 0°$, a significant change in the AoA curve can only be expected when the blade passes the tower shadow at the azimuthal angle of 180°. The expected distortion can be observed at a rotor frequency of 3.0 Hz and 3.5 Hz. At the rotor frequency of 2.5 Hz, where a separated flow regime is present at the specific span position, a tower impact on the AoA curve cannot be observed.

Figure 4.2 shows the measured phase averaged data of the side-slip angle β over the azimuthal angle θ at a rotor plane yaw angle $\phi = 0°$. Data sampled at rotor frequencies of 2.5 Hz, 3.0 Hz and 3.5 Hz are shown. The side-slip angle is not constant over one rotation because of the non-uniform inflow velocity in the wind tunnel settling chamber (see section 3.1.1 and reference Klein et al. (2017)). The data gathered at rotor frequencies of 2.5 Hz and 3.0 Hz are at relatively the same level, while the data measured at a rotor frequency of 3.5 Hz differs significantly. At a rotor frequency of 3.5 Hz attached flow over the entire rotation can be assumed at this specific span position.

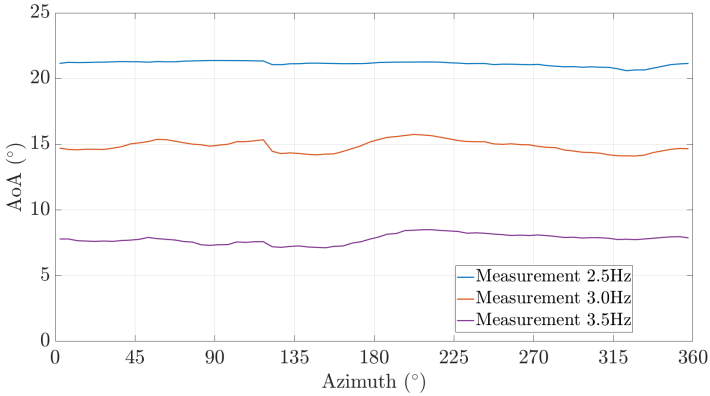

Figure 4.1: Measured phase averaged angle of attack α data over the azimuthal angle θ for a rotor plane yaw angle $\phi = 0°$. Data sampled at rotor frequencies of 2.5 Hz, 3.0 Hz and 3.5 Hz are shown.

Notable in Figs. 4.1 and 4.2 are significant jumps in the values of both AoA and slide-slip angle β at a rotation angle of approximately 120°. These jumps of 1-2°are much larger than the measurement uncertainty of the five-hole probe, as elaborated in Fig. 3.12. On the other hand, this is unlikely a physical flow phenomenon, since there is no plausible explanation for a significant angular change of flow velocity at this rotor position. The conjecture is that this jump arises from unsteady mechanical rotation of the turbine, since for these measurements, the drive belt of the turbine was already damaged. Unfortunately, a definitive conclusion about this effect cannot be retroactively drawn.

Figure 4.3 shows the measured phase averaged data of the total velocity v_T measured by the five-hole pressure probe located at 50% of the blade span for a rotor plane yaw angle $\phi = 0°$. The data is gathered for rotor frequencies of 2.5 Hz, 3.0 Hz and 3.5 Hz. As can be expected, the total velocity v_T increases with increasing rotor frequency.

For comparison, the same quantities as presented above are now shown for

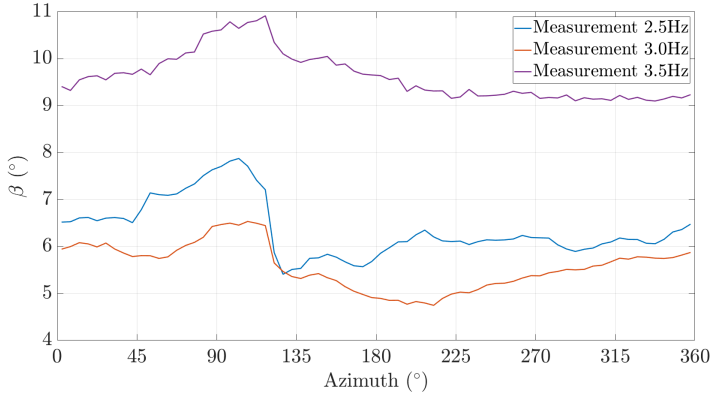

Figure 4.2: Measured phase averaged data of the side-slip angle β of the blade section at 50 % of the blade radius at a rotor plane yaw angle $\phi = 0°$ over the azimuthal angle θ

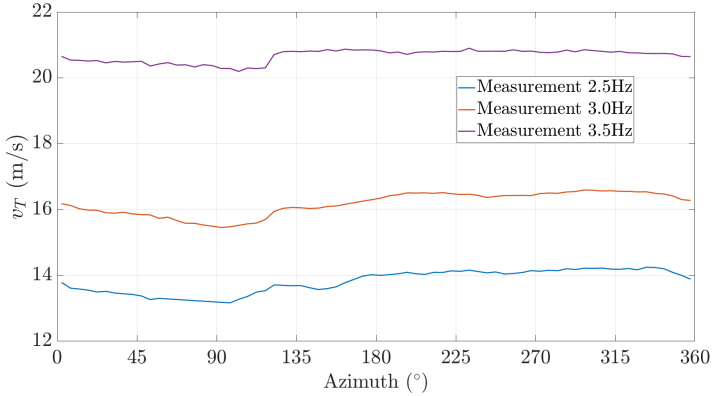

Figure 4.3: Measured phase averaged total velocity v_T at 50% of the blade span for a rotor plane yaw angle $\phi = 0°$. Data sampled at rotor frequencies of 2.5 Hz, 3.0 Hz and 3.5 Hz are shown.

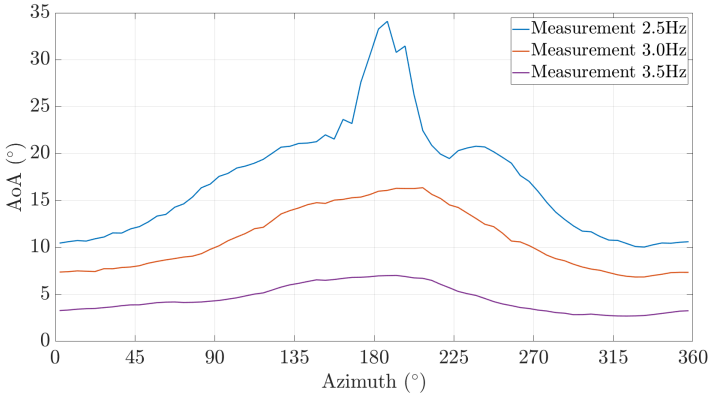

Figure 4.4: Measured phase averaged AoA(α) over the azimuthal angle (θ) for a rotor plane yaw angle $\phi = -30°$. Data sampled at rotor frequencies of 2.5 Hz, 3.0 Hz and 3.5 Hz are shown.

a rotor plane yaw angle $\phi = -30°$. Figure 4.4 shows the AoA(α) curves at the three rotor frequencies. The AoA fluctuations due to the rotor plane yaw is evident. The amplitude of the fluctuations increases with a decreasing rotor frequency, because the component of the constant rotational speed, Ω, becomes less dominant.

The measured phase averaged data of the side-slip angle (β) for a rotor plane yaw angle $\phi = -30°$ is presented in figure 4.5. The fluctuation of β due to the rotor plane yaw angle is clearly visible. As observed for a rotor plane yaw angle $\phi = 0°$, the data measured at rotor frequencies of 2.5 Hz and 3.0 Hz are relatively at the same level, while the mean of the β curve derived from data measured at a rotor frequency of 3.5 Hz lies at a higher mean β angle. It can be observed that β reaches its minimum when the AoA reaches its maximum at an azimuthal angle $\theta = 180°$.

Figure 4.6 depicts the measured phase averaged data of the total velocity v_T at a rotor plane yaw angle $\phi = -30°$. It can be observed, that the az-

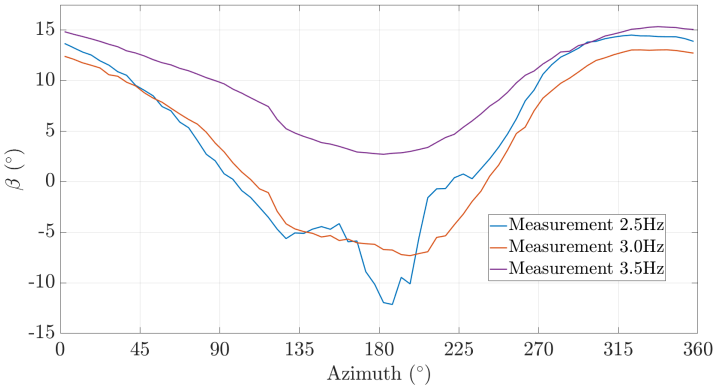

Figure 4.5: Measured phase averaged data of the side-slip angle β of the blade section at 50% of the blade span for a rotor plane yaw angle $\phi = -30°$ over the azimuthal angle θ. Data at rotor frequencies of 2.5 Hz, 3.0 Hz and 3.5 Hz are shown.

imuthal position of the maximum and minimum of v_T depends on the rotor frequency.

Table 4.1 summarises the mean values derived from the above presented data of the blade incident flow at 50% of the blade span. In general all mean values decrease due to a yawed rotor plane. The yaw angle causes a relatively small decrease of the total velocity v_T. The most significant impact of the yaw case scenario can be observed in the AoA(α) data. The mean of the side-slip angle β seems to be more sensitive to the rotor frequency. Looking at the values at a rotor frequency of 3.5 Hz it can be observed that there is practically no difference of $\overline{v_T}$ and $\overline{\beta}$ between a rotor plane yaw angle of $\phi = 0°$ compared to $\phi = -30°$.

Figure 4.7 elaborates on figure 2.6 introduced in section 2.2.2. It shows a blade profile for a given span position, with a local profile twist angle τ between the yawed rotor plane and the chord of the profile. If there is a blade twist angle τ, the component of the total blade incident velocity (v_T) parallel

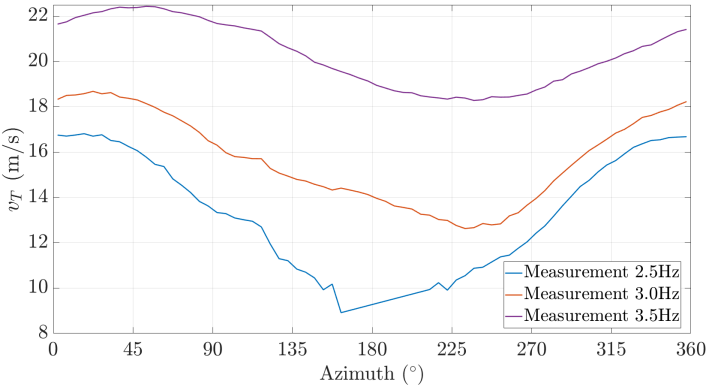

Figure 4.6: Measured phase averaged total velocity v_T data at 50% of the blade span for a rotor plane yaw angle $\phi = -30°$. Data sampled at rotor frequencies of 2.5 Hz, 3.0 Hz and 3.5 Hz are shown.

$\bar{\alpha}(°)$	$\phi = 0°$	$\phi = -30°$
$f = 2.5Hz$	21.14	17.18
$f = 3.0Hz$	14.85	10.86
$f = 3.5Hz$	7.8	4.53

$\bar{\beta}(°)$	$\phi = 0°$	$\phi = -30°$
$f = 2.5Hz$	6.36	4.34
$f = 3.0Hz$	5.58	3.8
$f = 3.5Hz$	9.63	9.52

$\bar{v_T}(m/s)$	$\phi = 0°$	$\phi = -30°$
$f = 2.5Hz$	13.8	13.44
$f = 3.0Hz$	16.17	15.53
$f = 3.5Hz$	20.67	20.25

Table 4.1: Mean values of measured α, β and v_T data at rotor frequencies of 2.5 Hz, 3.0 Hz and 3.5 Hz. Mean values derived from data sampled at rotor plane yaw angle $\phi = 0°$ are compared to mean values derived from data sampled at $\phi = -30°$.

to the chord c is not simply the local angular velocity Ωr, as described in section 2.2.2, but becomes dependent on v_2. The component of v_T parallel to the chord is denoted by v_{Ty}.

Figure 4.7 depicts the revolution in terms of a plunging motion seen by the blade profile. The total travel during the effective upstroke and downstroke motion is defined as x_{plunge}. It depends on the rotor plane yaw angle ϕ and the radial span position r. The downstroke included in the rotor plane yaw case takes place over an azimuthal angle range between 270° to 90°, while the upstroke occurs over an azimuthal angle range between 90° and 270°. That means the upper and lower turning points of the plunging motion are located at azimuthal positions of 270° and 90°. At these points the velocity component v_{plunge} induced by the plunging motion disappears. Furthermore, the side-slip velocity v_{Tr}; hence, the curves of the side-slip angle β induced by v_{Tr} reach their inflection points. The velocity component v_{plunge} is added to v_2 during the "downstroke" and subtracted during the "upstroke".

The two-dimensional total blade incident velocity seen by a specific blade profile is defined as

$$v_{T2d} = \sqrt{{v_{Tx}}^2 + {v_{Ty}}^2} \tag{4.1}$$

The three components of the total blade incident velocity (v_T), v_{Tx}, v_{Ty} and v_{Tr}, according to Treaster & Yocum (1978) are given by

$$v_{Tx} = v_T \sin\alpha(\phi, \tau) \cos\beta(\phi) \tag{4.2}$$

$$v_{Ty} = v_T \cos\alpha(\phi, \tau) \cos\beta(\phi) \tag{4.3}$$

$$v_{Tr} = v_T \sin\beta(\phi) \tag{4.4}$$

Figure 4.8 shows the v_{Tx} trends over the azimuthal angle θ. With an increase of the rotor frequency the mean of v_{Tx} decreases due to an increase of Ω; hence a decrease of α. It can be assumed that v_{plunge} has the largest impact on v_{Tx}. Furthermore, the impact of v_{plunge} should increase with with increasing rotor frequency. At an azimuthal angle $\theta = 90°$ and 270°, v_{plunge} should become zero and that should also be observable in the trends of v_{Tx}.

Looking at the trends in figure 4.8 a pre-maximum about an azimuthal angle $\theta = 90°$ can be observed. That hump becomes more distinctive and and shifts closer to an azimuthal angle of 90° with increasing rotor frequency. Beyond an azimuthal angle of 90°, v_{plunge} is expected to change direction and counteract the constant velocity v_2, which is also a main component of v_{Tx}. At an azimuthal angle of 270° at the end of the "downstroke", v_{plunge} is expected to become zero and change its direction again with a specific delay. Looking at the trends in Figure 4.8 a pre-minimum about an azimuthal angle $\theta = 270°$ can be observed. The second hump becomes more distinctive and and shifts closer to an azimuthal angle of 270° with increasing rotor frequency.

At this point it is instructive to underline that the plunging motion corresponds directly to the Theodorsen situation, arising from the yawed rotor plane. Especially at a rotor frequency of 3.5 Hz, where Theodorsen conditions are best fulfilled, the expected behaviour becomes evident.

Another fluctuating velocity component which impacts v_2 and also arising from the yawed rotor plane is v_{Tr}. It can be assumed, that if v_{Tr} decreases, a percentage of this decrease is added to v_{Tx} and if v_{Tr} increases, a percentage of this increase is subtracted from v_{Tx}.

Figure 4.9 shows the v_{Tr} trends over the azimuthal angle ϕ. The presented trends of v_{Tr} confirm the assumptions about its influence on v_{Tx}. The v_{Tr} curves show a further decrease beyond an azimuthal angle $\theta = 90°$, which causes a further increase of v_{Tx} beyond the discussed pre-maxima to the main maxima of the trends shown in figure 4.8. The same applies for the minima of

the v_{Tx} trends. A further increase of v_{Tr} beyond an azimuthal angle of 270° causes a further decrease of v_{Tx}.

Unfortunately no incident flow data at 30% and 70% of the blade span could be collected during the measurement campaign. For the later discussion of ACP behaviour, QBlade simulations at the specific operation points and span positions are used as a reference. Figures 4.10 and 4.11 show the blade incident velocity at 30% blade radius obtained using QBlade. This corresponds to the radial position of ACP section-1. Figures 4.12 and 4.13 show the blade incident velocity at 70% blade radius, which represents the radial position of ACP section-3.

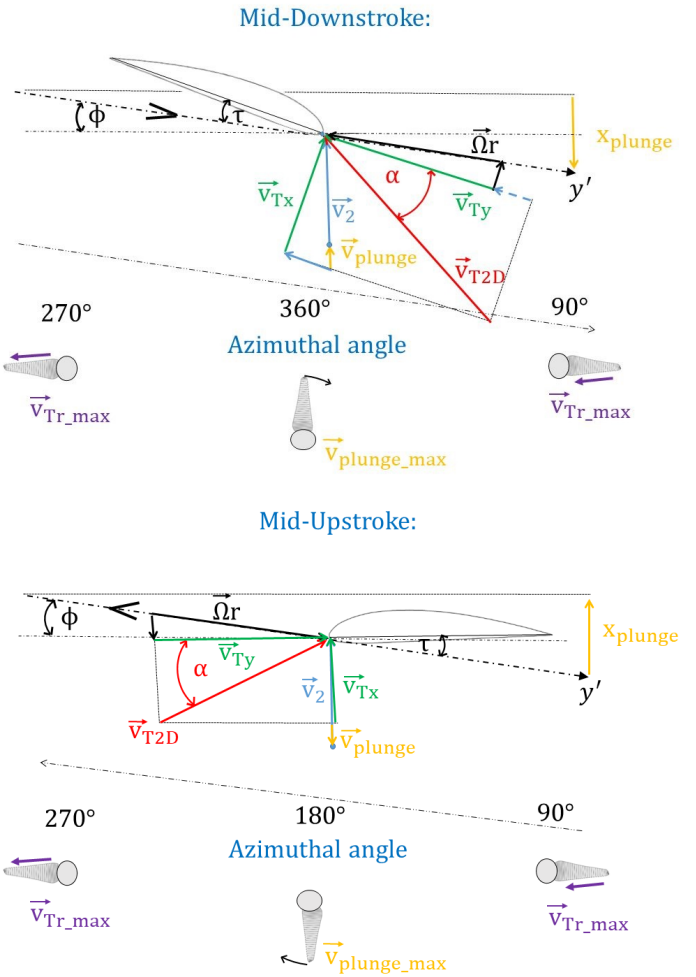

Figure 4.7: Velocity triangles of a blade profile section at different positions of the azimuthal angle θ at for a rotor plane yaw angle ϕ. The profile section has a twist angle τ. The two-dimensional presentation is based on the concept of an induced plunge velocity v_{plunge} due to the yawed rotor plane.

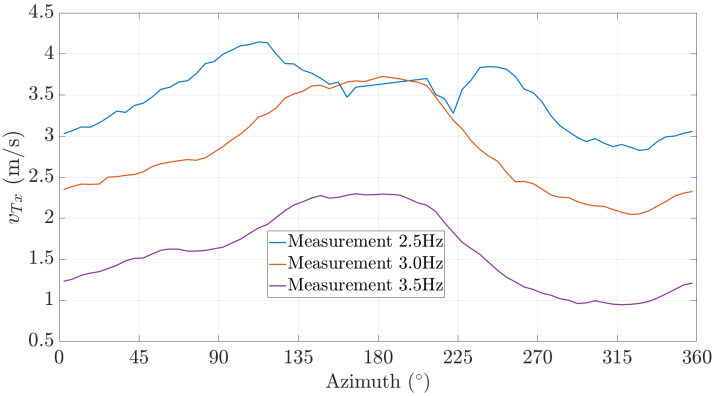

Figure 4.8: Data of the velocity component v_{Tx} of v_T over the azimuthal angle θ. The curves represent data measured at rotor frequencies of 2.5 Hz, 3.0 Hz and 3.5 Hz for a rotor plane yaw angle $\phi = -30°$.

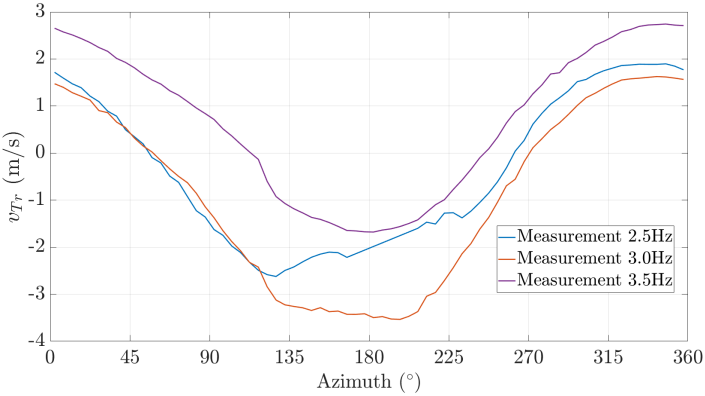

Figure 4.9: The curves depict the velocity component v_{Tr} of v_T over the azimuthal angle θ. The curves represent data measured at rotor frequencies of 2.5 Hz, 3.0 Hz and 3.5 Hz for a rotor plane yaw angle $\phi = -30°$.

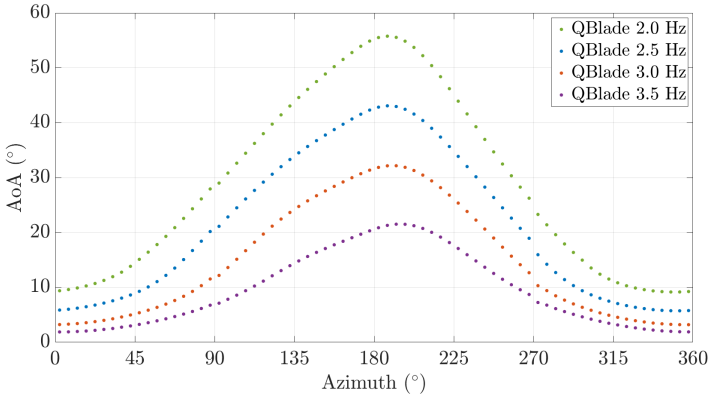

Figure 4.10: QBlade predictions of the AoA at 30% of the blade span over the azimuthal angle θ for a rotor plane yaw angle $\phi = -30°$.

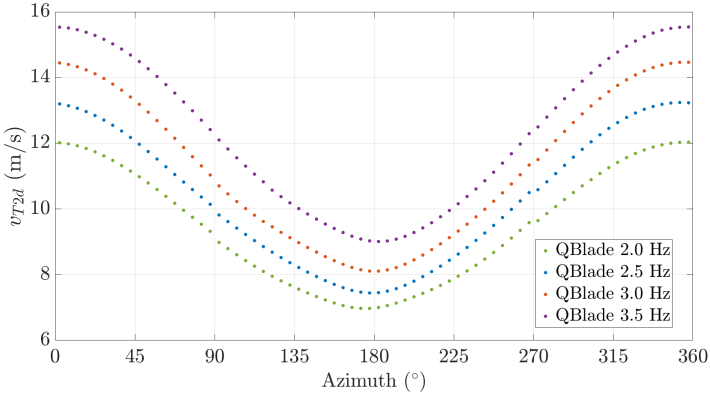

Figure 4.11: QBlade predictions of the total velocity v_{T2d} at 30% of the blade span over the azimuthal angle θ for a rotor plane yaw angle $\phi = -30°$.

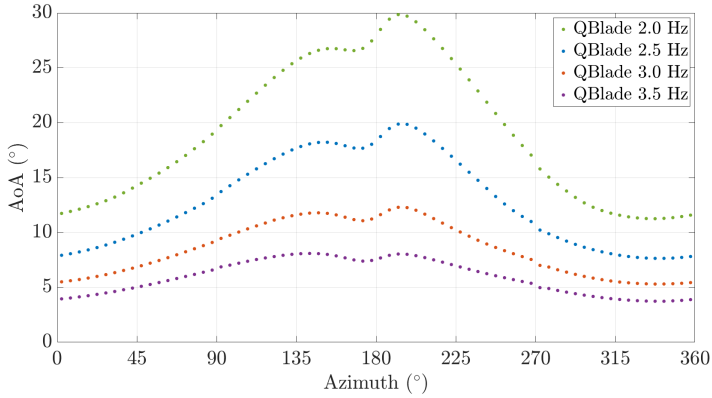

Figure 4.12: QBlade predictions of the AoA at 70% of the blade span over the azimuthal angle θ for a rotor plane yaw angle $\phi = -30°$.

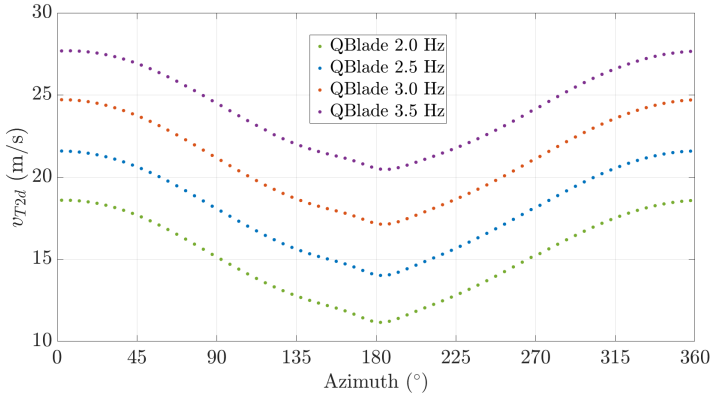

Figure 4.13: QBlade predictions of the total velocity v_{T2d} at 70% of the blade span over the azimuthal angle θ for a rotor plane yaw angle $\phi = -30°$.

4.2 Results of Single-Section ACP Operation

In the following subsection the response of the single ACP section mounted on Blade-2 between 60% and 80% of the blade span is examined.

Figure 4.14 shows the trailing edge flap angle for a rotor plane yaw of $\phi = -30°$ over the azimuthal angle for three different rotor speeds and for two pre-tensions. It can be observed that the mean camber of the ACP profile decreases with increasing rotor frequency. Furthermore, the amplitude of the trailing edge flap deflection decreases with increasing rotor frequency. Both observations reflect the general behaviour of the incident blade velocity on the profile section, as discussed in section 4.1.

Before further interpreting these curves, it is instructive to recall the AoA values at 70% span for the three rotor angular frequencies. These values were not directly measured; however, approximate values have been estimated using QBlade and presented in figure 4.12. At a rotor frequency of 2.0 Hz and a blade span position of 70% (ACP section-3) the AoA ranges between about 12° and 30°, reaching conditions of dynamic and total stall. At a rotor frequency of 2.5 Hz the AoA ranges between about 8° and 20°, covering both the linear and the dynamic stall region of the lift curve. At a rotor frequency of 3.0 Hz the AoA ranges between about 5° and 12°, lying only in the linear region of the lift curve.

Comparing the three curves presented in figure 4.14 measured at various rotor frequencies, it can be observed that they differ significantly. At a rotor frequency of 2.0 Hz for example, there in the range of azimuthal angle $180° < \theta < 270°$ within which the trailing edge flap angle γ remains constant near the initial pre-camber value. Looking at the values of the blade incident flow in figures 4.12 and 4.13 it becomes clear that in this range of azimuthal angle the AoA increases beyond the critical total stall angle of 20°. Furthermore, the blade incident velocity lies below 15 m/s, which means that the Reynolds number falls below 200,000 into a range which is not recommended

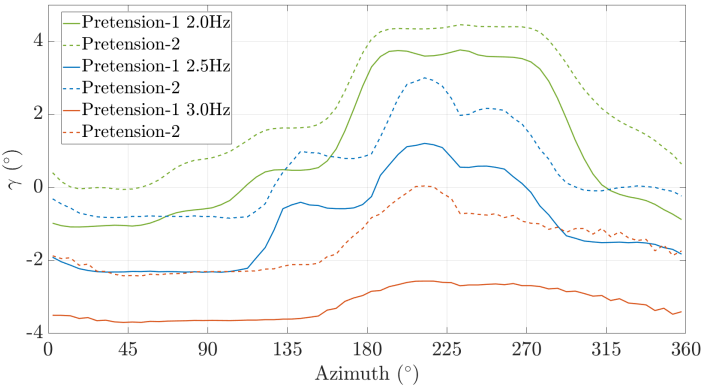

Figure 4.14: Measured phase averaged data of trailing edge flap angle γ for a rotor plane yaw angle ϕ = -30° over the azimuthal angle θ. Results are shown for two different pre-tensions and three different rotor speeds. ACP segment at 60% to 80% span.

for operation of the Clark-Y profile. Under these conditions the ACP returns to its default state and does not actively influence the flow.

The trailing edge flap movement at a rotor frequency of 2.5 Hz over the same range of azimuthal angle exhibits a more pronounced contour, reflecting the influence of the tower shadow on the ACP response. This coincides closely with the AoA changes predicted by QBlade, as shown in figure 4.12. The tower shadow leads to a short AoA dip, which leads to an increase in camber of the ACP.

At larger values of azimuthal angle, beyond about $\theta = 230° - 250°$, the trailing edge flap angle decreases smoothly in figure 4.14 for the higher rotor frequencies, whereby the slope of the decrease also decreases with increasing rotor frequency. This is very consistent with the expected trends of AoA in this azimuthal angle range, as depicted in figure 4.12 . This close correlation between AoA and trailing edge flap angle indicates that the ACP is operating in the linear range of the lift curve in this range of azimuthal angle.

There is another conspicuous feature observed in the trailing edge flap angle curves which arises at rotor frequencies of 2.0 Hz and 2.5 Hz at the azimuthal angles of approximately $\theta = 150°$ and 300°. At these points, a flattening of the curves seems to be initiated with a certain angle beyond top or bottom dead center of the plunge motion, which cannot be directly correlated with the corresponding AoA trends. This directly influences the velocity component v_{Tx} and, as concluded in Spiegelberg (2014) and Cordes (2016), the ACP movement is very sensitive to this component of velocity; hence to the effective plunging motion. The flattening in these curves can therefore be attributed to this kinematic influence. At the higher rotor frequency the influence of the plunging motion becomes less, since the rotation frequency dominates the total velocity vector, especially at the 60%-80% rotor span position depicted in figure 4.14.

At a rotor frequency of 3.0 Hz the corresponding AoA curve in figure 4.12 remains within a moderate range under an AoA of 10°, where attached flow over the complete rotation at ACP section-3 can be assumed. Compared to other operation points, the gust amplitude with respect to AoA and velocity is relatively small. Due to that fact the reaction of the ACP is weaker. The curve is smoother, round and not as defined as at other rotor frequencies.

Regarding the present investigation of two different pre-tensions, it can be observed, that a higher pre-tension shifts the curves of the trailing edge flap angle to a state of lower mean deflection, as can be expected. Furthermore, the amplitude of flap deflection is not strongly affected by the change of pre-tension. In particular, if the mean deflection does not change much, the amplitude of flap deflection mainly depends on the spring stiffness. To provoke larger flap deflections, a lower spring stiffness could be chosen.

In a nutshell, figure 4.14 represents a milestone, because for the first time it documents the operation of a rotor blade with a passively deforming camber profile in the rotational system of a wind turbine. Operation points and

a gust scenario has been experimentally implemented, which supply various flow regime conditions over the blade span and mimic real and relevant gust scenarios. It can be pointed out that the implementation of the unique ACP design reacts extremely fast and precise to the incoming flow.

Figure 4.15 shows the phase averaged data of the out-of-plane root bending factor (OPRB) measured at a rotor frequency of 2.0 Hz for a rotor plane yaw angle $\phi = -30°$. The bending of the rigid blade is compared with Blade-2 containing the single-section ACP. Results for two pre-tensions are presented. One should assume that all OPRB curves for the rigid profile are always identical for given measurement conditions, however this is not strictly the case for two reasons. First, OPRB curves are acquired for both the single-section ACP blade and the multi-section ACP blade, thus the blades are not in themselves structurally identical. Furthermore, the strain gauges are different on each blade and uncalibrated. For this reason, no attempt is made to directly compare OPRB curves between the two blades in interpreting measurement results.

It can be observed, that there is no influence of ACP operation regarding the behaviour of root loads over a large azimuthal angle range from about 90° to about 270°. Neither can an influence of the pre-tension adjustment be observed. Only in the remaining azimuthal range around 0° is a slight peak load reduction observed. It can be assumed that the ACP does not make a difference under totally stalled conditions, considering that there is only a small mean camber compared to the rigid blade. Only in the above-mentioned range around a azimuthal angle of 0° does the AoA fall below the 20° limit for stalled conditions.

Figure 4.16 shows the phase averaged data of the Out-of-Plane Root Bending factor (OPRB) measured at a rotor frequency of 2.5 Hz. The corresponding AoA trend does not exceed the 20° limit. In an azimuthal angle range from about 270° to about 45° the AoA falls slightly below 10°, where attached flow can be assumed. The ACP profile is therefore mostly acting under fully stalled conditions, as described in section 2.2.1. In an azimuthal angle range

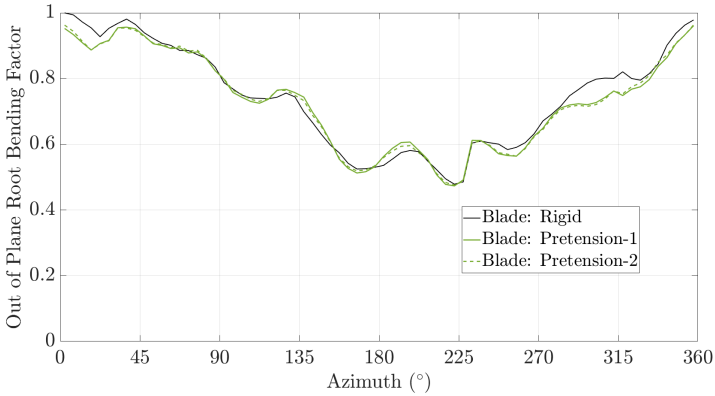

Figure 4.15: Comparison of measured phase averaged dimensionless out-of-plane root bending data at a rotor frequency of 2.0 Hz. Data for the blade is compared to data of Blade-2 in which single-section ACP is installed. Results for two pretensions and a rotor plane yaw angle $\phi - 30°$ are shown.

of about 135° to 270°, and according to figure 4.14, the largest ACP activity has been observed; here the dynamic stall cycle is expected to take place.

A peak load reduction of about 5% compared to the rigid blade can be observed, while the load minimum does not fall below the minimum of the rigid blade. This indicates a reduction of periodically alternating loads by the ACP. Furthermore, an influence of the spring stiffness in the described azimuthal angle range of about 135° to 270° becomes obvious. In the remaining azimuthal angle range with low ACP activity and assumed attached flow, an influence of the pre-tension still cannot observed.

Figure 4.17 shows the phase averaged data of the Out-of-Plane Root Bending factor (OPRB) measured at a rotor frequency of 3.0 Hz. The tip speed ratio for that rotor frequency is 3.3. The AoA fluctuations due to the yawed rotor plane are about 5° to 12°. That range includes design AoAs of a typical turbine. This case represents realistic root load fluctuations under normal operation conditions of common turbines.

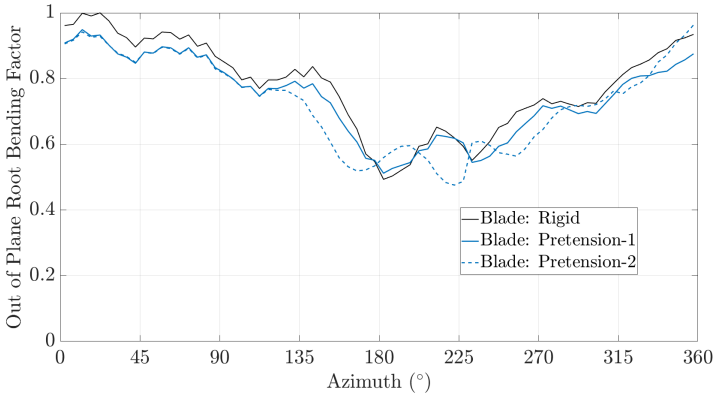

Figure 4.16: Comparison of measured phase averaged dimensionless out-of-plane root bending data at a rotor frequency of 2.5 Hz. Data of the rigid blade is compared with ACP data of Blade-2 at two pre-tensions and for a rotor plane yaw angle $\phi = -30°$.

Qualitatively the trends in figure 4.17 do not differ much from the trends in figure 4.16. Compared to the data gathered at a rotor frequency of 2.5 Hz, a higher peak load reduction of about 10% could be achieved. The observation indicates the high potential of the ACP to reduce periodic alternating loads of wind turbine blades under realistic conditions.

It is apparent in both Figs. 4.16 and 4.24 that the curves for OPRB at pre-tension 2 exhibit significant fluctuations in the rotor angular range 90°270°, deviating from the smoother curves for pre-tension 1. This behaviour is also addressed in section 4.3; however, especially for 3.0 Hz it appears that the ACP flap movement becomes unstable and exhibits an oscillating behaviour. Further discussion of this effect is found in section 4.3.

To summarise this subsection, it can be pointed out that the functionality of the ACP in a rotating frame of reference as been documented experimentally for the first time. Moreover, the ACP concept operates in the desired manner and is able to reduce periodically unsteady loads at the blade root.

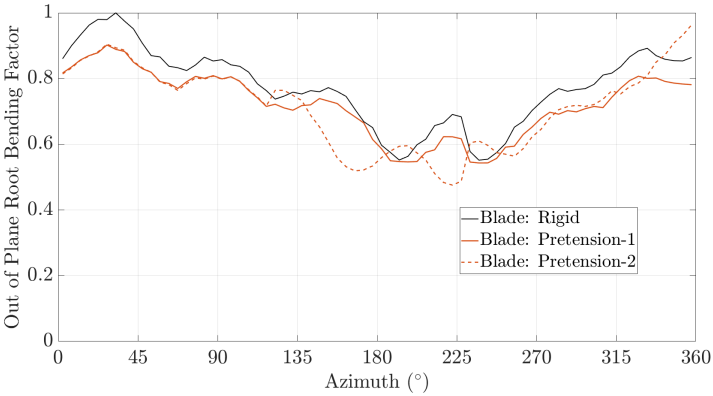

Figure 4.17: Comparison of measured phase averaged dimensionless out-of-plane root bending data at a rotor frequency of 3.0 Hz. Data of the rigid blade is compared with ACP data of Blade-2 at two pre-tensions and for a rotor plane yaw angle $\phi = -30°$.

The central design criterion, namely to achieve an effect on aerodynamic loads by small structural deformations, has been achieved. An experimental verification of about 10% peak load reduction can be considered very successful. The reduction is achieved by trailing edge flap angle amplitudes smaller than 3.5°.

4.3 Results of Multi-Section ACP Operation

In the following section the response of Blade-3 with three installed ACP sections is examined. Table 4.2 lists the mean values and standard deviations of the trailing edge flap angle movement measured at the three rotor frequencies for the two pre-tension settings described in subsection 3.4.1. The mean flap deflection is subtracted from the data presented in the following figures for better comparability of the movement of the three different ACP sections among each other.

The values presented in table 4.2 show qualitatively the same trends as

Pre-tension setting-1	γ_1 (°)	γ_2 (°)	γ_3 (°)
mean at 2.5 Hz	0.8	-0.3	-3.5
STD at 2.5 Hz	0.55	0.49	1.1
mean at 3.0 Hz	0.5	-0.31	-5.2
STD at 3.0 Hz	0.6	0.3	0.3
mean at 3.5 Hz	0.12	-0.6	-6.3
STD at 3.5 Hz	0.5	0.1	0.08
Pre-tension setting-2	γ_1 (°)	γ_2 (°)	γ_3 (°)
mean at 2.5 Hz	1.4	2.1	2.8
STD at 2.5 Hz	0.13	0.52	0.71
mean at 3.0 Hz	1.24	2.0	1.3
STD at 3.0 Hz	0.16	0.35	0.13

Table 4.2: Comparison of the mean values and standard deviations of measured phase averaged data of the trailing edge flap angle γ for ACP segments 1, 2 and 3 for a rotor plane yaw angle $\phi = -30°$.

observed for single-section ACP operation. With increasing rotor frequency the mean flap deflection angle decreases for every ACP trailing edge flap, while the standard deviation also decreases. Recalling that a trailing edge flap angle of 0° corresponds to the rigid Clark-Y profile, the pre-tensions have been adjusted so that the ACP operated in ranges around this default value. Examining the mean values listed in table 4.2, they ranged between about 2° and -6° for all investigated rotor frequencies. The exact values of pre-tension for the multi-section rotor blade are given in subsection 3.4.1.

Figure 4.18 shows the trailing edge flap angle movement over the azimuthal angle for pre-tension 1, rotor frequency $f = 2.5\ Hz$ and rotor plane yaw angle $\phi = -30°$. Similar to the discussion of trailing edge flap movement for single section ACP operation, first the movement of flap 3 (outer ACP section) will be examined, since this is in the same position as the single ACP segment on Blade-2.

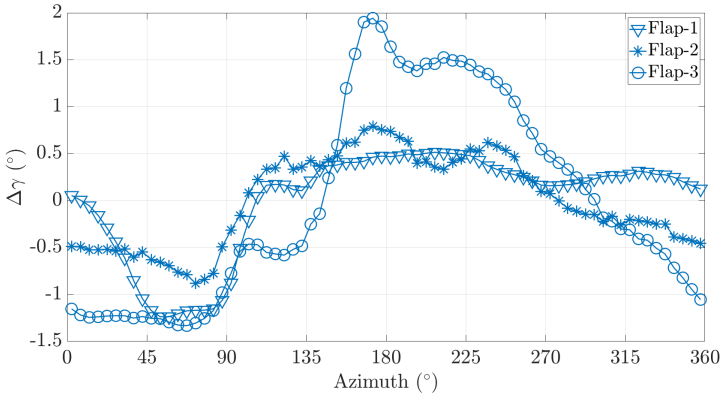

Figure 4.18: Trailing edge flap angle γ at 2.5 Hz rotor frequency and a rotor plane yaw angle $\phi = -30°$ over the azimuthal angle θ and for the pre-tension setting-1. The mean flap angle has been subtracted.

The trailing edge flap amplitude is about the same as observed for single section ACP operation, as presented in figure 4.14. The dips in the curve at azimuthal angles of about 90° and 270°, as well as the maximum camber are shifted to an earlier azimuthal position. The first dip is now located exactly at an azimuthal angle of 90°, while the second dip is located exactly at an azimuth angle of 270°, where they are expected to be due to the effective plunging motion induced by the yawed rotor plane. The maximum camber of the ACP is now attained at an azimuthal angle of $\phi = 180°$ corresponding to the tower passage. The observed behaviour, and especially the deviations from the values obtained for single-section ACP operation, indicates that the inner ACP sections on Blade-3 influence the incident blade flow, presumably the fluctuations of the side-slip angle β; hence v_{Tr}. The sign change of v_{Tr} is located exactly at an azimuthal angle of 180°, where it is expected due to geometrical considerations. This is evident in the blade incident flow data shown in figure 4.9. The inner ACP segments on the rotor provoke a faster decrease of v_{Tr} to its change of direction by damping or preventing the dynamic stall evolution from span positions near the hub towards the tip.

From outer to inner span positions the effective plunging amplitude and velocity (v_{plunge}) decrease and the dominating component of the blade incident velocity (v_{Tx}) fluctuations becomes v_{Tr}, i.e. the component tangential to the leading edge. This velocity also arises due to the yawed rotor plane. Furthermore, with decreasing r, the rotation speed Ωr decreases and v_2 becomes a more dominant component of the velocity triangle. This leads to high AoA fluctuations at high mean AoAs and low incident blade velocities, which result in dynamic stall.

Moreover, from tip to hub, the ratio between the circumference that a blade section subscribes during its rotational motion and the chord decreases. In other words, the profile experiences a faster variation of inflow conditions and also a different temporal influence from the tower shadow.

The above considerations are reflected in the trend of the trailing edge flap movement of ACP sections 1 and 2 pictured in figure 4.18. The dips attributed to the plunge motion ($\theta = 90°, 270°$) are only marginal and the tower distortion in flap movement is observed over a wider azimuthal angle range at these inner ACP segments.

Figure 4.19 shows the curves of trailing edge flap movement measured at a rotor frequency of 2.5 Hz and a rotor plane yaw angle of $\phi = -30°$ with pre-tension 2. The curves exhibit qualitatively the same trends as with pre-tension 1. It must be noted that the difference between the adjusted pre-tensions in single section operation is much smaller than the difference between the adjusted pre-tensions in multi-section operation, as described in subsection 3.4.1.

Comparing the curves in figure 4.18 with the curves in figure 4.19, it can be observed that an increase of pre-tension not only shifts the trailing edge flap angle to higher mean camber values, but also reduces the amplitude of the flap deflection.

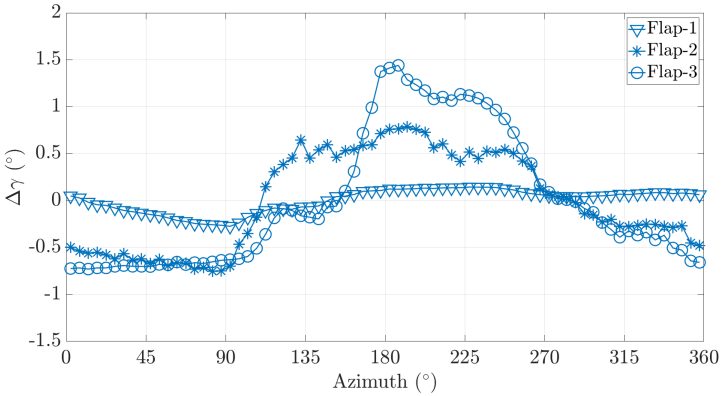

Figure 4.19: Trailing edge flap angle γ of ACP segments 1,2 and 3 at 2.5 Hz rotor frequency and for a rotor plane yaw angle $\phi = -30°$ over the azimuthal angle θ for the pre-tension setting-2. The mean flap angle has been subtracted.

Figure 4.20 shows the data of the trailing edge flap movement at a rotor frequency of 3.0 Hz and pre-tension 1. The movement of the outer flaps has become marginal, while the ACP segment 1 has become the most active one. The observation is plausible due to the discussed decrease of mean AoA and AoA amplitudes with increasing rotor frequency.

Figure 4.21 shows the trailing edge flap angle at a rotor frequency of 3.0 Hz for pre-tension setting-2. The ACP response is almost completely suppressed. Obviously this pre-tension value is inappropriate for these operation conditions.

Figure 4.22 shows the trailing edge flap angles of Blade-3 at 3.5 Hz rotor frequency and pre-tension 1. Because of the small gust amplitudes and low mean values of AoAs, unsteady ACP operation is no longer observable and there is a steady adjustment of the profile camber over azimuthal angle. Attached flow can be expected over the entire blade span. The velocity and AoA fluctuations are sufficiently high to actuate the ACP mechanism only at the

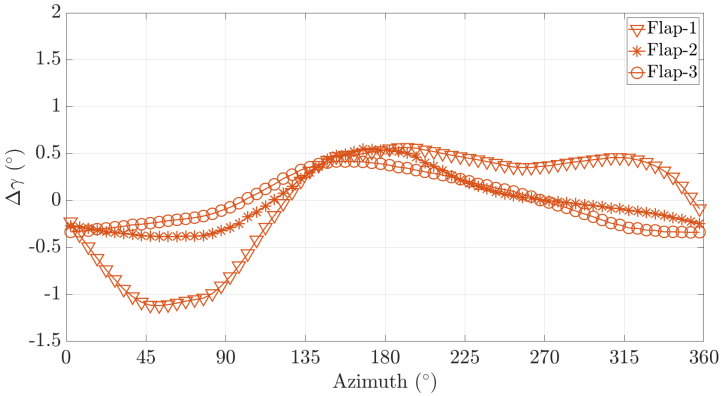

Figure 4.20: Trailing edge flap angle γ of ACP segments 1,2 and 3 at 3.0 Hz rotor frequency and a rotor plane yaw angle $\phi = -30^{\circ}$ over the azimuthal angle θ and for pre-tension setting-1. The mean flap angle has been subtracted.

innermost ACP segment 1.

Figure 4.23 shows the out-of-plane root bending (OPRB) data of Blade 3 in multi-section ACP operation compared to the rigid blade data at a rotor frequency of 2.5 Hz and a rotor plane yaw angle of $\phi = -30^{\circ}$. Compared to the corresponding data for single-section ACP operation presented in figure 4.16, a higher peak load reduction of about 10% compared to the rigid blade can be observed.

A significant observation is the smoother trend of the OPRB curves and the higher mean loadings with the ACP operation compared to those with the rigid blade in the azimuthal angle range $220^{\circ} < \theta < 360^{\circ}$. The ACP in multi-section operation significantly reduces the periodic dynamic load fluctuations and increases the mean load over a wide azimuthal angle range. Local load enhancements of about 30% compared to the rigid blade can be observed. In this azimuthal angle range the rigid blade exhibits extreme local fluctuations, presumably arising from dynamic stall phenomena. The ACP mechanism in

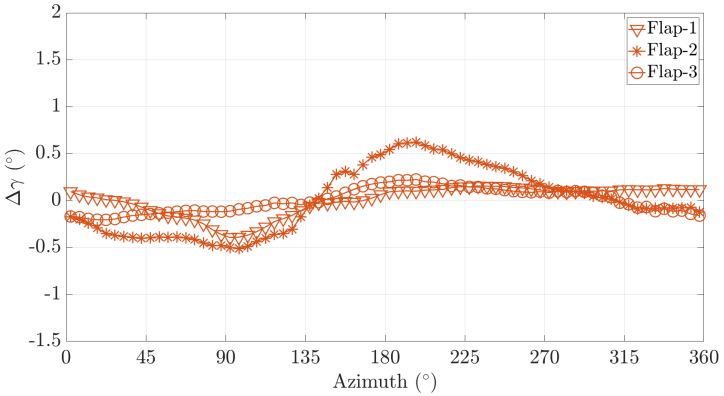

Figure 4.21: Trailing edge flap angle γ of ACP segments 1,2 and 3 at 3.0 Hz rotor frequency and for a rotor plane yaw angle $\phi = -30°$ over the azimuthal angle θ and for pre-tension setting-2. The mean flap angle has been subtracted.

multi-section operation is able to suppress these effects, leading to a smoother change of OPRB values.

These observations already lead to the conclusion that the ACP is able to increase mean thrust and partially suppress fluctuations of rotor blade bending. That indicates the potential of the ACP concept to increase the lifetime of turbines, to decrease maintenance costs and to increase power output. Furthermore, the dynamic stall scenario in section 2.2.1 has been identified as the most critical scenario for the structural integrity of turbines in extreme gust scenarios. With the ability to probably prevent dynamic stall on rotor blades, the ACP concept has proven to be an effective gust load alleviation approach.

The minima of the OPRB curves are located around an azimuthal angle of 180°. As observed for single-section ACP operation at a rotor frequency of 2.5 Hz, the OPRB minimum of all curves lies nearly at the same value. Considering that the AoA at this azimuthal angle exceeds the total stall limit

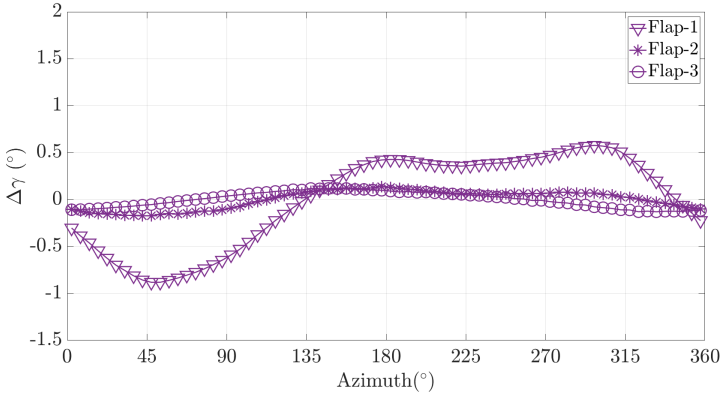

Figure 4.22: Trailing edge flap angle γ of ACP segments 1,2 and 3 at 3.5 Hz rotor frequency and for a rotor plane yaw angle $\phi = -30°$ over the azimuthal angle θ for pre-tension setting-1. The mean flap angle has been subtracted.

of 20° over a wide range of the blade span, it can be concluded that the minimum in this operational point is determined by a loss of lift due to total stall. The total stall limit of a profile cannot be sufficiently shifted upwards by ACP de-cambering, especially not with the present ACP design.

When comparing the curves in figure 4.23, an increasing phase shift of several features with decreasing pre-tension can be observed. This behaviour can be explained by the fact that, compared to a rigid profile, the more a profile de-cambers the earlier it reaches its lift maximum during a periodic gust. This is a known behaviour, also described and explained by Cordes (2016) or Wester et al. (2018a).

Figure 4.24 shows the OPRB curves related to the multi-section ACP operation at a rotor frequency of 3 Hz. Comparing these curves with curves presented in figure 4.23, it can be observed that they are smoother and the higher frequency fluctuations are almost non-existent. Presumably the higher frequency fluctuations in the OPRB curves can be attributed to the dynamic

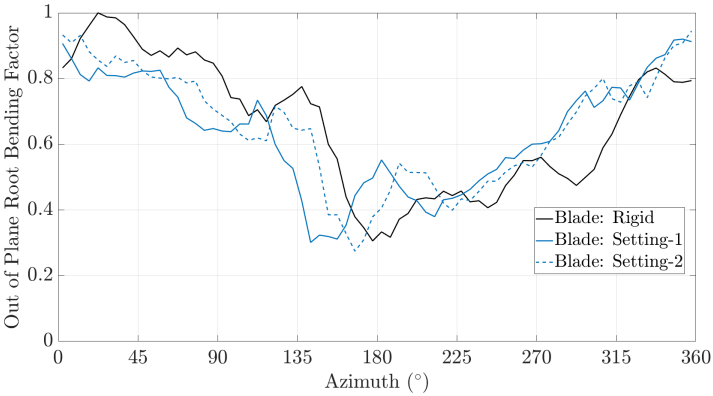

Figure 4.23: Comparison of measured phase averaged dimensionless out-of-plane root bending data at a rotor frequency of 2.5 Hz. Data for the rigid blade is compared with ACP data of Blade-3 at two different pre-tension settings and for a rotor plane yaw angle $\phi = -30°$.

stall evolution on the rotor blade. While at a rotor frequency of 2.5 Hz, fluctuations of the AoA of about 10°to 22°are observed at 50% of the blade radius, the fluctuation of the AoA at $3.0Hz$ is in the range of 7°to 15°. The first case is called "deep dynamic stall" and the second case is called "light dynamic stall". The operating point at a rotor frequency of 3.0 Hz is therefore a very unstable case with regard to the characteristics of the load behaviour. Small changes in the setting of the ACP parameters can cause large effects. The smooth curve for spring pre-tension 1 indicates that the ACP is able to reduce the dynamic stall evolution on the rotor blade.
The OPRB behaviour with pre-tension 2 exhibits the largest fluctuations. This illustrates nicely the fact that, if the ACP pre-tension is not properly adjusted, the ACP does not work in the desired manner. This has also been mentioned by Cordes (2016) and Klein (2019).

Figure 4.25 shows the OPRB curves measured at a rotor frequency of 3.5 Hz. The flexible curve over the entire rotation lies beneath the curve for the rigid blade. Almost all profile sections except for ACP segment 1 oper-

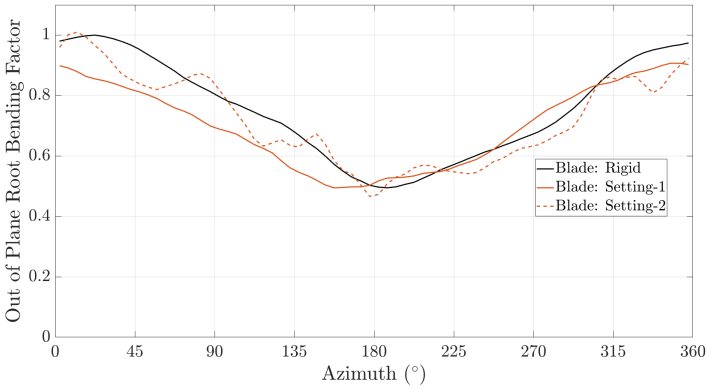

Figure 4.24: Comparison of measured phase averaged dimensionless out-of-plane root bending data at a rotor frequency of 3.0 Hz. Data for the rigid blade is compared with ACP data of Blade-3 at two different pre-tension settings and for a rotor plane yaw angle $\phi = -30°$.

ate in the attached flow regime and the AoA amplitudes and mean AoAs are smaller when compared to the other operation points. The OPRB minimum is no longer determined by the total stall limit. The entire curve for the ACP blade is shifted to lower out-of-plane root bending moments, caused by a steady de-cambering of the ACP. The behaviour can be explained by the findings of Lambie (2011). In this case the average load was reduced while maintaining the same load amplitude. With regard to a desired prolongation of the life of turbines with the same or increased energy yield, this behaviour is not optimal. Desired in this sense is a reduction of the dynamic load amplitude at a constant average load, as observed with the rotor frequencies of 2.5 Hz and 3 Hz.

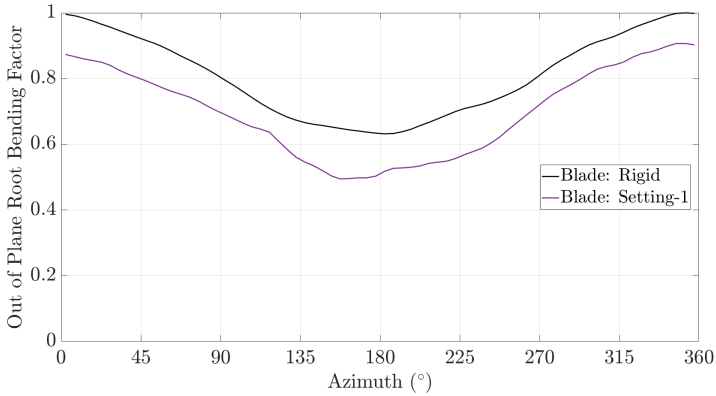

Figure 4.25: Comparison of measured phase averaged dimensionless out-of-plane root bending data at a rotor frequency of 3.5 Hz. Data for the rigid blade is compared with ACP data of Blade-3 at two different pre-tension settings and for a rotor plane yaw angle $\phi = -30°$.

4.4 Comparison with QBlade Computations

In the following, the curves of the OPRB factor discussed in chapter 4.3 are presented in comparison with curves of QBlade simulations of the rigid blade. The deviation between simulations and measurements is discussed in terms of the simulated and measured incident flow on blades, presented in section 4.1.

It is assumed that the trend of the OPRB curves depends on the trend of the total velocity v_T and the AoA trend. Hence, it is assumed that the position at 50% of the blade span is an adequate reference for the interpretation of the trends of the OPRB curves.

Figures 4.26, 4.27 and 4.28 show the OPRB curves at the three rotor frequencies, 2.5 Hz, 3.0 Hz and 3.5 Hz. Examining the curves, some main observations can be summarised:

- The position of the OPRB minimum agrees relatively good between measured and simulated curves of the rigid blade.

- The OPRB minimum of the measured and simulated curves at a rotor frequency of 2.5 Hz agrees very well.
- The minimum value of the simulated curve of the rigid blade at the rotor frequencies 3.0 Hz and 3.5 Hz lies about 10% higher than that of the measured curve of the blade in rigid condition
- The OPRB maximum of the simulated curves of the rigid blade exhibits a shift towards higher azimuthal angles θ with increasing rotor frequency.

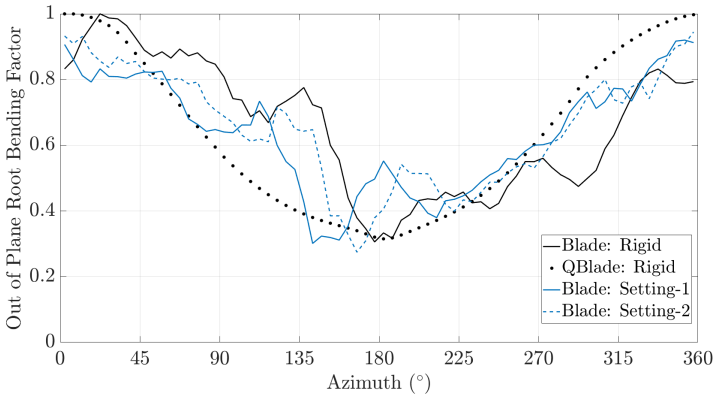

Figure 4.26: Curves of phase averaged dimensionless out-of-plane root bending data measured at a rotor frequency of 2.5 Hz and for a rotor plane yaw angle ϕ = - 30° complemented with the curve derived of a QBlade LFFVW simulation for the rigid blade. The results of the simulation are non-dimensionalised for percentage comparison with the measured curves.

Figure 4.29 shows the AoA data already presented in section 4.1 and complemented with QBlade simulations over an azimuthal angle range from 160° to 300°. The measured and simulated curves agree well regarding their maxima. The maximum is located at an azimuthal angle of about 180° and corresponds to the position of the minimum of the presented OPRB curves. The assertion that the minimum of the OPRB curves is determined by a total stalled situation is verified with the curves measured and simulated for a rotor frequency

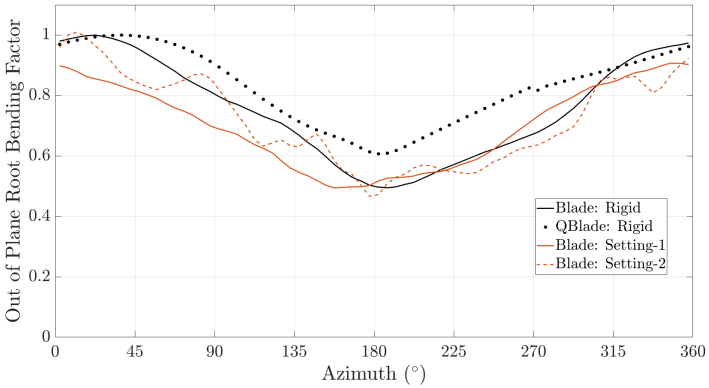

Figure 4.27: Curves of phase averaged dimensionless out-of-plane root bending data measured at a rotor frequency of 3.0 Hz and a rotor plane yaw angle ϕ = -30° complemented with the curve derived of a QBlade LFFVW simulation for the rigid blade. The results of the simulation are non-dimensionalised for percentage comparison with the measured curves.

of 2.5 Hz. The minimum of the curves is determined by the total stall AoA limit of 20° defined in chapter 2. That is obviously the reason why QBlade in that case predicts the same OPRB minimum value as the measurement. The code assumes a total breakdown of lift at a specific AOA.

At a rotor frequency of 3.0 Hz the maximum AoA of the simulated and measured curves is at about 15°, while at a rotor frequency of 3.5 Hz it is located under an AoA of 10°, where attached flow conditions can be assumed. The reason for the higher minimum of the simulated curves with respect to the measured curves can not be found in the AoA trends, since they agree well in every sense.

Figure 4.30 depicts the velocity v_{T2d} seen by a blade profile at 50% of the blade span, complemented with Qblade simulations over an azimuthal angle θ range from 160° to 300°. The curves measured and simulated at a rotor frequency of 2.5 Hz agree well. The gradient of the simulated curves at a

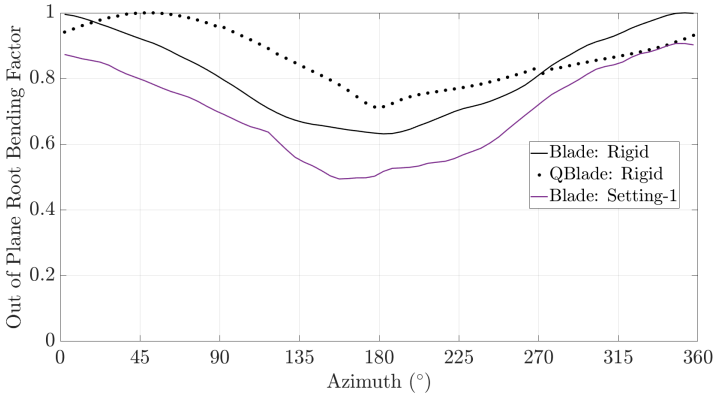

Figure 4.28: Curves of phase averaged dimensionless out-of-plane root bending data measured a rotor frequency of 3.5 Hz and for a rotor plane yaw angle ϕ = -30° complemented with the curve derived of a QBlade LFFVW simulation for the rigid blade. The results of the simulation are non-dimensionalised for percentage comparison with the measured curves.

rotor frequency of 3.0 Hz and 3.5 Hz beyond an azimuthal angle of 180° is clearly higher than that of the measured curves. A higher acceleration leads to higher loads and may cause the higher OPRB minimum of the simulated curves compared to the measured curves at said frequencies.

It is assumed that the azimuthal position of the OPRB maximum is determined by both the AoA and v_{T2d}. Figure 4.31 shows the AoA trends of the measured and simulated curves over an azimuthal angle range from 320° to 120°. Figure 4.32 shows the trends of v_{T2d} of the measured and simulated curves over an azimuthal angle range from 320° to 120°.

It is asserted that the OPRB maximum of the measured and simulated curves at rotor frequencies of 2.5 Hz and 3.0 Hz fits roughly. That is explained with the observation that the corresponding AoA and v_{T2d} trends fit roughly regarding their gradients.

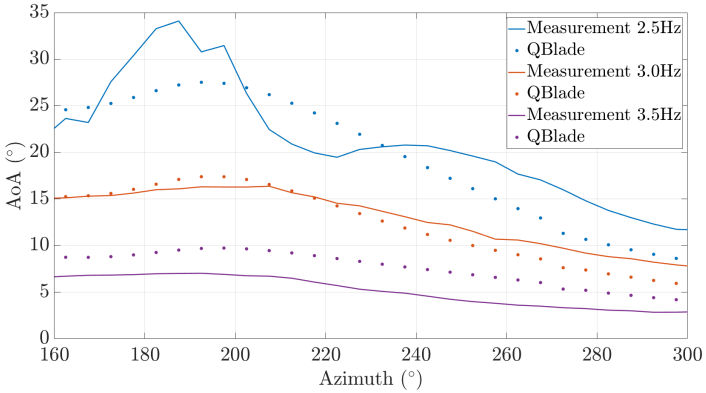

Figure 4.29: Measured and simulated AoA α curves at rotor frequencies of 2.5 Hz, 3.0 Hz and 3.5 Hz and for a rotor plane yaw angle ϕ = -30° over an azimuthal angle θ range of 160° to 300°. The curves represent the AoA trend at 50% of the blade span.

The OPRB maximum of the simulated curve is located about at an azimuthal angle of about 45°, while the OPRB maximum of the measured curve is located at an azimuthal angle of about 0°. A significant difference regarding the corresponding AoA and v_{T2d} trends can be observed, which obviously causes the shift in the OPRB maxima.

The OPRB maximum of the measured curve seems to be determined by reaching the maxima of the v_{T2d} trend, while the corresponding AoA trend proceeds flat in the specific azimuthal angle range. The OPRB maximum of the simulated curve seems to be determined by an increasing gradient of the AoA curve, while v_{T2d} slowly decreases in the specific azimuthal angle range.

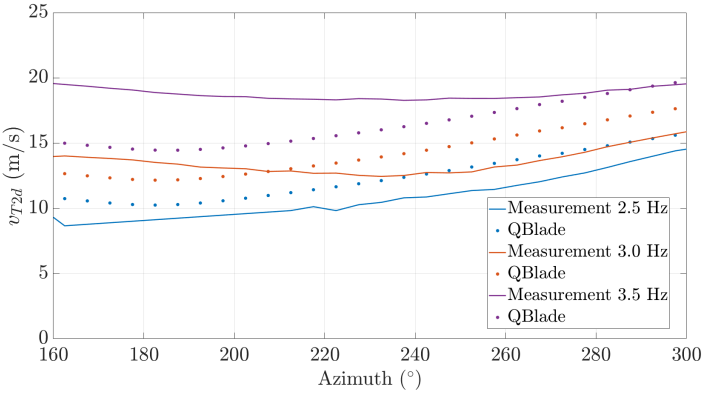

Figure 4.30: Measured and simulated velocity v_{T2d} seen by a blade profile at 50% of the blade span for a rotor plane yaw angle of ϕ = -30°. Data is gathered at rotor frequencies of 2.5 Hz, 3.0 Hz, and 3.5 Hz and depicted for an azimuthal angle θ range of 160° to 300°.

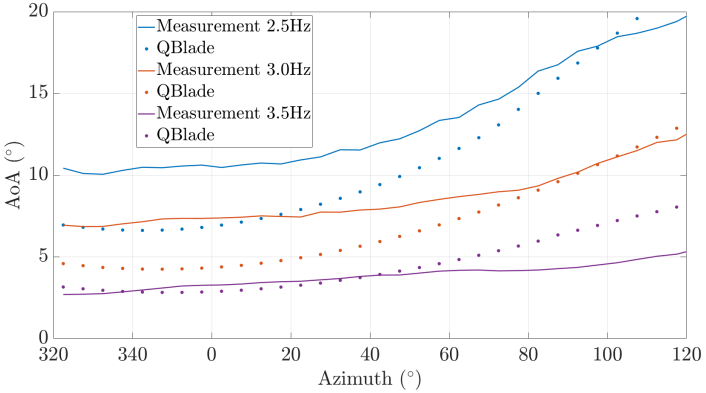

Figure 4.31: Measured and simulated AoA α curves at rotor frequencies of 2.5 Hz, 3.0 Hz and 3.5 Hz and for a rotor plane yaw angle ϕ = -30° over an azimuthal angle θ range of 320° to 120°. The curves represent the AoA trends at 50% of the blade span.

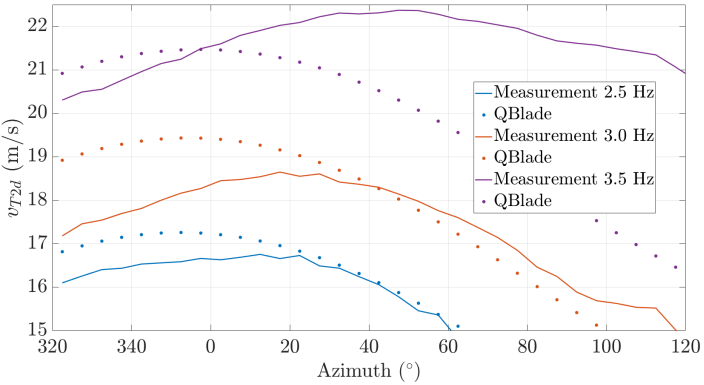

Figure 4.32: Measured and simulated velocity v_{T2d} seen by a blade profile at 50% of the blade span for a rotor plane yaw angle ϕ = -30°. Data is gathered at rotor frequencies of 2.5 Hz, 3.0 Hz, and 3.5 Hz and depicted over an azimuthal angle θ range of 320° to 120°.

The measured and simulated OPRB trends for the blade in rigid condition at a rotor frequency of 2.5 Hz, pictured in figure 4.26, compared to the rest of the investigated rotor frequencies fit best regarding to their mean trend. That accordance is explained by the fact that QBlade in that operation point is able to predict the incident flow at the blade well.

The QBlade simulation does not show the local ups and downs in the trend, which can be observed in the trend of the the measured curve of the rigid blade, caused by evolving dynamic stall vortexes at the blade, because no dynamic stall model could be activated in actual simulations.

In figure 4.26 it can be observed that the trend of the simulated curve agrees remarkably well with the trend of the curves measured with all ACP sections in operation within an azimuthal angle range of 20° to 360°. The curves differ at an azimuthal angle of about 270° because of the desired ACP impact in respect to peak load reduction only.

The said azimuthal angle range has been discussed in section 4.3 and identified as the azimuthal angle range within which the ACP is able to avoid the dynamic stall evolution at the blade successfully. If dynamic stall is suppressed by an adequate mechanism, no dynamic stall model in the simulation is needed to predict the OPRB curve correctly.

This section emphasises that a correct prediction of the incident blade inflow, as well as an adequate prediction of the dynamic stall phenomena is crucial for the prediction of unsteady aerodynamic loads.

5 Conclusion and Outlook

This chapter summarises the main conclusions of this study and suggests future research topics to further the understanding and development of passively deforming camber rotor blades.

5.1 Conclusion

The overall goal of this study was to experimentally demonstrate the functionality of the ACP concept on a model wind turbine. More precisely, compared with the performance of rigid blades, gust loads should be alleviated while simultaneously improving the overall power output of the turbine. Furthermore, the experimental investigation should improve the physical understanding and analytical approaches for the design of an ACP rotor blade operating under unsteady aerodynamic conditions. The main achievements of this study can be discussed in the light of the following fundamental areas:

- Model design and manufacturing
- Experimental investigation
- Analytical considerations

Model design and manufacturing

An ACP design has been developed and realised in the rotor of a model wind turbine. The concept is suitable for implementation in real turbines with larger rotor diameters. A conventional blade can be adapted to accept the ACP mechanism without unduly diminishing the structural integrity of the blade. The essential ACP parameters, specifically the pre-tension and spring stiffness, are convenient to adjust and monitor and the entire mechanism can

be housed inside the blade profile.

A measurement concept to investigate the ACP operation in the rotating system of a wind turbine has been developed and successfully demonstrated. Wireless data transmission combined with custom-built five-hole pressure probes to measure the blade incident flow and monitoring of the torsion spring connected to the flap hinge using angle sensors are mature concepts available for use in field studies with prototype turbines.

Experimental investigation

A realistic gust generation has been realised using a yawed rotor plane of the Berlin Research Turbine - BeRT. By varying rotor frequency, a large range of relevant gust scenarios resulted, depending on the azimuthal angle and the rotor radius. This includes fully attached flow, dynamic stall cycles, plunging motion as well as three-dimensionality through a geometrically induced sideslip velocity. In many cases several of these effects were superimposed on one another.

A proof of concept has been delivered regarding the functionality of the ACP in a rotating system. Using single-section blades, a peak bending load reduction of up to 10% has been achieved compared to rigid blades. Dynamic stall cycles have been prevented or at least reduced compared to rigid blades. Furthermore, the mean lift could be maintained up to 20% higher over large azimuthal angle ranges. This leads to higher energy output and presumably to longer blade lifetime through reduced cyclic loading. The multi-flap results indicate that the ACP can function advantageously at all blade radii. Near the root the ACP reduced dynamic stall development; hence critical gust loading. However the ACP influences the velocity at the rotor plane (v_2) in a manner which increases the power curve of the turbine.

Analytical considerations

The blade incident flow resembles closely the conditions addressed with the theory of Theodorsen for a plunging flat plate. The measurement re-

sults confirm that this such conditions exist; however, these are complicated through the existence of a side-slip velocity arising from the yawed rotor plane. Therefore, the unsteadiness encountered on a turbine blade is not likely to be captured using simplified analytic models or blade element theory, such as those implemented in the code QBlade. At present these additional effects can probably only be captured using empirical corrections or by reverting to a full simulation of the flow, for instance using finite-volume codes (CFD).

The situation becomes even more complex when introducing the adaptive camber profile on the rotor blades. For this case the present results suggest that existing models for dynamic stall may no longer be appropriate, since the ACP can strongly influence the stall behaviour of the blade. Moreover, numerical simulations of the turbine with ACP must also include fluid structure interaction and account for several degrees of freedom in the ACP mechanism. Thus, future experimental investigations appear to be indispensable to further develop and refine the design and implementation of the ACP concept for wind turbines.

5.2 Suggestions for Future Research

Complementing the work of Lambie (2011), Spiegelberg (2014) and Cordes (2016), the present study definitively demonstrates the functionality of the ACP concept for gust load alleviation on wind turbines. Furthermore, it illuminates the complexity demanded of analytical approaches to describe the ACP response under realistic unsteady turbine flow conditions. A proof of concept has been established and this then leads to the question of what steps are now necessary for realising the concept in field units, in particular regarding interaction with other common control mechanisms and devices?

One of the first steps is to examine in detail the economic return of the concept, since this in the end will determine whether a return on investment can be realised. This can be considered in terms of the COE factor introduced in section 2.1. Accordingly, three topics have to be investigated and quantified:

- Increase of turbine lifetime
- Increase of power output
- Capital and maintenance costs

Prolonged lifetime can be estimated on the basis of peak load reduction and reduction of periodic/cyclic loads compared to a rigid blade. Such data are essential for fatigue estimates according to e.g. Wöhler curves. First estimates of peak load reduction have been presented with this study.

To estimate the increase of power output due to the ACP an adequate analytic tool is required. For this, long-term field investigations will be necessary to deliver validation data of such a tool. Such field investigations will also deliver first estimates of capital and maintenance costs.

Although the present study has provided integral quantities verifying the functionality of the ACP concept, many details and questions are left open, for instance:

- How does the ACP influence the flow over the blade, for example stall behaviour depending on the position on the blade?
- How does the ACP influence the wake of a rotor?
- How does ACP operation influence the velocity v_2 close to the rotor plane?

In performing experiments in the future it is crucial to define the aims and scope of the investigations. The advantage of the BeRT facility was and is that that ACP rotor blades are available. Further measurements can be performed there, but for an in-depth investigation of the flow the setup has numerous restrictions. To mention a few, the turbine inflow conditions can only be varied in a small velocity range, are not well defined, in-homogeneous and definitely not uniform across the tunnel cross-section. Also the possibilities for gust generation are restricted.

The University of Oldenburg has implemented a research turbine in a new active grid wind tunnel. Rotor experiments under controlled unsteady inflow conditions can be realised with this facility. The turbine and tunnel has been described in Petrovic et al. (2019) and Berger & Kühn (2018). Berger et al. (2018) describes the investigation of the turbine under turbulent inflow conditions generated by the active grid. Sedano et al. (2019) provides a CFD validation of the setup. The conditions appear to be promising for future research activities.

Otherwise a number of aims can be identified to further develop the ACP design.

- reduce the number of mechanical parts as well as gaps in the profile at hinge points
- adapt the construction for field tests on large-scale turbines
- monitor functionality and durability over long-term tests
- investigate performance and interaction when operating with other turbine control devices

The ACP has been presented as a fully passive, locally acting flow control device. However, the present investigation has underlined the necessity of adjusting the pre-tension and spring stiffness according to prevalent flow conditions. It is therefore conceivable, with minimal sensor input, to make these adjustment active; hence, optimised for instantaneous inflow conditions.

Bibliography

Akkala, J. M. & Buchholz, J. H. J. (2016). Vorticity transport mechanisms governing the development of leading-edge vortices. *Journal of Fluid Dynamics*, Vol.829:P.512–537. -URL https://doi.org/10.1017/jfm.2017.559.

Atassi, H. (1984). The Sears problem for a lifting airfoil revisited - new results. *Journal of Fluid Mechanics*, Vol.141:P.109–122. -URL https://doi.org/10.1017/S0022112084000768.

Baik, Y. S., Bernal, L. P., Granlund, K., & Ol, M. V. (2012). Unsteady force generation and vortex dynamics of pitching and plunging aerofoils. *Journal of Fluid Dynamics*, Vol.709:P. 37 – 68. -URL https://doi.org/10.1017/jfm.2012.318.

Bak, C., Madsen, H. A., & Johansen, J. (2001). Influence from blade-tower interaction on fatigue loads and dynamics (poster). In *2001 European Wind Energy Conference and Exhibition (EWEC'01)*. WIP Renewable Energies.

Bangga, G. S., Lutz, T., & Krämer, E. (2015). An examination of rotational effects on large wind turbine blades. *11th EAWE PhD Seminar on Wind Energy in Europe, Stuttgart*, Sep,2015.

Barlas, A. (2011). *Active Aerodynamic load control on wind turbine blades: Aeroservoelastic modelling and wind tunnel experiments*. Dissertation, TU Delft.

Barlas, T. K. & van Kuik, G. A. M. (2009). Review of state of the art in smart rotor control research for wind turbines. *Progress in Aerospace Sciences*, Vol.46(1):P. 1 – 27. -URL https://doi.org/10.1016/j.paerosci.2009.08.002.

Bell, C. (2013). *Beginning Sensor Networks with Arduino and Raspberry Pi*. No.1. Springer Science+Business Media New York. ISBN: 978-1-4302-5824-7.

Bergami, L. & Gauna, M. (2014). Analysis of aeroelastic loads and their contributions to fatique damage. *Journal of Physics: Conference Series*, Vol.555(1):P. 012007. -URL https://doi.org/10.1088/1742-6596/555/1/012007.

Berger, F., Kröger, L., Onnen, D., Petrovic, V., & Kühn, M. (2018). Scaled wind turbine setup in a turbulent wind tunnel. *Journal of Physics: Conference Series*, Vol.1104(1):P.012026. -URL https://doi.org/10.1088/1742-6596/1104/1/012026.

Berger, F. & Kühn, M. (2018). Experimental investigation of dynamic inflow effects with a scaled wind turbine in a controlled wind tunnel environment. *Journal of Physics: Conference Series*, Vol.1037:P.052017. -URL https://doi.org/10.1088/1742-6596/1037/5/052017.

Bernhammer, L. O., van Kuik, G. A. M., & Breuker, R. D. (2016). Fatigue and extreme load reduction of wind turbine components using smart rotors. *Journal of Wind Engineering and Industrial Aerodynamics*, Vol.154:P. 84 – 95. -URL https://doi.org/10.1016/j.jweia.2016.04.001.

Betz, A. (1924). *Wind-Energie und ihre Ausnutzung durch Windmühlen.* No.1. Vandenhoeck & Ruprecht, Göttingen, reprint: Öko-Buchverlag Kassel 1994. ISBN: 978-3922964117.

Bottasso, C. L., Groce, A., Gualdoni, F., & Montinari, P. (2016). Load mitigation for wind turbines by a passive aeroelastic device. *Journal of Wind Engineering and Industrial Aerodynamics*, Vol.148:P. 57 – 69. -URL https://doi.org/10.1016/j.jweia.2015.11.001.

Burton, T., Sharpe, D., Jenkins, N., & Bossanyi, E. (2011). *Wind Energy Handbook.* 2. John Wiley & Sons LTD. ISBN: 978-0470699751.

Butterfield, C. P., Hansen, A. C., Simms, D., & Scott, G. (1991). Dynamic stall on wind turbine blades. *Wind Power 91' Conference Palm Springs, CA*, Vol.91. -URL.

Carr, L. W., McAlister, K. W., & McCroskey, W. (1977). Analysis of the development of dynamic stall based on oscillating airfoil experiments. *Technical report, NASA Ames Research Center*, Vol.8382. -URL https://ntrs.nasa.gov/search.jsp?R=19770010056.

Carr, L. W., McCroskey, W. J., & McAlister, K. W. (1978). Dynamic stall experiments on the naca 0012 airfoil. *Technical report, NASA Ames Research Center*, Vol.1100. -URL https://ntrs.nasa.gov/search.jsp?R=19780009057.

Chandrasekhara, M. S., Wilder, M. C., & Carr, L. W. (1998). Unsteady stall control using dynamically deforming airfoils. *AIAA Journal*, Vol.36:P. 1792 – 1800. -URL https://doi.org/10.2514/2.294.

Chen, T. & Liou, L. (2011). Blockage corrections in wind tunnel tests of small horizontal-axis wind turbines. *Experimental Thermal and Fluid Science*, 35(3):565–569.

Choudhry, A., Arjomandi, M., & Kelso, R. (2016). Methods to control dynamic stall for wind turbine applications. *Renewable Energy*, Vol.86:P. 26 – 37. -URL https://doi.org/10.1016/j.renene.2015.07.097.

Cordes, U. (2016). *Experimental Investigation of a Passively Deforming Airfoil Under Dynamic Flow Conditions*. Dissertation, TU Darmstadt.

Drela, M. (2014). *Flight Vehicle Aerodynamics*. 1. MIT Press Ltd. ISBN: 978-0262526449.

Fedorov, V. & Bergreen, C. (2014). Bend-twist coupling potential of wind turbine blades. *Journal of Physics: Conference Series*, Vol.524:P. 012035. -URL https://doi.org/10.1088/1742-6596/524/1/012035.

Feszty, D., Gillies, E. A., & Vezza, M. (2003). Alleviation of rotor blade dynamic stall via trailing edge flap flow control. *AIAA Paper41st Aerospace Sciences Meeting & Exhibit, Reno*, Vol.41:P. 26 – 37. -URL https://doi.org/10.2514/6.2003-50.

Fingersh, L., Hand, M., & Laxson, A. (2006). Wind turbine design cost and scaling model. *Technical Report NREL/TP-500-40566*, Vol.13. -URL https://doi.org/10.2172/897434.

Galloway, P. W., Myers, L. E., & Bahaj, A. S. (2013). Quantifying wave and yaw effects on a scale tidal stream turbine. *Renewable Energy*, Vol.63:P. 297 – 307. -URL https://doi.org/10.1016/j.renene.2013.09.030.

Gasch, R. & Twele, J. (2010). *Windkraftanlagen; Grundlagen,Planung und Betrieb*. 6. Vieweg+ Teubner. ISBN: 978-3-8348-0693-2.

Gerontakos, P. & Lee, T. (2006). Dynamic stall flow control via a trailing-edge flap. *AIAA Journal*, Vol.44:P. 469 – 479. -URL https://doi.org/10.2514/1.17263.

Goldstein, M. E. & Atassi, H. (1976). A complete second-order theory for the unsteady flow about an airfoil due to a periodic gust. *Journal of Fluid Mechanics*, Vol.74:P.741–764. -URL https://doi.org/10.1017/S0022112076002036.

Grothe, K. H. & Feldhusen, J., editors (2007). *DUBBEL Taschenbuch für den Maschinenbau*. Vol.20. Springer Berlin Heidelberg New York. ISBN: 978-3-540-49714-1.

Gülçat, U. (2016). *Fundamentals of Modern Unsteady Aerodynamics*. 2. Springer Science+Business Media Singapore. ISBN: 978-981-10-0018-8.

Herráez, I., Stoevesand, B., & Peinke, J. (2014). Insight into rotational effects on a wind turbine blade using navier- stokes computations. *Energies*, Vol.7:P. 6798 – 6822. -URL https://doi.org/10.3390/en7106798.

Hirai, S., Honda, A., & Kariromi, K. (2008). Wind loads investigations of hawt with wind tunnel tests and site measurements. *Wind Power Asia, Beijing*.

Horowitz, P. & Hill, W. (2015). *The Art of Electronics*. Vol.3. Cambridge University Press. ISBN: 978-0521809269.

Hufnagel, K. & Lambie, B. (2013). Invention relating to rotor blades in particular for wind power installations. Patent: EP 2 569 535 B1, -URL https://patents.google.com/patent/EP2569535B1/de.

Hütter, U. (1942). *Beitrag zur Schaffung von Gestaltungsgrundlagen für Windkraftwerke*. Dissertation, TH Wien.

Johnson, S. J., Baker, J. P., van Dam, C. P., & Berg, D. (2010). An overview of active load control techniques for wind turbines with an emphasis on microtabs. *Wind Energy*, Vol.13:P. 239 – 253. -URL https://doi.org/10.1002/we.356.

Klein, A. C. (2019). *Numerische Studien zur Lastenkontrolle an Windenergieanlagen mittels gekoppelter Vorder- und Hinterklappen*. Dissertation, Universität Stuttgart.

Klein, A. C., Bartholomay, S., Marten, D., Lutz, T., Pechlivanoglou, G., Nayeri, C. N., Paschereit, C. O., , & Krämer, E. (2017). About the suitability of different numerical methods to reproduce model wind turbine measurements in a wind tunnel with a high blockage ratio. *Wind Energy Science*, Vol.3:P. 439–460. -URL https://doi.org/10.5194%2Fwes-3-439-2018.

Knebel, P., Kittel, A., & Peinke, J. (2011). Atmospheric wind field conditions generated by active grids. *Experiments in Fluids*, Vol.51:P.471–481. -URL https://doi.org/10.1007/s00348-011-1056-8.

Kramer, M. (1932). Increase in the maximum lift of an airplane wing due to a sudden increase in its effective angle of attack resulting from a gust. *Zeitschrift für Flugtechnik und Motorluftschifffahrt*, Vol.23:P. 185 – 189. -URL https://ntrs.nasa.gov/search.jsp?R=19930094738.

Lambie, B. (2011). *Aeroelastic Investigation of a Wind Turbine Airfoil with Self-Adaptive Camber*. Dissertation, TU Darmstadt.

Leishman, J. & Beddoes, T. (1989). A semi-empirical model for dynamic stall. *Journal of the American Helicoter Society*, Vol.34:P. 3–17. -URL https://doi.org/10.4050/JAHS.34.3.3.

Leishman, J. G. (2006). *Principles of Helicopter Aerodynamics*. Vol.2. Cambridge University Press. ISBN: 978-0-521-85860-1.

Lobitz, D. & Veers, P. (1998). Aeroelastic behavior of twist-coupled hawt blades. *AIAA*, Vol. 98-0029:P. 75 – 83.

Marten, D., Lennie, M., Pechlivanoglou, G., & Nayeri, C. N. (2016). Implementation, optimisation, and validation of a nonlinear lifting line-free vortex wake module within the wind turbine simulation code qblade. *Journal of Engineering for Gas Turbines and Power*, Vol.138(7):P. 072601. -URL https://doi.org/10.1115%2F1.4031872.

Marten, D., Pechlivanoglou, G., Nayeri, C. N., & Paschereit, C. (2010). Integration of a wt blade design tool in xfoil/xflr5. *10th German Wind Energy Conference, Bremen, Germany*, Nov, 2010.

Marten, D., Pechlivanoglou, G., Nayeri, C. N., & Paschereit, C. (2015). Integration of an unsteady nonlinear lifting line free vortex wake algorithm in a wind turbine design framework. *EEWEA Annual Meeting, Paris*, Nov,2015:P. 17–20.

Micallef, D. & Sant, T. (2016). A review of wind turbine yaw aerodynamics. *Wind Turbines(Design, Control and Applications)*, Chapter-2:P. 27 – 53. -URL https://doi.org/10.5772/63445.

Nguyen, K. (1998). Active control of helicopter blade stall. *Journal of Aircraft*, Vol.35(1):P. 91 – 98. -URL https://doi.org/10.2514/2.2264.

Pereira, R., Schepers, G., & Pavel, M. D. (2013). Validation of the beddoes-leishman dynamic stall model for horizontal axis wind turbines using mexico data. *Wind Energy*, Vol.16:P. 207 – 219. -URL https://doi.org/10.1002/we.541.

Petrovic, V., Berger, F., Neuhaus, L., Hölling, M., & Kühn, M. (2019). Wind tunnel setup for experimental validation of wind turbine control concepts under tailor-made reproducible wind conditions. *Journal of Physics: Conference Series*, Vol.1222. -URL https://doi.org/10.1088/1742-6596/1222/1/012013.

Plumley, C., Leithead, W., Jamieson, P., Bossanyi, E., & Graham, M. (2014). Comparison of individual pitch and smart rotor control strategies for load reduction. *Journal of Physics: Conference Series*, Vol.524:P. 012054. -URL https://doi.org/10.1088/1742-6596/524/1/012054.

Reinke, N. (2017). *Application, generation and analysis of turbulent flows.* Dissertation, Carl von Ossietzky Universität Oldenburg.

Roth, K. (1998). *Zahnradtechnik Evolventen-Sonderverzahnungen zur Getriebeverbesserung.* 2. Springer-Verlag Berlin Heidelberg. ISBN: 978-3-642-63778-0.

Sarlak, H., Nishino, T., Martínez-Tossas, L., Meneveau, C., & Sørensen, J. N. (2016). Assessment of blockage effects on the wake characteristics and power of wind turbines. *Renewable Energy*, 93:340–352.

Scherz, P. & Monk, S. (2016). *Practical Electronics for Inventors.* Vol.4. McGraw-Hill Education Ltd. ISBN: 978-1259587542.

Schmitz, G. (1955). Theorie und entwurf von windrädern optimaler leistung. *Wiss. Zeitschrift der Universität Rostock*, Vol.5.

Schreck, S. J., Robinson, M. C., Hand, M. M., & Simms, D. A. (2000). Hawt dynamic stall responde asymmetries under yawed flow conditions. *Wind Energy*, Vol.3(4):P. 215 – 232. -URL https://doi.org/10.1002/we.40.

Schreck, S. J., Robinson, M. C., Hand, M. M., & Simms, D. A. (2001). Blade dynamic stall vortex kinematics for a horizontal axis wind turbine in yawed conditions. *Journal of Solar Energy Engineering*, Vol.123(4):P. 272 – 281. -URL https://doi.org/10.1115/1.1408307.

Schreck, S. J., Sørensen, N. N., & Robinson, M. C. (2007). Aerodynamic structures and processes in rotationally augmented flow fields. *Wind Energy: An International Journal for Progress and Applications in Wind Power Conversion Technology*, 10(2):159–178.

Schümann, H., Pierella, F., & Sætran, L. (2013). Experimental investigation of wind turbine wakes in the wind tunnel. *Energy Procedia*, 35:285–296.

Schürmann, H. (2007). *Konstruieren mit Faser-Kunststoff-Verbunden.* Vol.2. Springer-Verlag Berlin Heidelberg. ISBN: 978-3-540-72189-5.

Sears, W. R. (1938). *A Systematic Presentation of the Theory of Thin Airfoils in Non- Uniform Motion.* Dissertation, California Institute of Technology. -URL https://doi.org/10.7907/EM5X-CZ66.

Sedano, C. A., Berger, F., Rahimi, H., Mejia, O. D. L., Kühn, M., & Stoevesand, B. (2019). Cfd validation of a model wind turbine by means of improved and delayed detached eddy simulation in openfoam. *energies*, Vol.12(7):P.1–17. -URL https://doi.org/10.3390/en12071306.

Sicot, C., Devinant, P., Loyer, S., & Hureau, J. (2008). Rotational and turbulence effects on a wind turbine blade. investigation of the stall mechanisms. *Journal of Wind Engineering and Industrial Aerodynamics*, Vol.96:P. 1320 – 1331. -URL https://doi.org/10.1016/j.jweia.2008.01.013.

Spiegelberg, H. (2014). *Adaptive Camber Airfoil for Load Alleviation in Horizontal Axis Wind Turbines: Analytical and Numerical Study.* Dissertation, TU Darmstadt.

Theodorsen, T. (1935). General theory of aerodynamic instability and the mechanism of flutter. *National Advisory Committee for Aeronautics*, Vol.496:P.291–312. -URL https://ntrs.nasa.gov/search.jsp?R=19930090935.

Treaster, A. L. & Yocum, A. M. (1978). The calibration and application of five-hole probes. *24th International Instrumentation Symposium, Albuquerque, New Mexico*, May,1978:P.255–266.

van Garrel, A. (2003). Developement of a wind turbine aerodynamic simulation model. *Technical Report, ECN*. -URL https://doi.org/10.13140/RG.2.1.2773.8000.

Wei, N. J., Kissing, J., & Tropea, C. (2019). Generation of periodic gusts with a pitching and plunging airfoil. *Experiments in Fluids*, Vol.60(11):P.166. -URL https://doi.org/10.1007/s00348-019-2815-1.

Wei, N. J., Kissing, J., Wester, T. T. B., Wegt, S., Schiffmann, K., Jakirlic, S., Peinke, J., & Tropea, C. (2018). Insights into the periodic gust response of airfoils. *Journal of Fluid Mechanics*, Vol.876:P.237–263. -URL https://doi.org/10.1017/jfm.2019.537.

Weitemeyer, S., Reinke, N., Peinke, J., & Hölling, M. (2013). Multi-scale generation of turbulence with fractal grids and an active grid. *Fluid Dynamics Research*, Vol.45(6):P.061407. -URL https://doi.org/10.1088/0169-5983/45/6/061407.

Wendler, J., Marten, D., Pechlivanoglou, G., Nayeri, C., & Paschereit, C. (2016). Implementation and validation of an unsteady aerodynamics model for horizontal and vertical axis wind turbines within the simulation tool qblade. *Proc. of the ASME Turbo Expo 2016*, pages 13–17.

Wester, T., Kampers, G., Gülker, G., Peinke, J., Cordes, U., Tropea, C., & Höllig, M. (2018a). High speed piv measurements of an adaptive camber airfoil under highly gusty inflow conditions. *Journal of Physics: Conference Series*, Vol.1037:P.072007. -URL https://doi.org/10.1088%2F1742-6596%2F1037%2F7%2F072007.

Wester, T. T. B., Bartholomay, S., Traphan, D., Höllig, M., Peinke, J., & Gülker, G. (2018b). Using high speed piv measurements and pod to solve the mystery of dynamic stall. *19th International Symphosium on the Application of Laser and Imaging Techniques to Fluid Mechanics, Lisbon, Portugal*, Jul,2018.

Xu, H., Qiao, C., & Ye, Z. (2016). Dynamic stall control on the wind turbine airfoil via a co-flow jet. *energies*, Vol.9(6):P.429–454. -URL https://doi.org/10.3390/en9060429.